The Astronomical Journal, 145:6 (34pp), 2013 January doi:10.1088/0004-6256/145/1/6

EXTENDING THE NEARBY GALAXY HERITAGE WITH *WISE*: FIRST RESULTS FROM THE *WISE* ENHANCED RESOLUTION GALAXY ATLAS

T. H. Jarrett[1,2], F. Masci[1], C. W. Tsai[1], S. Petty[3], M. E. Cluver[4], Roberto J. Assef[5,14], D. Benford[6], A. Blain[7], C. Bridge[8], E. Donoso[9], P. Eisenhardt[5], B. Koribalski[10], S. Lake[3], James D. Neill[8], M. Seibert[11], K. Sheth[12], S. Stanford[13], and E. Wright[3]

[1] Infrared Processing and Analysis Center, California Institute of Technology, Pasadena, CA 91125, USA
[2] Astronomy Department, University of Cape Town, Rondebosch 7701, South Africa
[3] Physics and Astronomy Department, University of California, Los Angeles, CA 90095, USA
[4] Australian Astronomical Observatory, P.O. Box 915, North Ryde, NSW 1670, Australia
[5] Jet Propulsion Laboratory, California Institute of Technology, 4800 Oak Grove Drive, Mail Stop 169-221, Pasadena, CA 91109, USA
[6] NASA Goddard Space Flight Center, Code 665, Greenbelt, MD 20771, USA
[7] Physics & Astronomy, University of Leicester, University Road, Leicester LE1 7RH, UK
[8] Department of Astronomy, California Institute of Technology, Pasadena, CA 91125, USA
[9] Spitzer Science Center, IPAC, California Institute of Technology, Pasadena, CA 91125, USA
[10] CSIRO Astronomy & Space Science, Australia Telescope National Facility (ATNF), P.O. Box 76, Epping, NSW 1710, Australia
[11] Observatories of the Carnegie Institution for Science, 813 Santa Barbara Street, Pasadena, CA 91101, USA
[12] NRAO, 520 Edgemont Road, Charlottesville, VA 22903-2475, USA
[13] Department of Physics, University of California, One Shields Avenue, Davis, CA 95616, USA
Received 2012 March 26; accepted 2012 September 30; published 2012 November 30

ABSTRACT

The *Wide-field Infrared Survey Explorer* (*WISE*) mapped the entire sky at mid-infrared wavelengths 3.4 μm, 4.6 μm, 12 μm, and 22 μm. The mission was primarily designed to extract point sources, leaving resolved and extended sources, for the most part, unexplored. Accordingly, we have begun a dedicated *WISE* Enhanced Resolution Galaxy Atlas (WERGA) project to fully characterize large, nearby galaxies and produce a legacy image atlas and source catalog. Here we demonstrate the first results of the WERGA project for a sample of 17 galaxies, chosen to be of large angular size, diverse morphology, and covering a range in color, stellar mass, and star formation. It includes many well-studied galaxies, such as M 51, M 81, M 87, M 83, M 101, and IC 342. Photometry and surface brightness decomposition is carried out after special super-resolution processing, achieving spatial resolutions similar to that of *Spitzer* Infrared Array Camera. The enhanced resolution method is summarized in the first paper of this two-part series. In this second work, we present *WISE*, *Spitzer*, and *Galaxy Evolution Explorer* (*GALEX*) photometric and characterization measurements for the sample galaxies, combining the measurements to study the global properties. We derive star formation rates using the polycyclic aromatic hydrocarbon sensitive 12 μm ($W3$) fluxes, warm-dust sensitive 22 μm ($W4$) fluxes, and young massive-star sensitive ultraviolet (UV) fluxes. Stellar masses are estimated using the 3.4 μm ($W1$) and 4.6 μm ($W2$) measurements that trace the dominant stellar mass content. We highlight and showcase the detailed results of M 83, comparing the *WISE*/*Spitzer* results with the Australia Telescope Compact Array H I gas distribution and *GALEX* UV emission, tracing the evolution from gas to stars. In addition to the enhanced images, *WISE*'s all-sky coverage provides a tremendous advantage over *Spitzer* for building a complete nearby galaxy catalog, tracing both stellar mass and star formation histories. We discuss the construction of a complete mid-infrared catalog of galaxies and its complementary role of studying the assembly and evolution of galaxies in the local universe.

Key words: galaxies: fundamental parameters – galaxies: statistics – infrared: galaxies – surveys – techniques: image processing

Online-only material: color figures

1. INTRODUCTION

Galaxies are the basic building blocks of the baryonic universe, self-contained laboratories for studying the complexity and sustainability of converting gas into stars. Comprising the local universe, nearby galaxies represent a *fossil record* of galaxy evolution, the boundary condition for cosmological models that explain past and current states of the universe. Although galaxies come in all shapes, sizes, mass, and morphological cases, the physics governing their structure and evolution should be elemental: we expect that the gravitational collapse of the interstellar medium (ISM, i.e., gas) to form new stars is held in check by angular momentum and the energetic "feedback" from recently formed hot massive stars, supernova explosions, and active nuclei. However, even the basic processes in this evolution are poorly understood, leaving major questions unanswered, including the following. What is the relationship between the density of the ISM and the amount of stars formed? What governs the mass spectrum of stars formed in a single event? How does the internal mass distribution within a galaxy affect its distribution of ISM and star formation? What role does the dominant mass constituent, i.e., the dark matter, play? Probing galactic structure and star formation history requires understanding the distribution of stars and gas among galaxies of all types and luminosities across a complete range of environments.

The modern study of nearby galaxies is characterized by multi-wavelength sensing that probes the diverse physical processes that drive galaxy evolution. Each window of the

[14] NASA Postdoctoral Program Fellow.

electromagnetic spectrum, from the radio to the X-ray, provides a complementary set of tools that, in combination, reveal the internal life cycle of galaxies. The infrared (IR) window, for example, has dual capability: sensitive to stellar light from the evolved population of stars and relatively low-temperature processes from the ISM and star formation regions. It is ideally suited for studying the stellar mass distribution and obscured star formation history in galaxies. The *Spitzer* Infrared Nearby Galaxies Survey (SINGS; Kennicutt et al. 2003) represents the most complete study of nearby galaxies, employing every IR instrument of *Spitzer* to study in detail the properties of 75 nearby "representative" galaxies. With imaging only, a larger sample is found in the SINGS follow-up project, Local Volume Legacy (LVL). In progress, the *Spitzer* Survey of Stellar Structure in Galaxies (S4G; Sheth et al. 2010) expands the sample to several thousand galaxies through the two short (near-IR) wavelength bands of Infrared Array Camera (IRAC; 3.6 and 4.5 μm), focusing on the internal stellar structure of galaxies.

Following closely in succession to the *AKARI* all-sky survey (Murakami et al. 2007), the *Wide-field Infrared Survey Explorer* (*WISE*; Wright et al. 2010) is the latest generation infrared space telescope. As with *AKARI* but unlike *Spitzer*, it was designed and implemented to map the entire sky. It was thus capable of constructing large, diverse, and complete statistical samples. In common with *Spitzer* imaging, it has both near- and mid-IR channels, sensitive to both stellar structure (as with S4G) and interstellar processes (as with SINGS). The *WISE* All Sky Data Release of 2012 March is available through the Infrared Science Archive (IRSA),[15] and includes imaging and source catalog. It should be emphasized that the *WISE* Source Catalog is designed, optimized, and calibrated for point sources. The complexity of detecting and measuring resolved sources was beyond the resources of the *WISE* Science Data Center (WSDC) processing. As a consequence, the *WISE* archive and public-release catalogs have either completely missed nearby galaxies or, even worse, their integrated fluxes are systematically underestimated (because they are measured as point sources) and often chopped into smaller pieces. However, the *WISE* public-release imaging products do capture resolved and complex objects. One of the goals of this current study is to use new image products to characterize and assess the quality of source extraction for resolved galaxies observed by *WISE*.

This present work demonstrates how *WISE* imaging can be utilized to study nearby galaxies by focusing on a sample of large, well-studied galaxies. Notably, we apply a technique to enhance the spatial resolution of *WISE*, known as the Maximum Correlation Method (MCM; Masci & Fowler 2009), extracting information on physical scales comparable to those of *Spitzer* imaging, thereby enabling detailed study of the internal anatomy of galaxies. The *WISE*-designed MCM method is summarized in Jarrett et al. (2012, hereafter referred to as Paper I), and its performance is demonstrated using both simulations and real *WISE* imaging of the spiral galaxy NGC 1566. The interested reader should refer to Paper I for more details on *WISE* imaging and the MCM. One of the goals of this current study is to use new image products to characterize and assess the quality of source extraction for resolved galaxies observed by *WISE*. We apply image resolution enhancement and compare the resulting measurements with those extracted using *Spitzer* imaging.

The modest sample presented in this work represents the pilot study of the more complete *WISE* Enhanced Resolution Galaxy Atlas (WERGA), consisting of several thousand nearby galaxies. The WERGA will comprise a complete mid-IR source catalog and high-resolution image Atlas of the largest (diameter $>1'$) angular-sized galaxies in the local universe. The galaxies that have an optical or near-IR angular diameter greater than $2'$ will undergo special MCM processing in which super-resolution methods are used to create the highest angular (spatial) resolution *WISE* images, comparable to the spatial resolution of *Spitzer*/IRAC and *Spitzer*/MIPS-24, while the remaining sources will be co-added using a "drizzle" method that significantly improves upon the nominal *WISE* co-added imaging.[16] Source characterization and extraction will be carried out with these enhanced images, comprising a source catalog that will be part of a public release through NASA Extragalactic Database (NED).

We have chosen a sample of nearby galaxies all observed by *Spitzer* and *Galaxy Evolution Explorer* (*GALEX*), to focus on the detailed *WISE* performance relative to these missions. We introduce the sample in Section 2 and the observations and data in Section 3. In Section 4 we present the results and performance, starting with a case study of early-type galaxies with their fossilized stellar populations, and then for the entire sample that consists of a diverse galaxy "zoo," comparing and contrasting the photometric results of *WISE* with those of *Spitzer* and *IRAS* (additional details are provided in Appendices A–D). Section 5 presents a detailed source characterization study of star-forming galaxy M 83 (NGC 5236), comparing *WISE* with *Spitzer*, *GALEX*, and radio observations. In Sections 6 and 7 we present the star formation rates (SFRs) and stellar mass estimation, respectively, derived from the global ultraviolet (UV) and IR photometry, demonstrating the capabilities of *WISE* to study these two important components of galaxy evolution. Finally, in Appendix D, we discuss ongoing work in building the WERGA. The legacy value of these high-resolution images will span decades. *WISE* is likely to be the most sensitive mid-IR all-sky survey available for many years to come.

All reported magnitudes are in the Vega System (unless otherwise specified). Conversion to the monochromatic AB system entails an additional 2.699, 3.339, 5.174, and 6.620 mag added to the Vega magnitudes for $W1$, $W2$, $W3$, and $W4$, respectively (Jarrett et al. 2011).

2. THE SAMPLE

The sample selection was driven by the primary science goal of this study: to demonstrate the scientific performance of extended source characterization using *WISE* imaging. The photometric performance is assessed by comparison with *Spitzer* measurements, both from the literature and from this study. We therefore require that the sample have previous, high-quality observations from *Spitzer*/IRAC and MIPS-24 imaging. Moreover, the sample should consist of galaxies of various morphologies, orientations and sizes, including a few large cases (e.g., M 83) to study their internal anatomy.

As such, we have chosen a total of 17 galaxies for this pilot study, presented in Table 1. The bulge-dominated elliptical galaxies in this sample, NGC 584, NGC 777, and NGC 4486 (M 87), can be simply modeled due to their fossilized population, and thus provide a test case of photometric calibration, color, and aperture corrections. The grand design spirals, NGC 628, M 81, M 51, M 83, M 101, NGC 6946, and IC 342,

[15] http://irsa.ipac.caltech.edu/

[16] Public-release *WISE* co-added images are referred to as "Atlas" images, available through http://irsa.ipac.caltech.edu/applications/wise/

Table 1
Observed Sources

Name	Distance (Mpc)	Type	log $M_{\rm H\,I}$ (log $M_\odot$)	Field Size ($'$)	Reference	Comment
NGC 584	19.0	E4	...	10	1	IRAC flux calibrator; SINGS galaxy
NGC 628 (M 74)	8.2	SA(s)c	9.91	23	2,3	SINGS galaxy
NGC 777	54.5	E1 Sy2	...	10	4	IRAC flux calibrator
NGC 1398	20.5	SB(r)ab	9.46	12	5,6	S4G galaxy
NGC 1566	9.5	SAB(s)bc Sy1.5	9.99	15	4,5,6	SINGS galaxy
NGC 2403	3.6	SAB(s)cd	9.32	25	4,5,6	SINGS galaxy
NGC 3031 (M 81)	3.7	SA(s)ab	8.93	43	7,8	Bode's Galaxy; SINGS galaxy
NGC 4486 (M 87)	16.7	E0 pec; Sy	...	30	20	Virgo A
NGC 5194 (M 51a)	8.4	SA(s)bc pec	10.01	20	5,9	Whirlpool Galaxy; SINGS galaxy
NGC 5195 (M 51b)	8.4	SB0 pec	...	20	5	SINGS galaxy
NGC 5236 (M 83)	4.7	SAB(s)c	9.92	17	2,5,9	Southern Pinwheel Galaxy
NGC 5457 (M 101)	7.2	SAB(rs)cd	10.30	33	9,10,11	Pinwheel Galaxy
NGC 5907	16.5	SA(s)c	10.39	30	4, 5,12,13	Edge-on disk
NGC 6118	23.1	SA(s)cd	9.58	10	5,9	S4G galaxy
NGC 6822	0.5	IB(s)m	8.16	30	5,6, 14,15	Barnard's Galaxy; SINGS galaxy
NGC 6946	6.1	SAB(rs)cd	10.10	23	5, 16,17	Fireworks Galaxy; SINGS galaxy
IC 342	3.1	SAB(rs)cd; Sy-2	9.71	27	5,18,19	Nuclear starburst

References. (1) Tonry et al. 2001; (2) Herrmann et al. 2008; (3) Briggs 1982; (4) Willick et al. 1997; (5) Tully 1988; Tully et al. 2009; (6) Kilborn et al. 2005; (7) Kanbur et al. 2003; (8) Chynoweth et al. 2009; (9) Huchtmeier & Bohnensiengel 1981; (10) Paturel et al. 2002; (11) Rogstad & Shostak 1971; (12) Shang et al. 1998; (13) Sancisi & van Albada 1987; (14) Clementini et al. 2003; (15) Cannon et al. 2006; (16) Poznanski et al. 2009; (17) Boomsma et al. 2008; (18) Crosthwaite et al. 2000; (19) Saha et al. 2002; (20) Larsen et al. 2001).

all possess strong ISM and star formation emission detected in the *WISE* long-wavelength channels of 12 and 22 μm. Strong nuclear starburst emitting galaxies are included in the form of NGC 1566, NGC 6946, and IC 342. The interacting system, M 51, consisting of a late-type spiral and early-type elliptical galaxy, represents a challenging case for deblending the photometric components. Edge-on disk galaxy, NGC 5907, clearly reveals the transverse bulge and halo components. In addition, the flocculent disk galaxy, NGC 2403, and ringed-spiral galaxy NGC 1398 are included. Finally, the Magellanic barred galaxy, NGC 6822, represents the nearest galaxy in the sample (part of the Local Group), and one of the most challenging to characterize due to the low surface brightness, amorphous shape, and severe foreground stellar contamination. The basic properties are listed in Table 1, including the distance, morphology, and neutral hydrogen content. Molecular hydrogen masses are tabulated in Leroy et al. (2008) for several galaxies in the sample (M 51a, NGC 628, NGC 2403, NGC 6946). Most of the samples have been observed by SINGS, S4G, or were part of targeted *Spitzer* programs (e.g., M 83, M 101, IC 342). The distances, as compiled in NED, are derived from relatively accurate (~5%) distance-ladder methods, including Tully–Fisher (TF), period–luminosity Cepheid variables, tip of the red giant branch (TRGB), Type II radio supernovae, planetary nebula luminosity function (PNLF), red supergiant variable (RSV) stars, and surface brightness fluctuations. We have eliminated outlier distance measurements and re-computed the average distance in Mpc; the table also specifies the primary reference for the distance measurements. The neutral hydrogen mass (with references given in the table) were re-scaled to the adopted distance listed in the table. Finally, the Hubble-type morphologies are taken from NED and T-Types (e.g., RC3 of de Vaucouleurs et al. 1991; de Vaucouleurs 1994) are assigned using these morphologies.

For the galaxy sample presented in this work, we find that between 10 and 20 reconstruction iterations provide the necessary balance between CPU demands, resolution enhancement, and artifact mitigation (artifact-ringing associated with bright sources). We have constructed HiRes mosaics limiting the total number of iterations to 20 for $W1$, $W2$, and $W3$, and 10 iterations for $W4$ (due to lower quality sampling and signal-to-noise ratio for this channel). The resulting images, with pixel scale $0\farcs6875$, are represented in Figure 1. The angular resolution is comparable to that of *Spitzer* imaging, explained in detail in the following section. The images are shown with four colors, where each color is assigned to a *WISE* band: blue ↔ $W1$ (3.4 μm), cyan ↔ $W2$ (4.6 μm), orange ↔ $W3$ (12 μm), and red ↔ $W4$ (22 μm). Stellar light from the old, evolved population will appear blue/green, and tends to concentrate in the nucleus and bulge regions. The ISM, warmed and excited by star formation, will appear yellow/orange, delineating H II and photodissociation regions (PDRs) as well as warm dust emission (red) from the disk. The early-type galaxies, discussed in Section 4.1, are shown in Figure 2.

3. OBSERVATIONS, CALIBRATION, AND SOURCE CHARACTERIZATION METHOD

3.1. WISE Observations

The NASA-funded Medium-Class Explorer mission, *WISE*, consists of a 40 cm primary-mirror space infrared telescope, whose science instrumentation includes 1024 × 1024 pixel Si:As and HgCdTe arrays, cooled with a two-stage solid hydrogen cryostat. Dichroic beam splitters allow simultaneous images in four mid-IR bands, each covering a $47' \times 47'$ field of view. The duty cycle was 11 s, achieved using a scan mirror that stabilizes the line of sight while the spacecraft scans the sky, achieving an angular resolution of $\sim 6''$ in the short bandpasses and $\sim 12''$ in the longest bandpass. Multiple, overlapping frames are combined to form deeper co-added images. Launched in 2009 December into a Sun-synchronous polar orbit, over a time span of eight months *WISE* completed its primary mission to survey the entire sky in the 3.4, 4.6, 12, and 22 μm IR bands with 5σ point-source sensitivities of at least 0.08, 0.11, 0.8, and 4 mJy, respectively (Wright et al. 2010) and considerably deeper sensitivities at higher ecliptic latitudes (Jarrett et al. 2011).

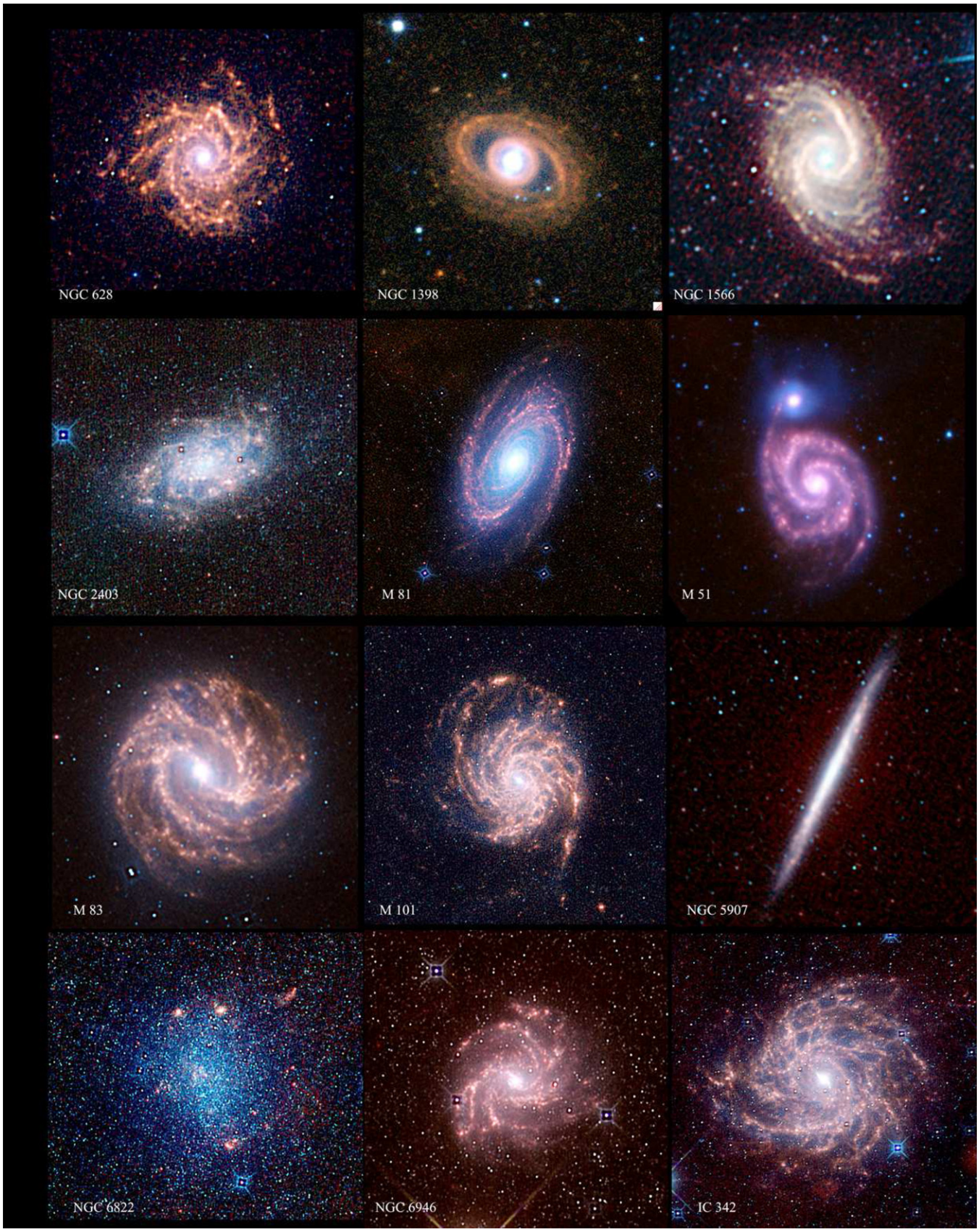

Figure 1. *WISE* montage of nearby galaxies, showing resolution-enhanced images of the sample galaxies (Table 1). The colors correspond to *WISE* bands: 3.4 μm (blue), 4.6 μm (cyan/green), 12.0 μm (orange), and 22 μm (red).

(A color version of this figure is available in the online journal.)

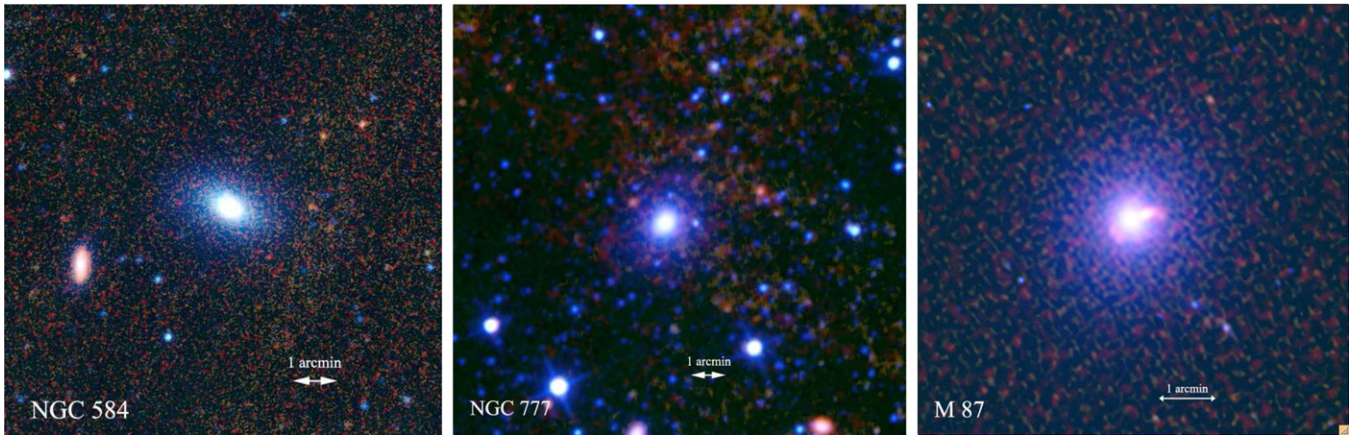

Figure 2. *WISE* view of early-type, elliptical galaxies NGC 584, NGC 777, and M 87. The colors correspond to *WISE* bands: 3.4 μm (blue), 4.6 μm (green), 12.0 μm (orange), and 22 μm (red).

(A color version of this figure is available in the online journal.)

Detailed in the *WISE* Explanatory Supplement (Cutri et al. 2011),[17] "Atlas" Images are created from single-exposure frames that touch a pre-defined $1.^{\circ}56 \times 1.^{\circ}56$ footprint on the sky. For each band, a spatially registered image is produced by interpolating and co-adding multiple 7.7/8.8 s single-exposure images onto the image footprint. To suppress copious cosmic rays and other transient events that populate the single-exposure frames, time-variant pixel outlier rejection is used during the co-addition process. The resulting sky intensity "Atlas" mosaics are 4095 × 4095 pixels with $1.''375$ pixel^{-1} scale, providing a $1.^{\circ}56 \times 1.^{\circ}56$ wide field. In addition to the sky intensity mosaics, 1σ uncertainty maps (tracking the error in intensity values) and depth-of-coverage maps are part of the standard products. The number of frames that are co-added depends on the field location relative to the ecliptic: Those near the equator will have the lowest coverage (typically 12–14 frames), while those near the poles have the highest coverage ($\gg$1000 frames).

For the nominal *WISE* survey, the co-addition process uses a resampling method based on a matched filter derived from the *WISE* point-spread function (PSF). It is designed to optimize detection of point sources, the prime objective of the *WISE* survey. But this interpolation method tends to smear the images, making them less optimal for detection and characterization of resolved sources. Hence, for the WERGA, we have created new mosaics using a resampling kernel that enhances angular resolution, known as Variable-Pixel Linear Reconstruction, or "drizzling," improving the spatial resolution performance compared with nominal *WISE* Atlas Images by ~30%–40%, depending on the depth of coverage. Most importantly, we employ a deconvolution technique known as the MCM (Masci & Fowler 2009), which can improve the resolution by a factor of three to four (see Paper I).

3.2. Spitzer Observations

The bulk of our sample is from the SINGS, LVL, and S4G projects (see Table 1), which have provided enhanced-quality spectroscopy and imaging mosaics.[18] For those galaxies that are not from SINGS or S4G, we have obtained the *Spitzer* data from the *Spitzer* Heritage Archive,[19] curated by IRSA. Here we have used the *Spitzer* pipeline-produced post-basic-calibrated-data (pbcds) IRAC and MIPS mosaics. Analysis for many of these galaxies have been published, including NGC 777 (IRAC Instrument Handbook), NGC 4486 (Shi et al. 2007), M 83 (Dong et al. 2008), M 101 (Gordon et al. 2008), and IC 342 (*Spitzer* Infrared Spectrograph (IRS) spectra from Brandl et al. 2006). For IC 342, we used a combination of both the short and long exposures (also known as high-dynamic range, or HDR observations) because the bright nucleus saturated in the long-exposure IRAC-1 and IRAC-2 imaging. The resultant saturation-corrected images have a larger flux uncertainty due to this "grafting" process.

For IRAC, aperture corrections are required to correct the photometry of extended sources (e.g., galaxies) whose absolute calibration is tied to point sources with the use of finite aperture. These corrections not only account for the "extended" emission from the PSF outer wings (that is outside of the finite calibration aperture), but also from the scattering of the diffuse emission across the IRAC focal plane (see Reach et al. 2005; IRAC Instrument Handbook). For large apertures, the corrections[20] are roughly 8%, 5%, 23%, and 25% for IRAC 1, 2, 3, and 4, respectively. For MIPS-24, the photometric calibration uses an "infinite" aperture calibration, and hence aperture corrections are generally only needed for small apertures (relative to the size of the object being measured; see the MIPS Instrument Handbook). We do, however, apply a small color correction (~4%) for the most spectrally "red" galaxies, as recommended and tabulated in the MIPS Instrument Handbook. Further details of the *Spitzer* photometry and comparison to *WISE* is presented in Appendix A.

3.3. GALEX Observations and Measurements

GALEX FUV (0.1516 μm) and NUV (0.2267 μm) images were obtained from the *GALEX* Medium Imaging Survey (MIS; Martin et al. 2005), which were processed using the standard *GALEX* pipeline (Morrissey et al. 2005, 2007). The MIS reaches a limiting NUV magnitude of 23 (AB mag) through multiple eclipse exposures that are typically 1 ks or greater in duration, while azimuthal averaging reaches surface brightness depths of ~30–31 mag arcsec^{-2} (AB mag).

In order to carry out source characterization measurements, foreground stars were identified and removed from the *GALEX*

[17] http://wise2.ipac.caltech.edu/docs/release/allsky/
[18] http://data.spitzer.caltech.edu/popular/sings/20070410_enhanced_v1/
[19] http://sha.ipac.caltech.edu/applications/Spitzer/SHA/
[20] http://spider.ipac.caltech.edu/staff/jarrett/irac/calibration/ext_apercorr.html

images. Aperture photometry was then carried out on the images using an elliptical annulus to determine the median background and a nested set of elliptical apertures to perform a curve of growth analysis. The reported integrated flux is taken from the aperture that corresponds to the RC3 D25 diameter, whose isophote has a typical UV surface brightness of 30 mag arcsec^{-2}. Further details are presented in Appendix B.

3.4. Optical Imaging

For the M 83 analysis, we compare with optical Hα and *B*-band imaging. The Hα (0.657 μm) imaging was extracted from NED and derived from Meurer et al. (2006), who used the CTIO 1.5 m to obtain Hα(+ continuum) and *R*-band imaging. The continuum-subtracted Hα image has a seeing FWHM of 1.″2. The *B* band (0.44 μm) was acquired with the IMACS instrument aboard the 6.5 m Baade Telescope of the Carnegie Observatory in Las Campanas on 2011 May 29, and was kindly provided by B. Madore (Carnegie). It has a seeing FWHM of 0.″5, representing the highest angular resolution imaging of M 83 that is presented in this work.

3.5. WISE Calibration and Aperture Corrections

The *WISE* photometric calibration, described in detail by Jarrett et al. (2011), relies upon stars that are located at both ecliptic poles and are common to the *Spitzer*, *AKARI*, and *Midcourse Space Experiment* (*MSX*) infrared missions. The stars are well-characterized K-M giants, which have a profile that follows a Rayleigh–Jeans (R-J) distribution, $F_\nu \sim \nu^2$, at mid-IR wavelengths. *WISE* measures the fluxes of stars using optimal profile (PSF) fitting, and the calibration zero-point magnitude is derived from these measurements of the calibration stars. The uncertainty in the zero-point flux-to-magnitude conversion is about 1.5% for all bands. Both the nature of the calibration stars and the method used to measure their flux have important implications toward photometric calibration of extended sources.

There are three different kinds of corrections that are required for aperture photometry measurements using *WISE* co-added mosaics. The first is an aperture correction that accounts for the *WISE* absolute photometric calibration method using PSF profile fitting. Similar to the *Spitzer* aperture correction (Reach et al. 2005), for large aperture measurements of *WISE* images the resulting integrated fluxes must be reduced by a small amount to be consistent with the standard photometric calibration. The All Sky Release Image Atlas requires the following corrections (mag units): 0.034, 0.041, −0.030, and 0.029 mag for $W1$, $W2$, $W3$, and $W4$, respectively, which are to be added to the measured magnitudes. The uncertainty in these aperture corrections is ∼1%.

The second correction is a "color correction" that accounts for the spectral signature of the source convolved with the *WISE* relative system response (RSR). For sources with a constant mid-IR power-law spectrum ($F_\nu \sim \nu^0$), the standard zero magnitude flux density, $F_{\nu 0}$, provides the conversion from *WISE* magnitudes to flux density, namely 309.54, 171.79, 31.64, and 8.63 Jy for $W1$, $W2$, $W3$, and $W4$, respectively. If the source has a spectrum that steeply rises in the mid-IR (e.g., dusty star-forming galaxies), a color correction is required, especially for $W3$ due to its wide bandpass. For example, star-forming galaxies typically have a spectral shape index that is 1 or 2 (e.g., $F_\nu \sim \nu^{-2}$), and thus require a color correction that is roughly −9% in $W3$. In this case, the zero magnitude flux density is 306.68, 170.66, 29.05, and 8.28 Jy, for $W1$, $W2$, $W3$, and $W4$, respectively. The color correction tables and details are given in Wright et al. (2010) and in the *WISE* Explanatory Supplement,[21] Section IV.4.h. We apply this color correction to our *WISE* photometry based on the *WISE* color and the Hubble type of the galaxy; note that for bands $W1$, $W2$, and $W4$, this corrections is always very small, ∼1%; but as noted in the above example, for $W3$ it can be as large as 9%.

The third correction is related to a calibration discrepancy between the *WISE* photometric standard "blue" stars and "red" galaxies (e.g., active galactic nuclei (AGNs) and star-forming galaxies). For the $W4$ measurements, sources with rising spectrum in the mid-IR, $F_\nu \sim \nu^{-2}$, appear brighter than sources that are dominated by R-J emission, corresponding to the standard stars used to calibrate *WISE* photometry. This discrepancy is likely related to an error in the $W4$ RSR, as described in Wright et al. (2010) and Jarrett et al. (2011). Based on work summarized in Jarrett et al. (2011), we have adopted a factor of 0.92 correction to the $W4$ flux of all of our galaxies, except those dominated by the old stellar population (NGC 584, NGC 777, M 87, and NGC 6822) in which case no flux correction is needed. In general, we recommend that this 8% flux correction be applied to all spiral and disk galaxies: translating to *WISE* colors: $(W2 - W3) > 1.3$ mag. Conversely, it should not be applied to those that with bulge-dominated populations: $(W2 - W3) < 1.3$ mag. The photometric uncertainty in $W4$ measurements due to this RSR correction is likely to be at the 3%–5% level.

3.6. Infrared Source Characterization

Basic measurements including position, size, extent, and integrated flux are carried out for all galaxies in the sample, for both *WISE* and *Spitzer* imaging sets. As with the IRAC imaging, the *WISE* MCM-HiRes imaging allows more detailed measurements, including the surface brightness distribution, total flux, effective or half-light radius and surface brightness, concentration metrics, and bulge-to-disk separation. We have adapted tools and algorithms from the Two Micron All Sky Survey (2MASS) Extended Source Catalog (XSC) pipeline (Jarrett et al. 2000) and the *WISE* Photometry System (Cutri et al. 2011), developing an interactive system that is used to identify foreground (contaminant) stars and assist in shape/extent characterization, surface brightness, and integrated flux measurements. It also assists in deblending close galaxy pairs (e.g., M 51, presented below).

The interactive steps are as follows: (1) display images (four bands), including an RGB-color image; (2) identify foreground stars for removal (using colors and proximity to spiral arms); (3) demarcate the central location, size and shape of galaxy (used as a first guess to the two-dimensional fitting routines); and (4) demarcate the location for estimation of the local background. The annulus should be well outside the influence of the galaxy. These initial inputs are supplied to the source characterization processor that carries out the measurements.

For each band, the local background is determined from the pixel value distribution within an elliptical annulus centered on the galaxy. Stars are excluded from the distribution through masking. The histogram mode—most common binned histogram value—is a robust metric for the "sky," and thus is adopted as the local background value. The local background for each band is then removed from the mosaic images. Stars

[21] http://wise2.ipac.caltech.edu/docs/release/allsky/expsup/

are then removed by subtracting them using the *WISE* PSF appropriate for each band. For sources that do not subtract well (due to strong background gradients), the regions are masked and then recovered using local background and isophotal substitution extracted from the galaxy ellipsoid model. With stars removed, the next step is to determine the size and shape of the galaxy. The best-fit axis ratio and ellipticity are determined using the 3σ isophote. The previous steps are then repeated using the updated galaxy shape, and the process is iterated several times until convergence.

The next set of steps it designed to characterize the surface brightness distribution, beginning with the azimuthal-averaged elliptical–radial surface brightness profile, ultimately bounded by the location of the background annulus. The adopted 1σ elliptical isophotal radius then corresponds to the 1σ (sky rms) isophote for each band. *WISE* $W1$ (3.4 μm) is the most sensitive for nearly all types of galaxies and thus has the largest isophotal radius; e.g., it is typically much larger, 3–4×, than in the 2MASS K_s band. Depending on the total coverage (and hence, depth), the typical 1σ isophotal surface brightness is 23.0, 21.8, 18.1, and 15.8 mag arcsec^{-2} (Vega), respectively, for $W1$, $W2$, $W3$, and $W4$ bands. The isophotal fluxes correspond to the integral of the elliptical shape defined by the axis ratio, position angle, and isophotal radius. Additionally, in order to compare across bands to deriving colors, we adopt $W1$ as the fiducial aperture for bands $W1$, $W2$, and $W3$, integrating these other bands using this $W1$ aperture. Since the sensitivity of $W4$ is sufficiently less than that of the other three bands, the $W4$ isophotal radius is considerably smaller than that of $W1$ and is therefore the most appropriate aperture to use for reporting $W4$ integrated fluxes. For all four bands, the axis ratio and position angle shape parameters used in the fiducial aperture photometry are taken from the $W1$ 3σ isophote. The exception, however, to this convention applies to early-type galaxies: since the R-J tail is falling fast in the mid-IR for the old stellar population as traced by the $W3$ and $W4$ bands, the $W1$ fiducial aperture is not appropriate to measurements of elliptical galaxies, and hence we use the $W3$ and $W4$ isophotal fluxes.

The azimuthal elliptical–radial surface brightness is then characterized using a double Sérsic function, where one Sérsic is fit to the inner galaxy region (i.e., the bulge) and the second Sérsic is fit to the outer region (i.e., the disk). Separately integrating these contributions to the total light, a bulge–disk fraction is estimated. This is a very simplistic approach, e.g., it does not account for spiral arms or bars, but serves as a rough estimate for the two general populations. Nearing completion, the fit to the radial surface brightness is used to estimate the total flux by extrapolating the fit to larger radii, corresponding to three times the disk scale length beyond the isophotal radius. This threshold represents a practical balance between capturing the outer disk light and mitigating fit errors that accumulate with radius. The resultant extrapolation or "total" flux can be used to estimate the half-light flux and its corresponding radius. Finally, both half-light and concentration indices follow from integrating the radial surface brightness profile.

4. RESULTS

In this section we present the resolved-source photometric performance derived from *WISE*, first focusing on the relatively simple case of early-type galaxies, comparing the extracted fluxes with the expectation based on the spectral energy distribution (SED) models, followed by the full sample results. A more detailed comparison with *Spitzer* and *IRAS* photometry is presented in Appendix A, notably comparing photometric results across the (approximately equal) paired bands: $W1$ and IRAC-1; $W2$ and IRAC-2; $W3$, IRAC-4, and IRAS-12; and $W4$, MIPS-24, and IRAS-25. Appendix B presents the *GALEX* photometric measurements.

4.1. Photometric Performance: Case Study of Elliptical Galaxies

Early-type "red-sequence" galaxies have conveniently homogeneous properties, resulting in smooth, featureless SEDs that are dominated by the evolved luminous population. Ellipticals and spheroids have low star formation, minimal dust content, and relatively high surface brightness. The bolometric luminosity is dominated by the R-J distribution that spans the near-IR (1–5 μm) window, sampled by the 2MASS J, H, and K_s bands, the IRAC-1 and IRAC-2 bands, and the *WISE* $W1$ and $W2$ bands. For nearby galaxies, the mid-IR light is bright enough to detect the long R-J tail, sampled by the IRAC-3, IRAC-4, MIPS-24, *WISE* $W3$, and *WISE* $W4$ bands. Because of their simple R-J profiles, ellipticals are relatively easy to model. Single burst population synthesis models do an adequate job of describing the mid-IR properties of spheroidal galaxies, and therefore can be used to validate the absolute calibration of the *WISE* and *Spitzer* photometry of resolved sources (see also Petty et al. 2012 for detailed modeling of early-type galaxies using *WISE*, Sloan Digital Sky Survey (SDSS), and *GALEX* measurements).

The sample includes three nearby early-type galaxies, shown in Figure 2: NGC 584, NGC 777, and M 87. The first is a SINGS galaxy with enhanced *Spitzer* observations, including IRS spectra of the nuclear light. The second appears to have nominal properties for galaxies of this type. The third, M 87, is the giant Virgo Cluster elliptical galaxy. It harbors a massive black hole at its center that is powering an AGN, whose signature non-thermal radio lobes and jets (Virgo A) are also visible in the optical and IR. All three have mid-IR light that is dominated by the old stellar population, brightest in the $W1$ band, and thus appearing as "blue" light in the *WISE* color images (Figure 2).

For each galaxy we construct the SED from *GALEX* (see Appendix B), SDSS, 2MASS (Jarrett et al. 2003), and mid-IR measurements from *Spitzer* (Appendix A) and *WISE*; Figure 3. A fiducial aperture, based on the 2MASS K_s-band standard isophote, is applied to each band of *WISE* and *Spitzer*. A small correction is made for the foreground Galactic extinction, estimated from the Schlegel et al. (1998) dust maps and tabulated by NED. Lastly, aperture corrections have been applied to both the *WISE* and *Spitzer* measurements. For comparison, we show the expected light distribution of an old galaxy at $t = 5$ and 13 Gyr, adapted from the GRASIL population synthesis models (Polletta et al. 2006, 2007; Silva et al. 1998). The major difference between the two models is the presence of asymptotic giant branch (AGB) stars in the $t = 5$ Gyr model, bumping up the mid-IR emission beyond 10 μm, demonstrating that evolutionary age is an important consideration when modeling elliptical galaxies. The model SEDs are fit to the data using the K-band (2.2 μm) measurement. Also for comparison we show the SINGS-IRS spectral measurements of the nuclear light, which are consistent with the broadband photometric measurements.

For all three galaxies, the SEDs show similar behavior for the near-IR bands (1–5 μm): the flux density peaks in the H-band (1.6 μm), thereafter steeply falling toward longer wavelengths. The photometric data matches well with the models, and in

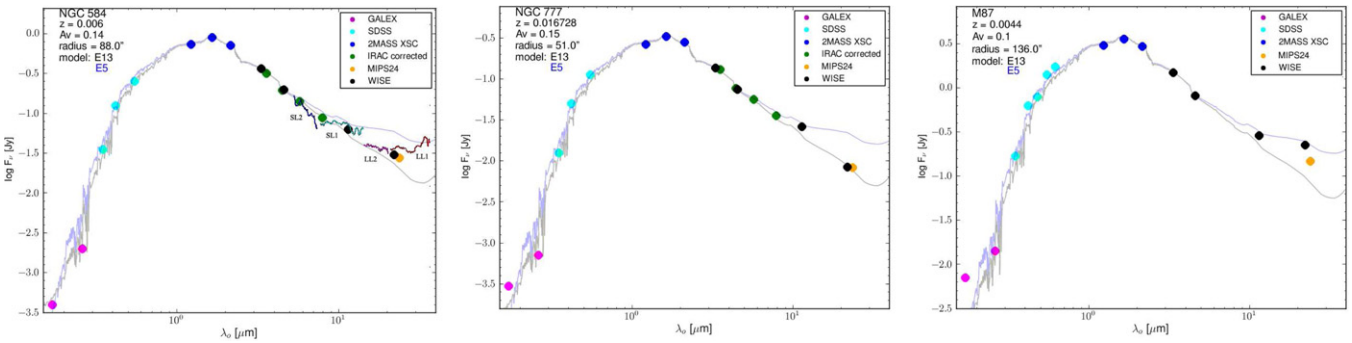

Figure 3. Mid-IR SED for elliptical-type galaxies NGC 584, NGC 777, and M 87. The diagram includes 2MASS XSC, IRAC, MIPS, and *WISE* photometry, where the 2MASS isophotal radius and shape were used as the fiducial aperture. The NGC 584 spectra are from SINGS *Spitzer*/IRS (SL and LL modules) of the nucleus. There is no IRAC data for M 87. The blue and gray lines are old 13 and 5 Gyr galaxy models, respectively, adapted from the GRASIL code (Polletta et al. 2006, 2007; Silva et al. 1998) normalized to the near-IR.

(A color version of this figure is available in the online journal.)

the case of NGC 584, the *Spitzer* spectroscopy of the nuclear emission. In the mid-IR, departures from the R-J tail arise from the presence of warm dust, either from the ISM (star-forming galaxies) or from AGB stars. NGC 584 hints at a warm dust excursion beyond 20 μm, traced by both the IRS-LL1 spectroscopy and the MIPS-24/$W4$ photometry. NGC 777 shows no such excursions and thus appears to be dust free, shining by the light of very old stars. Not surprisingly, Virgo's M 87 exhibits an IR excess due to the stellar light giving way to non-thermal emission from the jet at 22 and 24 μm bands. Both the forward (approaching) and backside (receding) of the central jet are clearly seen in the long-wavelength imaging (Figure 2), notably bright in the $W4$ band compared the MIPS-24 band. Since this emission arises from a powerful, non-thermal source, the models are not relevant to the emission beyond 10 μm, and other than variability between the *WISE* and MIPS-24 observations of M 87, it is unknown why $W4$ is brighter than MIPS-24.

To summarize, all three early-type galaxies in the sample show near-IR photometric properties that are consistent among the data sets: 2MASS versus *WISE* versus *Spitzer*, and among the population synthesis models. Likewise, at longer wavelengths, the galaxies NGC 584 and NGC 777 display photometric results that are consistent between data sets and models. Only M 87 exhibits peculiar properties at the longest wavelengths due to the IR-bright jet that originates from the nucleus and dominates the light beyond 20 μm. We conclude that, for these three galaxies, the *WISE* photometric measurements are consistent with those of *Spitzer*, and that the absolute measurements are consistent with the population synthesis models normalized to the 2MASS photometry.

4.2. WISE Full Sample Measurements

In this subsection we present the photometry and characterization measurements for the entire sample of 17 galaxies, extracted from the *WISE* HiRes imaging. Appendix A presents a comparison between the matched *Spitzer* IRAC and MIPS-24 imaging, as well as between archival *IRAS* 12 and 25 μm measurements. Appendix B presents the *GALEX* measurements.

Similar to the *Spitzer* and MIPS bands, all four *WISE* bands provide valuable spectral information, tracing both stellar light and that arising from the ISM associated with star formation. The *WISE* $W1$ 3.4 μm and $W2$ 4.6 μm bands are nearly ideal tracers of the stellar mass distribution in galaxies because they image the R-J limit of the blackbody emission for stars 2000 K and hotter. These bands are relatively extinction free, and have a $W1 - W2$ color that is constant and independent of the age of the stellar population and its mass function (Pahre et al. 2004; Jarrett et al. 2011). Thus, a combination of the $W1$ and $W2$ luminosities with the corresponding mass-to-light ratio, which varies much less in the mid-IR compared with the optical, leads to the aggregate stellar mass or "backbone" mass assembly of the galaxy (detailed results are presented in Section 6).

At longer wavelengths, the stellar light gives way to the cooler emission of the ISM. The 22 μm band is sensitive to warm dust emission, arising in the vicinity of hot H II regions. Calzetti et al. (2007) using similar 24 μm data from the *Spitzer Space Telescope*, showed that mid-IR fluxes when combined with Hα fluxes provide a powerful reddening free indicator of O/B star formation. Similarly, the 12 μm data are sensitive to polycyclic aromatic hydrocarbon (PAH) emission arising from the photon-dominated regions (PDRs) located at the boundaries of H II regions and molecular clouds and thus excited by far-UV photons. UV photons that manage to escape the dust trap will be traced by *GALEX* imaging, thus completing the census of the current rate of star formation. SFRs derived from the *GALEX*, 12 and 22 μm bands are presented in Section 6.

4.2.1. WISE Source Characterization

Measurements extracted from HiRes imaging is presented in three separate tables: the fiducial isophotal photometry in Table 2, the extrapolated fluxes in Table 3, and the half-light and concentration indices in Table 4. The quoted flux uncertainties include contributions from the Poisson errors and background estimation errors (but do not include the calibration errors). All reported flux densities and their formal uncertainties are in mJy units.

We adopt a fiducial aperture to report integrated fluxes since cross-band comparisons (i.e., colors) may be directly computed from the reported flux measurements. As discussed in Section 3.5, for most galaxies, *WISE* $W1$ (3.4 μm) is the most sensitive band to the faint lower surface brightness emission in the outer disks; consequently, we adopt the $W1$ 1σ isophotal aperture as the fiducial aperture for aperture measurements in the $W1$, $W2$, and $W3$ *WISE* bands, and use the $W4$ isophotal aperture for the $W4$ integrated fluxes. Note that the axis ratio and orientation are based on the higher signal-to-noise ratio isophote at 3σ in $W1$; see Section 3.5. The typical 1σ surface brightness in $W1$ is $\sim$23 mag arcsec^{-2} (Vega).

Table 2
WISE Isophotal-aperture Photometry

Name	R.A. (°)	Decl. (°)	Axis[a] Ratio	P.A.[a] (°)	$R1^{1}_{iso}$ (″)	$R4_{iso}$ (″)	$W1$ (Jy)	$W2$ (Jy)	$W3$ (Jy)	$W4$ (Jy)
NGC 584[b]	22.83626	−6.86801	0.67	66.1	149.2	30.8	0.381 ± 0.004	0.207 ± 0.002	0.051 ± 0.001	0.021 ± 0.001
NGC 628	24.17406	15.78373	1.00	0.0	354.6	198.8	0.885 ± 0.009	0.559 ± 0.006	3.022 ± 0.033	2.864 ± 0.032
NGC 777[b]	30.06247	31.42939	0.83	144.7	176.9	30.8	0.179 ± 0.002	0.102 ± 0.001	0.028 ± 0.000	0.009 ± 0.000
NGC 1398	54.71692	−26.33771	0.71	93.3	326.2	140.0	0.897 ± 0.009	0.518 ± 0.005	0.874 ± 0.010	0.396 ± 0.005
NGC 1566	65.00161	−54.93800	0.68	32.2	374.6	374.6	0.733 ± 0.007	0.451 ± 0.005	1.927 ± 0.021	2.942 ± 0.033
NGC 2403	114.21203	65.59946	0.56	−57.8	627.2	366.5	1.701 ± 0.017	1.099 ± 0.011	4.699 ± 0.052	5.966 ± 0.066
NGC 3031	148.88857	69.06503	0.56	156.4	954.6	495.0	11.317 ± 0.115	6.366 ± 0.064	7.359 ± 0.075	4.966 ± 0.055
NGC 4486[b]	187.70595	12.39088	0.73	158.1	538.5	65.3	2.206 ± 0.022	1.233 ± 0.012	0.321 ± 0.004	0.219 ± 0.003
NGC 5194[c]	202.46976	47.19496	0.67	21.3	402.7	290.3	2.444 ± 0.025	1.564 ± 0.016	11.196 ± 0.113	12.324 ± 0.125
NGC 5195[c]	202.49825	47.26591	0.95	130.4	285.3	72.0	1.153 ± 0.012	0.666 ± 0.007	0.878 ± 0.009	1.255 ± 0.013
NGC 5236	204.25330	−29.86576	1.00	0.0	572.8	338.9	6.272 ± 0.064	3.953 ± 0.040	22.605 ± 0.249	41.175 ± 0.417
NGC 5457	210.80225	54.34859	1.00	0.0	605.2	328.7	2.573 ± 0.026	1.638 ± 0.017	8.384 ± 0.085	8.245 ± 0.084
NGC 5907	228.97302	56.32840	0.17	154.9	413.0	235.6	0.794 ± 0.008	0.499 ± 0.005	1.760 ± 0.018	1.663 ± 0.017
NGC 6118	245.45239	−2.28323	0.42	52.8	177.6	121.5	0.184 ± 0.002	0.113 ± 0.001	0.441 ± 0.005	0.384 ± 0.005
NGC 6822	296.23502	−14.80102	0.87	21.8	562.0	310.0	1.920 ± 0.019	1.122 ± 0.012	1.248 ± 0.021	1.472 ± 0.030
NGC 6946[d]	308.71735	60.15389	1.00	0.0	470.0	310.0	3.177 ± 0.032	2.056 ± 0.021	14.914 ± 0.151	19.187 ± 0.194
IC 342	56.70229	68.09621	1.00	0.0	675.0	527.0	7.671 ± 0.078	4.830 ± 0.049	28.363 ± 0.287	41.821 ± 0.424

Notes.
[a] The fiducial aperture for bands $W1$, $W2$, and $W3$ is based on the $W1$ 1σ isophotal radius. The typical 1σ surface brightness in $W1$ is ∼23 mag arcsec^{-2} (Vega) or 25.7 mag arcsec^{-2} (AB). For $W4$, the isophotal radius of $W4$ is used to define the aperture; the typical 1σ surface brightness in $W4$ is ∼15.8 mag arcsec^{-2} (Vega) or 22.4 mag arcsec^{-2} (AB).
[b] For the early-type elliptical galaxies, the $W3$ aperture radii are based on the $W3$ 1σ isophotal radius due to the lack of strong emission at 12 and 22 μm; they are the following—NGC 584: 52.″9; NGC 777: 64.″0; M 87: 154.″7.
[c] Photometry of NGC 5194/5 is uncertain due to blending.
[d] The MIPS-24 mosaic image is too small to capture the total flux, so a slightly smaller aperture for $W4$ and MIPS-24 is used measure the isophotal flux. Measurements are not corrected for Galactic or internal extinction.

Table 3
WISE Extrapolated Photometry

Name	$R1_{ext}$ (″)	$W1_{ext}$ (Jy)	$R2_{ext}$ (″)	$W2_{ext}$ (Jy)	$R3_{ext}$ (″)	$W3_{ext}$ (Jy)	$R4_{ext}$ (″)	$W4_{ext}$ (Jy)
NGC 584	286.3	0.398 ± 0.004	225.0	0.220 ± 0.002	144.2	0.068 ± 0.002	75.2	0.030 ± 0.001
NGC 628	565.5	0.973 ± 0.012	528.0	0.610 ± 0.007	615.8	3.293 ± 0.044	531.1	3.233 ± 0.046
NGC 777	244.1	0.183 ± 0.002	231.7	0.106 ± 0.001	147.6	0.035 ± 0.001	68.2	0.012 ± 0.000
NGC 1398	554.0	0.902 ± 0.010	462.0	0.528 ± 0.006	562.6	0.966 ± 0.013	280.0	0.661 ± 0.023
NGC 1566	567.2	0.752 ± 0.008	548.5	0.461 ± 0.005	506.7	1.944 ± 0.021	589.8	3.069 ± 0.038
NGC 2403	1555.6	1.776 ± 0.019	1070.6	1.212 ± 0.015	979.2	5.014 ± 0.064	1099.5	8.721 ± 0.239
NGC 3031	1213.9	11.408 ± 0.121	1205.7	6.440 ± 0.069	916.9	8.659 ± 0.138	1331.0	5.599 ± 0.080
NGC 4486	707.0	2.271 ± 0.024	722.2	1.277 ± 0.014	271.2	0.436 ± 0.011	195.8	0.330 ± 0.009
NGC 5194	549.9	2.498 ± 0.027	558.2	1.625 ± 0.018	1070.7	12.245 ± 0.156	497.8	13.086 ± 0.151
NGC 5195	393.0	1.182 ± 0.013	410.8	0.696 ± 0.008	359.9	1.263 ± 0.034	216.0	1.386 ± 0.018
NGC 5236	768.3	6.376 ± 0.066	749.9	4.064 ± 0.042	736.7	23.006 ± 0.249	507.4	43.062 ± 0.494
NGC 5457	870.2	2.703 ± 0.029	900.3	1.792 ± 0.022	891.3	8.839 ± 0.103	684.0	9.768 ± 0.156
NGC 5907	561.0	0.805 ± 0.009	664.6	0.516 ± 0.006	852.8	1.897 ± 0.023	706.9	1.834 ± 0.023
NGC 6118	326.7	0.190 ± 0.002	355.3	0.115 ± 0.001	333.2	0.477 ± 0.006	364.6	0.481 ± 0.010
NGC 6822	1568.8	2.154 ± 0.027	1686.0	1.444 ± 0.028	1686.0	1.645 ± 0.038	805.5	2.174 ± 0.062
NGC 6946	657.3	3.295 ± 0.035	660.6	2.119 ± 0.023	636.1	15.121 ± 0.171	583.6	19.760 ± 0.219
IC 342	1431.0	7.932 ± 0.085	1386.2	4.993 ± 0.054	1432.6	28.977 ± 0.328	1299.6	44.193 ± 0.506

Notes. The extrapolation photometry is the sum of the isophotal aperture photometry (Table 2) and the integral of the double-Sérsic fit to the elliptical–radial surface brightness carried out to a maximum radius of R_{ext}. Measurements are not corrected for Galactic or internal extinction.

We employ a different strategy for elliptical galaxies (and also the nearby irregular galaxy NGC 6822). The light observed in the long-wavelength bands is too faint to obtain a reliable flux in the (relatively) large $W1$ aperture (see Section 4.2); the integrated flux tends to bias high when using a large aperture due to contamination from faint, foreground stars that are not subtracted from the images. Consequently, for NGC 584, NGC 777, M 87 and NGC 6822, the reported $W1$ and $W2$ fluxes are derived from the $W1$ isophote, and the $W3$ flux from the $W3$ isophote, and the $W4$ flux from the $W4$ isophote. The typical 1σ isophotal surface brightness for the $W2$, $W3$, and $W4$ bands, respectively, is 21.8, 18.1, and 15.8 mag arcsec^{-2} (Vega). Details of the isophotal apertures are specified in Table 2 and its notes.

Derived from the integrated fluxes (Table 2), the *WISE* colors and their estimated formal plus calibration uncertainties are presented in Figure 4. Here the magnitudes have been corrected for the estimated foreground Galactic extinction, where we have

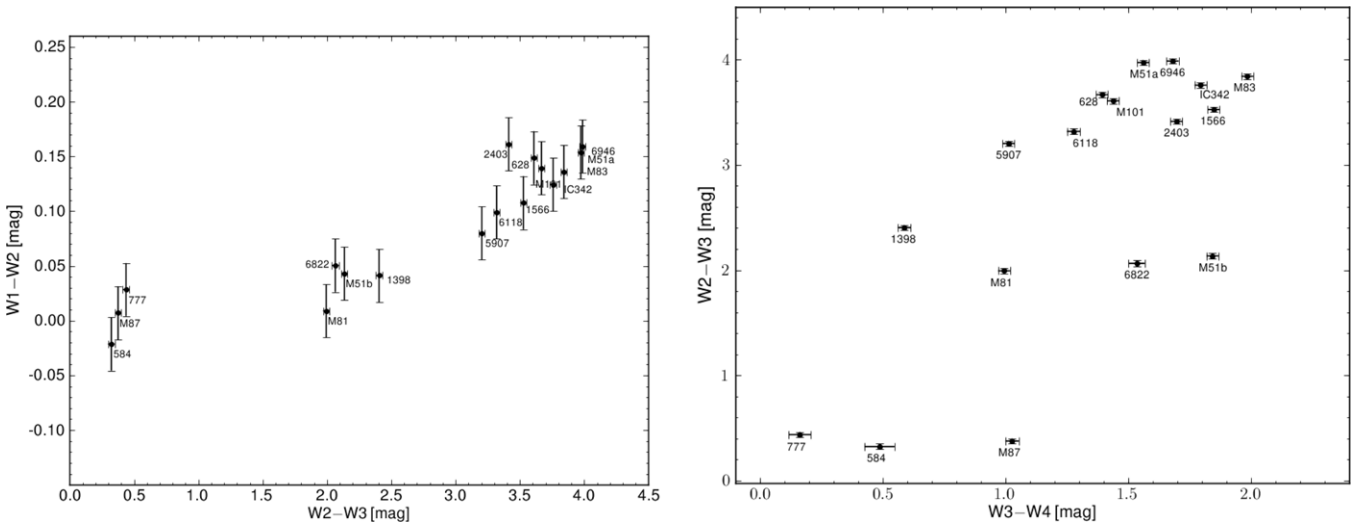

Figure 4. *WISE* colors for the sample, derived from matched aperture photometry. The units are Vega magnitudes. The error bars represent the formal uncertainties (Table 2) and a 1.5% photometric calibration uncertainty. Measurements have been corrected for Galactic and internal extinction. The galaxy name is indicated next to the measurement, where single numbers represent the NGC #.

Table 4
WISE Half-light Surface Brightness, Concentration, and Disk Fraction

Name	$R1_e$ (″)	$W1_e$ (mag arcsec^{-2})	C1	$f1_{\rm disk}$	$R2_e$ (″)	$W2_e$ (mag arcsec^{-2})	C2	$f2_{\rm disk}$	$R3_e$ (″)	$W3_e$ (mag arcsec^{-2})	C3	$f3_{\rm disk}$	$R4_e$ (″)	$W4_e$ (mag arcsec^{-2})	C4	$f4_{\rm disk}$
NGC 584	25.2	15.796	5.46	0.595	27.0	15.947	5.40	0.579	24.0	15.132	4.44	0.594	20.3	14.200	2.90	0.226
NGC 628	114.7	18.550	3.41	0.692	117.5	18.470	3.28	0.761	124.7	14.934	2.48	0.661	114.1	13.300	2.15	0.993
NGC 777	24.3	16.791	5.64	0.658	27.9	17.043	6.06	0.679	26.8	16.317	4.35	0.731	21.3	15.555	2.45	0.053
NGC 1398	55.2	16.679	6.30	0.758	63.4	16.922	6.09	0.815	140.1	16.153	2.95	0.990	124.8	14.854	2.59	0.998
NGC 1566	66.5	17.227	4.11	0.383	65.0	17.068	4.05	0.258	76.0	13.919	2.66	0.997	78.4	12.123	2.71	0.420
NGC 2403	176.9	18.198	3.27	0.343	194.1	18.175	3.64	0.384	181.3	14.650	2.83	0.226	217.7	12.986	3.26	0.457
NGC 3031	168.7	16.082	4.88	0.869	179.5	16.197	4.88	0.778	324.3	15.325	2.54	0.962	305.1	14.207	2.45	0.969
NGC 4486	87.5	16.694	6.41	0.563	94.1	16.838	6.77	0.596	79.4	15.799	5.97	0.824	35.8	12.928	5.21	0.709
NGC 5194	117.6	17.145	3.27	0.928	123.2	17.073	3.22	0.930	139.0	13.308	2.66	0.074	128.5	11.607	2.94	0.851
NGC 5195	43.6	16.184	7.54	0.702	44.6	16.166	8.05	0.561	39.1	13.397	0.00	0.660	0.0	0.090	0.00	0.889
NGC 5236	146.5	17.040	3.30	0.960	145.4	16.873	3.25	0.940	130.4	12.826	2.73	0.928	98.1	10.162	12.28	0.861
NGC 5457	201.7	18.667	2.87	0.984	218.2	18.645	3.02	0.937	207.2	14.963	2.37	0.998	220.3	13.529	2.05	0.999
NGC 5907	79.8	16.045	3.13	0.540	82.6	15.962	3.25	0.441	93.4	12.982	3.06	0.276	81.5	11.261	2.67	0.227
NGC 6118	65.1	18.152	2.44	0.981	65.5	18.075	2.39	0.980	72.6	14.916	2.19	0.990	75.8	13.541	2.29	0.331
NGC 6822	298.8	19.615	2.50	0.321	335.8	19.663	2.69	0.481	316.4	17.464	2.36	0.192	302.6	15.713	1.12	0.951
NGC 6946	142.1	17.692	3.01	0.981	139.4	17.490	3.00	0.980	131.7	13.396	2.84	0.966	110.4	11.262	6.77	0.949
IC 342	279.5	18.206	2.76	0.959	277.4	18.053	2.78	0.974	270.0	14.249	2.66	0.954	179.6	11.446	35.99	0.946

Notes. The half-light is relative to the extrapolated integrated flux; see Table 3. The concentration index is ratio of the 3/4 light-radius to the 1/4 light-radius. The disk fraction, $f_{\rm disk}$, is the fraction of the total integrated light that is attributed to the disk component characterized by the Sérsic function fit to the extended light. Measurements are not corrected for Galactic or internal extinction.

adopted the following coefficients based on merging the Cardelli et al. (1989), Flaherty et al. (2007), and Indebetouw et al. (2005) relations for the near- and mid-IR windows: $A_K = 0.114\ A_V$; $A_{3.4\,\mu{\rm m}} = 0.056\ A_V$; $A_{4.6\,\mu{\rm m}} = 0.049\ A_V$; $A_{12\,\mu{\rm m}} = 0.049\ A_V$; $A_{22\,\mu{\rm m}} = 0$. For the inclined galaxies (M 81, NGC 1566, NGC 2403, NGC 6118, NGC 5907), the expected internal extinction is estimated using the prescription from Masters et al. (2003): $A_K \simeq 0.26\ \log(a/b)$, where a/b is the inverse of the axis ratio.

The color $W1 - W2$ is a metric for the steepness of the falling R-J tail and is also sensitive to nuclear activity (Stern et al. 2012), for the sample is relatively narrow in range, ~0.2 mag, between the elliptical galaxies and the star-forming galaxies—for the most part sampling the same evolved stellar population. In contrast, the color $W2 - W3$ ranges across ~4 mag, from the relatively blue, R-J dominated, elliptical galaxies, to the red, molecular PAH-dominated star-forming galaxies. A linear normal-galaxy "sequence" is formed from early to late-type galaxies. Similarly, the $W3 - W4$ color traces the ISM emission from star-forming galaxies; $W3$ is dominated by the PAH emission and $W4$ is dominated by the warm dust emission arising from the UV radiation field. There are three galaxies that stand out in the $W3 - W4$ color diagram: M 51b, M 87, and NGC 6822. The mid-IR light of M 87 is dominated by the evolved stellar population, but in the 22 μm band the central jet begins to dominate the emission, pushing the color to (relatively) redder levels. The early-type galaxy M 51b has blended ISM dust/PAH emission from its larger, late-type companion, M 51a, as well as possessing a nuclear molecular structure (cf. Kohno et al. 2002), thereby exhibiting hybrid IR colors that reflect stellar and ISM emission. NGC 6822 is the only dwarf galaxy in the sample, possessing an old stellar

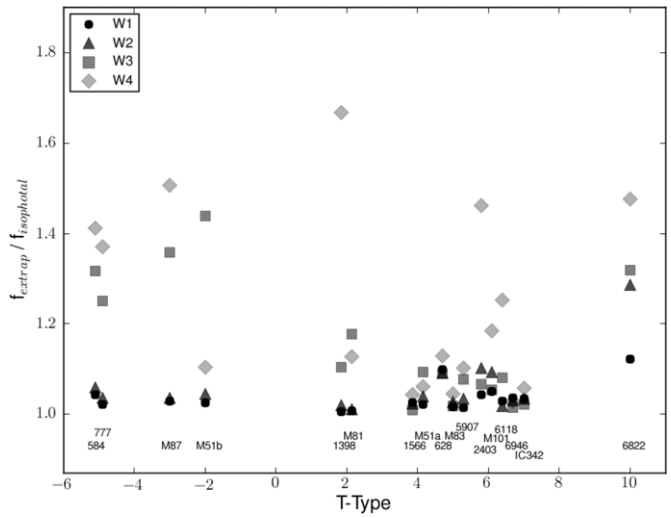

Figure 5. Ratio of the extrapolation ("total") flux to the isophotal (1σ) flux. The galaxy name is indicated below the measurement, where single numbers represent the NGC #. The Hubble T-Type is derived from the morphology (Table 1).

population that dominates the short-wavelength bands (∼similar in color to early-type spirals) and isolated star formation regions that give it a $W3-W4$ color that is comparable to late-type spirals.

To estimate the total flux, the double-Sérsic fit to the radial surface brightness (see Appendix C) is used to extrapolate the integrated flux to lower levels, corresponding to a radius that is 3 disk scale lengths extended beyond the 1σ isophotal radius. The resulting photometry is presented in Table 3. In $W1$, the flux densities range from 0.2 Jy (NGC 777) to 12 Jy (M 81). The brightest flux, ∼45 Jy, is recorded for IC 342 in the $W4$ band, and the largest sizes, $\sim1^{\circ}$, are derived for NGC 2403 and M 81. The extrapolation adds only a small correction to the isophotal fluxes in the $W1$ and $W2$ bands, typically only a few percent (see Figure 5). This result suggests that the $W1$ and $W2$ isophotal radii basically capture the total flux of the systems, attributed to the sensitivity and depth of these bands in *WISE*. In contrast, the $W3$ and $W4$ bands require large corrections: $W3$ ranges from a nearly few percent to 30%, and $W4$ up to 70% corrections, notably for the early-type galaxies, NGC 2403, the ringed-spiral NGC 1398, and the low surface brightness "flat" NGC 6822.

Derived using the extrapolation fluxes as a proxy for the total flux, the half-light, concentration, and disk fraction indices are presented in Table 4. As expected, the highest $W1$ and $W2$ surface brightnesses (likewise, concentration indices) are observed for the early-type galaxies, dominated by the bulge light that is tracing the large stellar masses (see Figure 6). The contrast seen between the central light and the total light is much less, so in the long-wavelength bands, $W3$ and $W4$, the mid-IR emission largely originates from the disk ISM. $W3$ exhibits somewhat higher concentration and B/D ratios for the early-type galaxies (due to the R-J component), while for $W4$, with a few exceptions (e.g., M 87 due to the central AGN), the concentration index is basically the same for all Hubble types, presumably because $W4$ is insensitive to the R-J emission from stars. As viewed in these ISM-sensitive bands, the mid-IR light is more evenly distributed throughout the systems.

4.2.2. Comparing WISE with Spitzer and IRAS

Building on the analysis that was carried for NGC 1566 in Paper I, Appendix A presents a detailed comparison between *WISE* and ancillary matched photometry for the entire sample presented in this work. It is augmented with SED analysis using population synthesis models and the bandpass information, with results that validate the *WISE* photometric calibration and WERGA imaging at 5%–10% relative to *Spitzer* and *IRAS*.

5. CASE STUDY OF M 83

In this section we showcase the science potential of the *WISE* and *Spitzer* imaging for studying the galaxy NGC 5236 (M 83), comparing the stellar, gas, and dust distribution that the IR observations provide, to complementary tracers of star formation and gas distribution, including UV, Hα, molecular CO, and neutral H I millimeter/radio observations.

5.1. M 83: The Infrared and UV Properties

M 83 is one of the most spectacular nearby galaxies, possessing a face-on, grand-design spiral arm system that is anchored by a large-scale bar. Its beautiful symmetry and prominent spiral arms has earned the moniker, the *Southern Pinwheel Galaxy*. It is also notable for its extended H I disk, spanning more than a degree along its major axis (Tilanus & Allen 1993; Koribalski et al. 2004; Koribalski 2010), and its central nuclear region that is almost exclusively molecular gas (Crosthwaite et al. 2002; Lundgren et al. 2008). In global terms, the molecular gas contributes about 25% to the total gas content.

The mid-IR disk spans about $18'$ down to the 1σ background level in $W1$. Figure 7 compares the *WISE* HiRes imaging and the IRAC+MIPS-24 imaging for the central $14'$ disk. As with the NGC 1566 comparison between IRAC and *WISE* HiRes (Paper I), the M 83 comparison impressively shows how well the *WISE* HiRes reconstructions improve the spatial resolution, nearly matching the $\sim2''$-resolved imaging of IRAC. For both color representations, the faint blue light is tracing the evolved stellar population, smoothly distributed across arms and inner arms, while the orange/red light is arising from star formation, localized to the spiral arms, bar and nuclear regions, as traced by the molecular (PAH) and warm dust emission. The *WISE* and *Spitzer* angular resolution and optimal sensitivity to the gas/ISM reveals substructure between the spiral arms, likely related to the shear-formed "spurs" that arise from differential compression of gas as it flows through the arms (Shetty & Ostriker 2006). Other grand design spirals in the sample also show transverse spurs, including M 101, M 51a, NGC 6946, and most notably, IC 342, who's disk/spiral pattern may be described as a lacework of nodes (massive star formation sites) and filaments (spiral and transverse arms; see Figure 1). Finally, the bar itself appears bounded, to the northeast and to the southwest, by the highest concentration of star formation in the disk—these are the bar transition zones, or bar "cusps." These zones arise from the convergence of gas stream lines due to the interaction of the gravitational density wave with the bar (see Kenney & Lord 1991). Orbit crowding compresses the gas and star formation ensues in these relatively small regions of the disk. Later we investigate the southwest cusp with our multi-wavelength data set that probes down to ∼100 pc scales.

The IR observations of *WISE* and *Spitzer* provide a direct probe of the physical conditions of the ISM responding to the present-day star formation. Confined primarily to the spiral arms, the stars form in giant molecular clouds and complexes

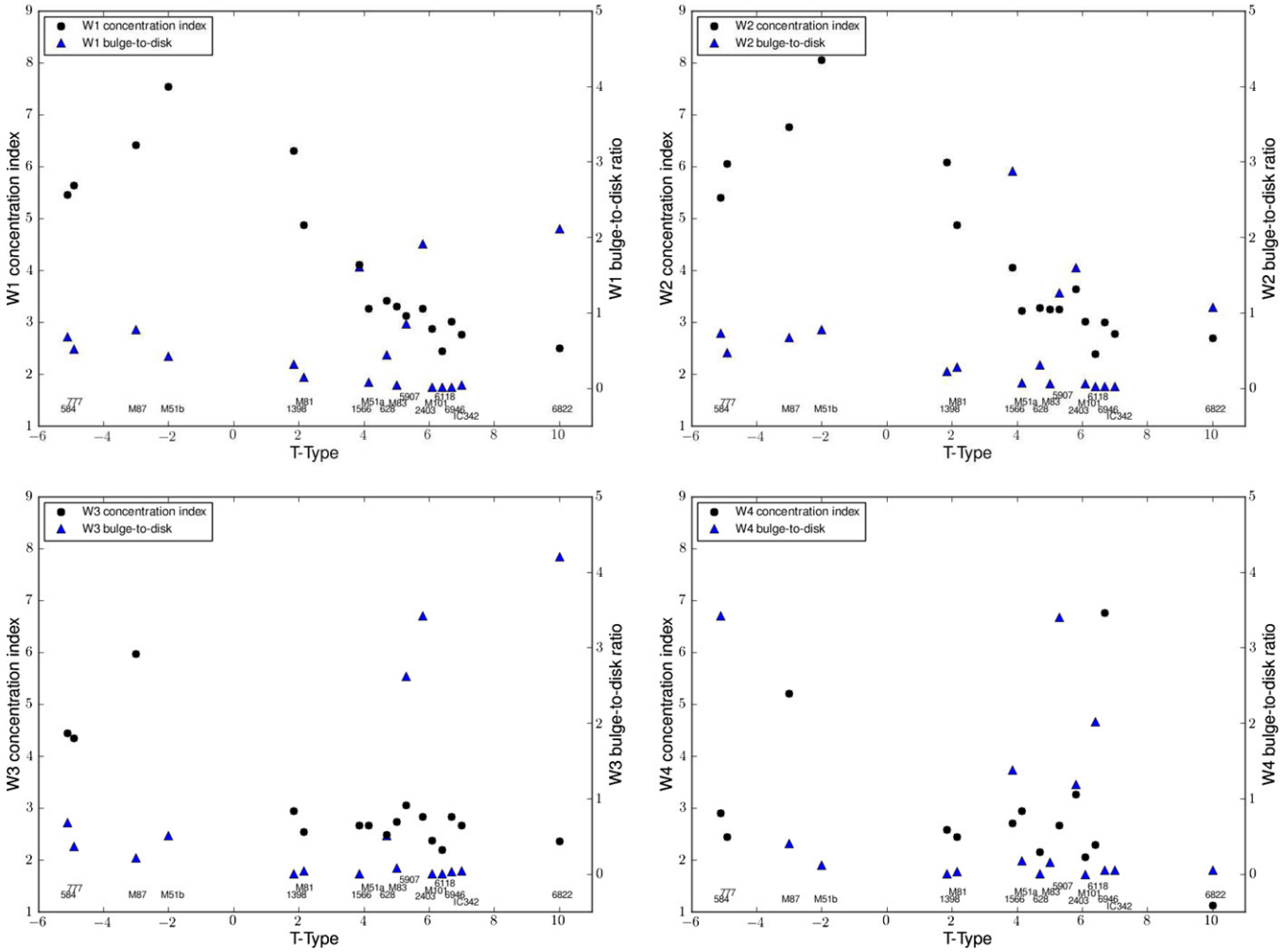

Figure 6. Central concentration index for the galaxy sample, corresponding to the ratio of the 3/4 light-radius to the 1/4 light-radius. For comparison, also shown is the bulge-to-disk ratio based on the double-Sérsic fit to the azimuthally averaged elliptical–radial profile (see Appendix C). The galaxy name is indicated below the measurement, where single numbers represent the NGC #. The Hubble T-Type is derived from the morphology (Table 1).

(A color version of this figure is available in the online journal.)

that are dotted along the arms and in the bar. Figure 8 shows that with radial averaging, the *WISE* colors reveal the axisymmetric arms and complexes (e.g., bar end cusps at a radius of 110″), notably with the $W2 - W3$ color (dashed line), whereas the evolved stellar population is smoothly distributed throughout the disk and bulge (solid line). In a global integrated-light view (right panel of Figure 8), the SED is characterized by a significant (aggregate massive) population of old stars, forming the near-IR peak and R-J tail in the mid-IR, very strong PAH emission at 6.2, 7.7, and 11.2 μm, and a rising warm (dust-emitted) continuum that is powered by young, hot stars, as evident from the relatively bright UV flux observed throughout the disk of M 83.

For disk/spiral galaxies, the stars that provide the most feedback to the ISM are the hottest and most massive. The O and B stars emit strong UV radiation that ionizes and heats the ISM, providing the energy needed to warm dust, excite and break apart molecules thereby creating H II and photodissociation regions (e.g., Tielens & Hollenbach 1985; Wolfire et al. 2003). This young population of stars is ideally probed by the *GALEX* UV survey (Martin et al. 2005) using the 0.1516 μm (FUV) and 0.2267 μm (NUV) bands, obtaining a spatial resolution comparable to that of *WISE*. The integrated flux of M 83 in these two bands is 9.56 (AB mag) and 10.12 (AB mag), respectively, for NUV and FUV, where the magnitudes have been corrected for the foreground extinction toward M 83 ($A_V = 0.22$ mag); see Gil de Paz et al. (2007) for the extinction coefficients. Figure 8 presents the full integrated SED of M 83, plotting the UV, near-IR, and mid-IR photometric results. The figure includes a model that is generic to Sd-type galaxies (generated using the GRASIL code of Silva et al. 1998), simply illustrating that M 83 possesses integrated characteristics of late-type galaxies.

Combining the *GALEX* UV and *WISE* IR observations provides a more complete understanding of the star formation that drives the evolution of disk galaxies. In Figure 9, we present a qualitative perspective of how *GALEX* and *WISE* observations of M 83 form a snapshot gallery of the galaxy anatomy. The color scheme is such that the ISM emission appears orange/red, the evolved stellar "backbone" appears green, and the photospheric light from young, hot stars appears magenta (FUV) and blue (NUV). The largest star formation complexes have both UV and IR light strongly correlated, appearing as white blobs, notably viewed near the bar ends and the connecting eastern spiral arm. The UV–IR color composite also reveals striking differences between the distribution of young stars and the warm ISM: (1) The *GALEX* emission is clearly extended beyond the

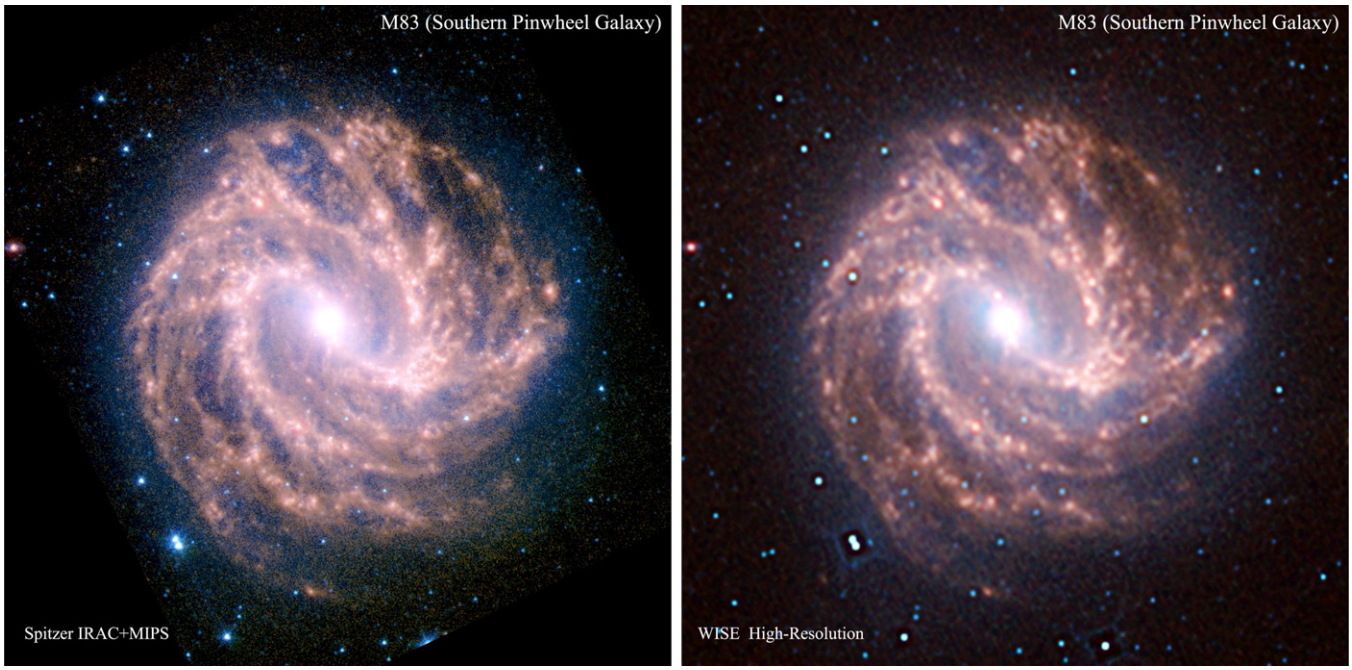

Figure 7. *Spitzer* and *WISE* view of M 83 (NGC 5236). The left panel shows IRAC+MIPS mosaic, where the colors correspond to 3.6 μm (blue), 4.5 μm (green), 5.8 μm (yellow), 8.0 μm (orange), and 24 μm (red). The right panel shows the *WISE* HiRes (MCM) mosaic, where the colors correspond to *WISE* bands 3.4 μm (blue), 4.6 μm (green), 12.0 μm (orange), and 22 μm (red). The field of view for both images is 13.′5.

(A color version of this figure is available in the online journal.)

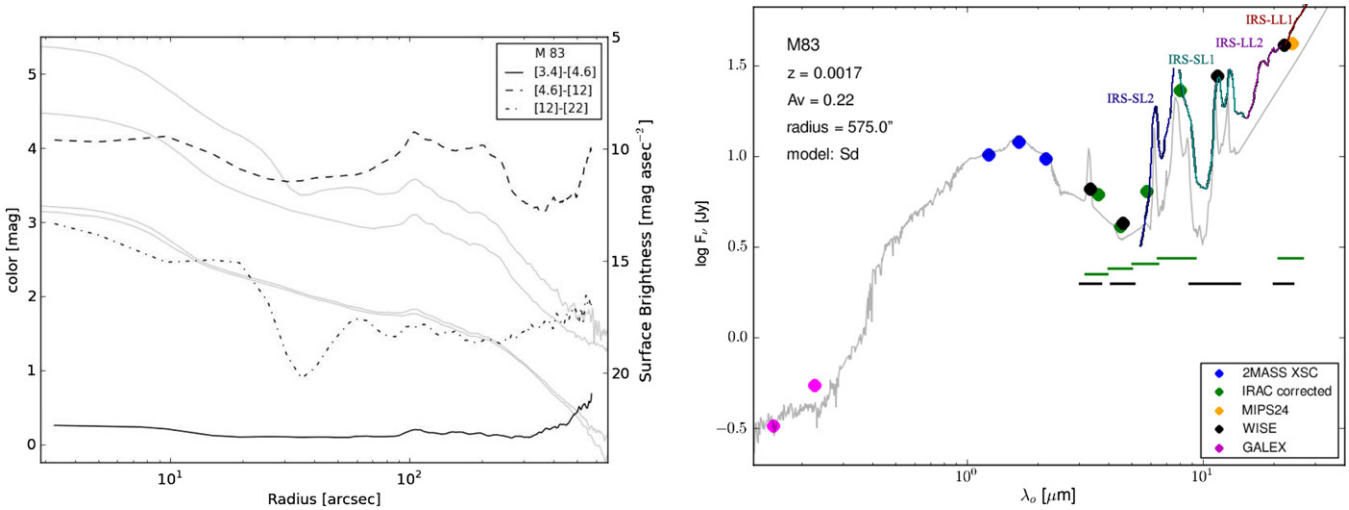

Figure 8. Radial color distribution and global SED for M 83 (NGC 5236). Left: the faint gray lines correspond to the azimuthal elliptical–radial surface brightness. The solid, dashed, and dash-dotted lines correspond to the difference in surface brightness between $W1$ vs. $W2$, $W2$ vs. $W3$, and $W3$ vs. $W4$, respectively. Right: the UV–NIR–MIR SED for M 83, including *GALEX*, 2MASS XSC, IRAC, MIPS, and *WISE* photometry, corrected for the foreground Galactic extinction (A_v = 0.22 mag). The spectra are from SINGS *Spitzer*/IRS (SL and LL modules) of the nucleus. The gray line is an Sd galaxy model, adapted from the GRASIL code (Polletta et al. 2006, 2007; Silva et al. 1998) normalized to the near-IR. The IRAC, MIPS-24 and *WISE* bandpass widths are indicated with solid green and black lines, respectively.

(A color version of this figure is available in the online journal.)

mid-IR limits, highlighting localized star formation that is well outside of the primary (optical R_{25}) disk and spiral arm system, a property that is also seen in many other spiral galaxies studied with *GALEX* (e.g., Thilker et al. 2005; Goddard et al. 2010). (2) The nuclear region and much of the central bar have very little UV emission, while the mid-IR continuum is bright in all *WISE* bands. (3) There is diffuse UV emission filling most of the disk, likely arising from B stars that have dispersed from their birth clouds. (4) The trailing edge of the spirals arms have strong $W3$ IR emission (note the orange/brown color inside of the spiral arms), arising from excited 11.3 μm PAH emission integrated along the galaxy's line of sight. (5) To the north of the nucleus, near the edge of the mid-IR disk, there is a large mid-IR "void" or fork in the spiral arms; in contrast, the entire area is filled with UV emission arising from massive star clusters.

The distinct separation of the UV from the IR emission is further illuminated in Figure 10, comparing the *WISE* $W3$ 12 μm image and the *GALEX* NUV 0.23 μm image of M 83. The primary bar+spiral arms are clearly seen in the 12 μm image, wrapping around the nucleus and extending to the north where

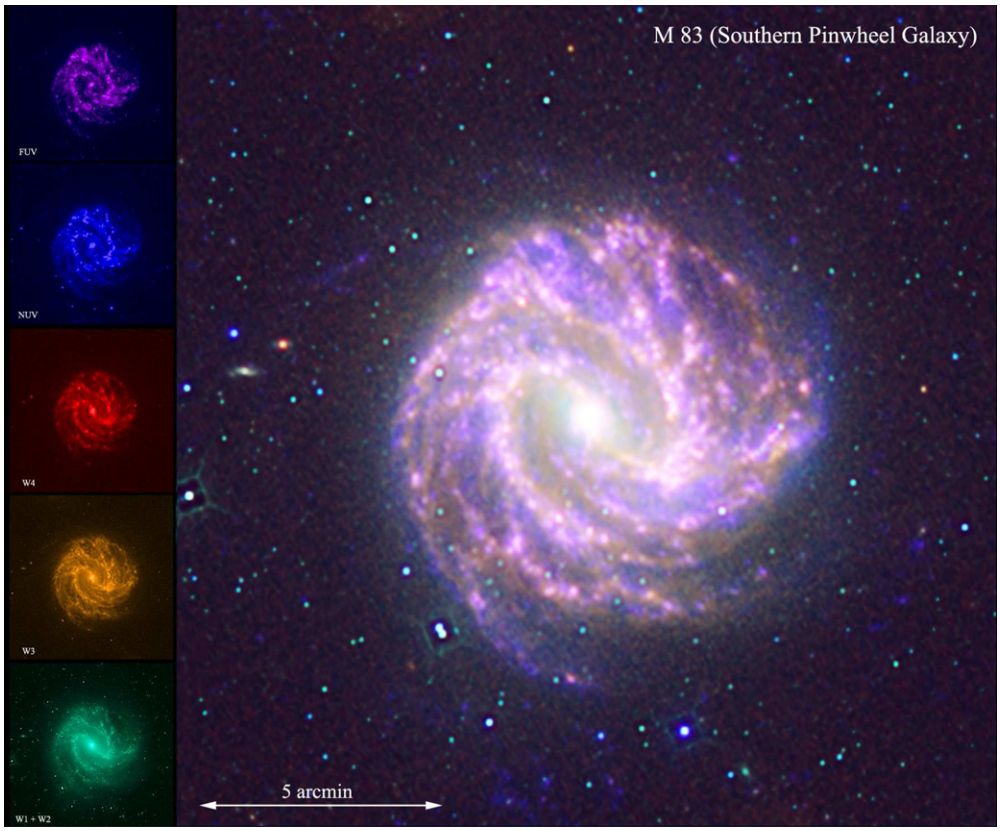

Figure 9. *GALEX* and *WISE* color-composite view of M 83 (NGC 5236). The color assignment for the *WISE* high-resolution imaging (3.4 μm + 4.6 μm, 12.0 μm and 22 μm) and *GALEX* imaging (0.227 μm and 0.152 μm) is shown with the small panels to the left.

(A color version of this figure is available in the online journal.)

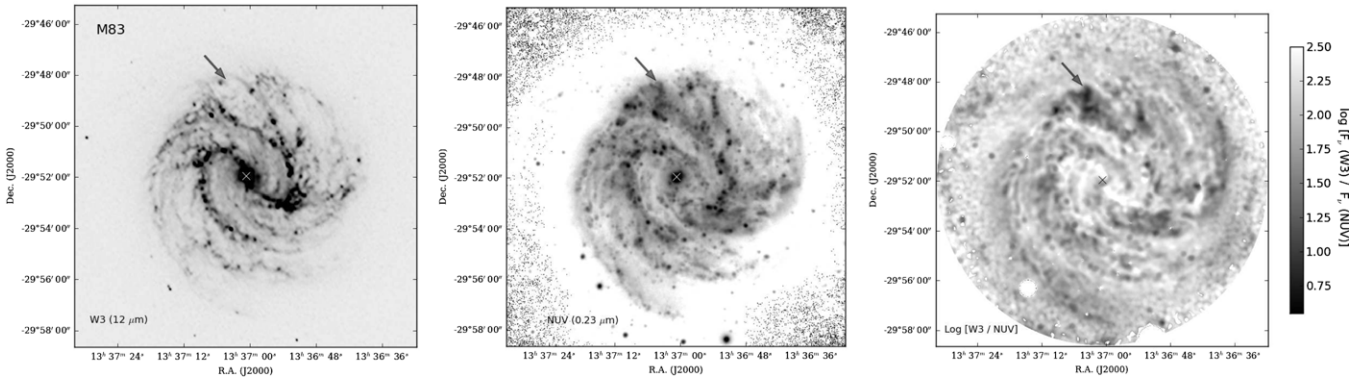

Figure 10. *WISE* $W3$ comparison with *GALEX* NUV of M 83 (NGC 5236). The left panel shows a log-stretch of the *WISE* $W3$ image, the middle panel shows a log-stretch of the *GALEX* NUV image, and the right panel is the flux ratio between the two bands. Dark gray-scale values indicate strong NUV, while light values indicate relatively strong $W3$; e.g., the arrow points to high NUV and low $W3$. The nucleus is denoted with a $\times$ symbol.

it forks into two separate arms. Between these two arms there is hardly any mid-IR emission. Comparing to the NUV image, the bar+spiral arms are not prominent (the southwestern end of the bar has the brightest emission seen in the NUV), but the inter-arm "void" to the north is easily apparent at these wavelengths. The contrast between the $W3$ and the NUV is demonstrated in the flux ratio, $F_\nu(\mathrm{NUV})/F_\nu(W3)$, shown in the third panel of Figure 10: The gray scale is such that strong UV (relative to $W3$) appears gray or black, and inversely, strong $W3$ appears white. The "white" structures show where the UV radiation has been fully absorbed by the dust and re-emitted at longer IR wavelengths. The "gray" complexes have less dust extinction and some large fraction of the UV light escapes. The "black" traces where the UV light is fully escaping from the veil of dust, due to either the absence of gas/dust (perhaps blown out by supernova winds) or the dust geometry; e.g., super star cluster located foreground to the molecular cloud, or located outside of a spiral arm, photoionizing gas and destroying the mid-IR PAHs in the local vicinity.

The northern inter-arm fork/void region is enormous, over $2'$ (>3 kpc) in length. It has two clumps of prominent UV emission (i.e., likely OB associations) and relatively strong diffuse emission filling the void. How does such a large area come to be evacuated of dust and gas (see below) while also filled by light from young, hot stars? The size of such a region seems to preclude a simple wind-blown event coming from a super star cluster; for example, the prominent (and resolved by *Hubble Space Telescope*) stellar cluster, NGC 206, seen in

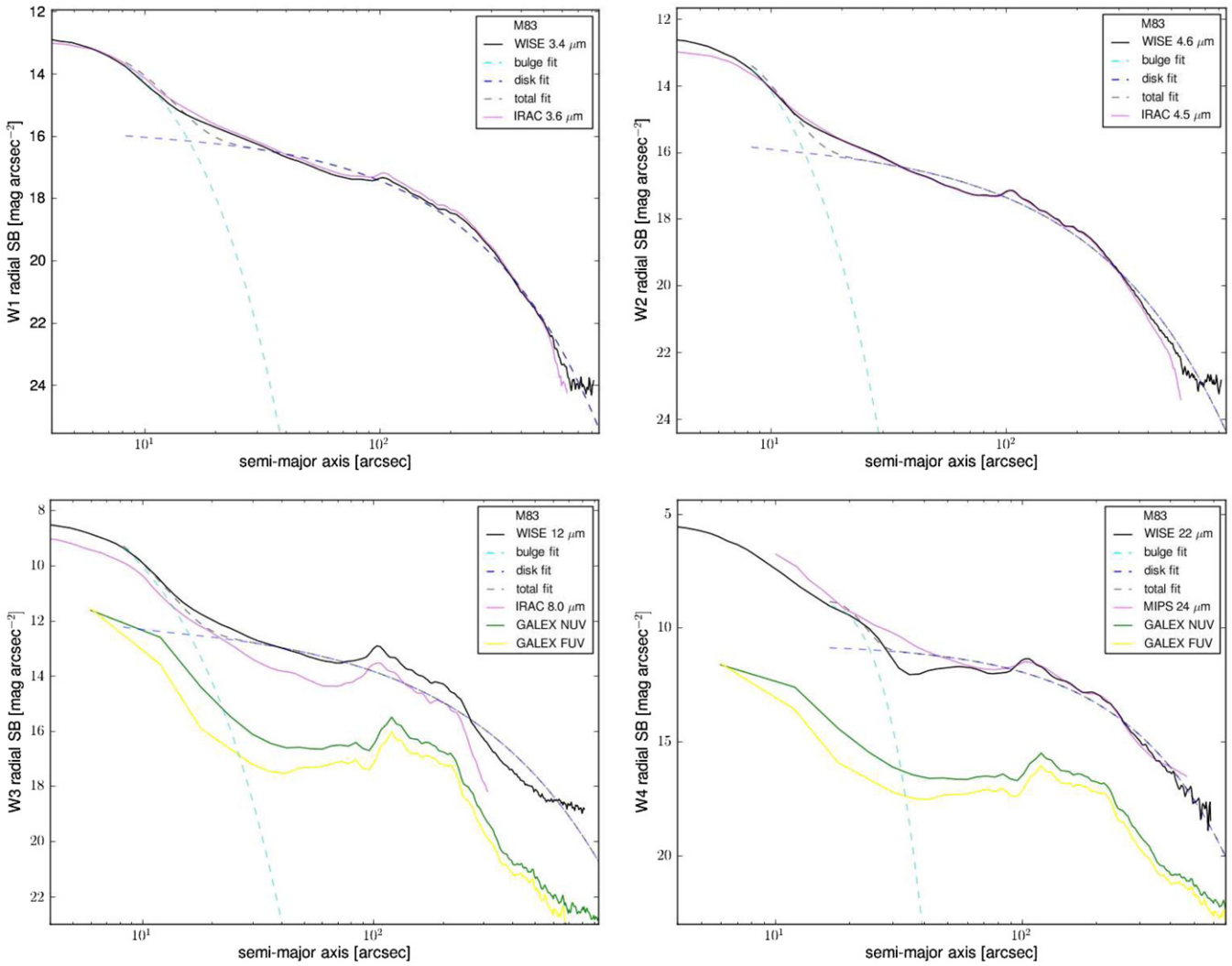

Figure 11. M 83 (NGC 5236) azimuthal elliptical–radial surface brightness profiles (Vega mag arcsec^{-2}), comparing *WISE* (black line) with IRAC and MIPS-24 (magenta line). A double Sérsic function (gray dashed line) is fit to the *WISE* radial profile, where the blue dashed line is the "bulge" component and the magenta dashed line is the "disk" component. Additionally, the *GALEX* NUV and FUV radial profiles are shown in the $W3$ and $W4$ panels (note that the *GALEX* AB magnitudes have been offset by ∼7 mag to fit within the y-axis dynamic range).

(A color version of this figure is available in the online journal.)

the disk of M 31 has cleared out a much smaller physical area (∼500 pc diameter hole; see Hunter et al. 1996) by contrast. Could the M 83 void be a remnant of some tidal interaction or similar dynamical disturbance due to accretion of a low-dust, gas-rich satellite galaxy? We note that M 83, the largest member of its galaxy group, has a large optically detected tidal stream to the north of this region (Malin & Hadley 1997; Pohlen et al. 2004), tracing the disruption of a dwarf galaxy in the strong gravitational field of M 83. These IR–UV properties are not unique to M 83. Other massive galaxies, including M 101 (see Figure 1) and, as noted above, M 31, also exhibit tidal streams and large unveiled (dust-free) UV star clusters and associations (e.g., Thilker et al. 2005).

There is another UV-filled void to the southwest of the nucleus, just beyond the bar cusp, that is somewhat symmetric in location with the northern void relative to the nucleus. Alternative to UV transparency or a simple dust geometric effect, the diffuse UV radiation may arise from older (less massive) star complexes that have either dispersed or blown away their birth cradle environment, revealing open clusters that are dominated by A and B stars (not unlike the Pleiades star cluster). Such regions would be much smaller in area than the northern fork/void discussed above. This mechanism was proposed by Thilker et al. (2007) as one of the explanations for the striking differences observed between the IR and UV emitted by the nearby star-forming galaxy NGC 7331.

Averaging with elliptical–radial axial symmetry, the resulting azimuthal surface brightness profiles of M 83 also reveal the spatial offsets between the UV and IR emission. Figure 11 presents the surface brightness for *WISE* ($W1$ and $W2$) and *Spitzer* (IRAC-1 and IRAC-2), and the addition of *GALEX* (NUV) to the $W3$+IRAC-4 profiles and *GALEX* (FUV) to the $W4$+MIPS-24 profiles. The *WISE* and *Spitzer* magnitudes are in Vega units, and the *GALEX* magnitudes are in AB units plus an offset of −7 mag to fit within the plot. The figure panels also show the double-Sérsic fit to the radial profile (bulge in cyan, disk in blue).

The first panel shows that $W1$ 3.4 μm and IRAC-1 3.6 μm have similar profiles, both reaching depths of 24 mag arcsec^{-2} (corresponding to 26.7 mag arcsec^{-2} in AB). The sharp "bump" at a radius of ∼110″ corresponds to the bright continuum emission arising from the bar end cusps where the gas has piled

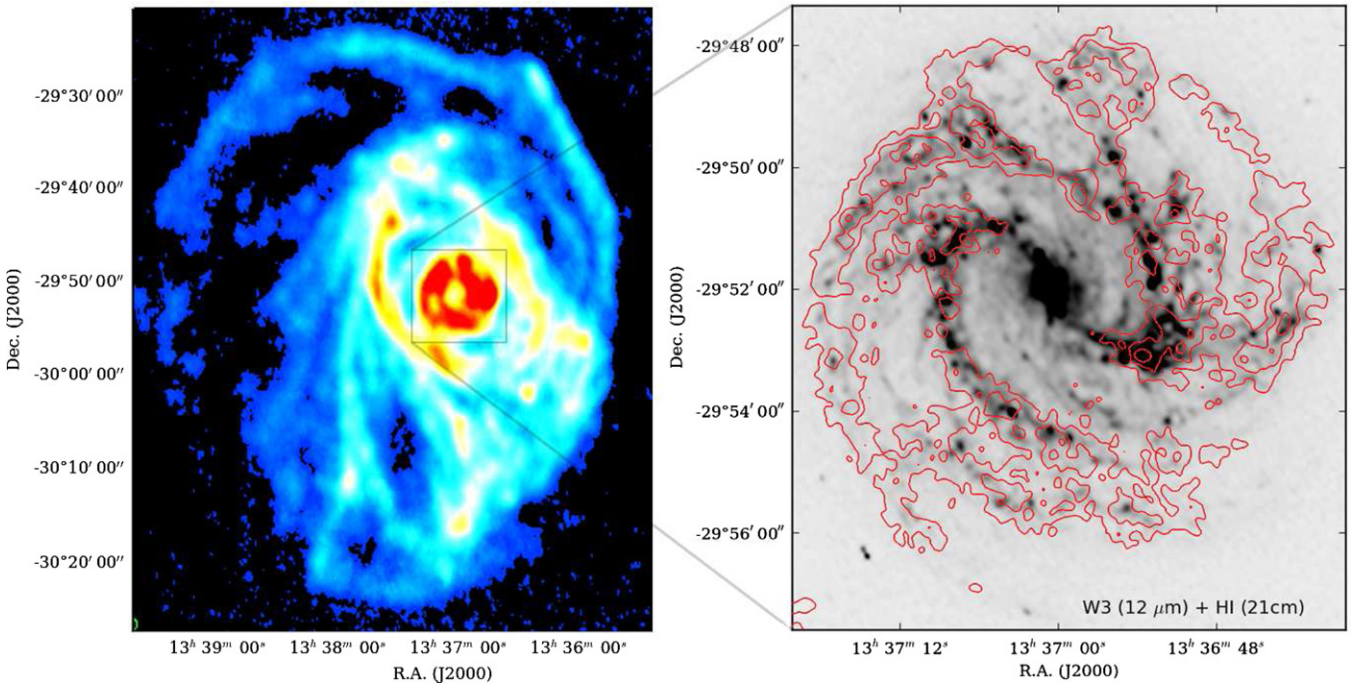

Figure 12. Neutral hydrogen distribution of the southern spiral galaxy M 83. Left: large-scale moment-0 map of the extended H I gas distribution, constructed from mosaic data obtained with both the 21 cm multibeam system on the 64 m Parkes dish and ATCA. Right: ATCA high-resolution H I moment-0 map (red contours) overlaid onto the *WISE* 12 μm map (gray scale, log-stretch) of the central disk (denoted with a gray box in the left panel). The H I contour levels are 0.1, 0.27, 0.43, and 0.6 Jy beam^{-1} km s^{-1}. The ATCA beam is approximately 10″, comparable to the *WISE* 22 μm band, but note that the diffuse gas (see the left panel) is resolved out when emphasizing the longer ATCA baseline measurements.

(A color version of this figure is available in the online journal.)

up from shock focusing, thereby fueling the observed active star formation (Lord & Kenney 1991; see also below). The second panel shows the $W2$ 4.6 μm and IRAC-2 4.5 μm profiles, which are also nicely co-aligned (as expected). The bar end cusps are even more prominent in this view of the mid-IR R-J tail. The $W2$ depth reaches a limit of 23 mag arcsec^{-2} (corresponding to 26.3 mag arcsec^{-2} in AB), while the IRAC-2 is about 1 mag deeper in sensitivity. The third panel shows the $W3$ 12 μm, IRAC-4 8 μm, and *GALEX* NUV+FUV. Both $W3$ and IRAC-4 have the same shape, but are offset slightly due to band-to-band differences between *WISE* and *Spitzer*: we would expect a flux ratio of 1.1 for M 83-type galaxies (e.g., see Figure 21, third panel). The $W3$ depth reaches a limit of 19.4 mag arcsec^{-2} (corresponding to 24.6 mag arcsec^{-2} in AB). In the UV window, the profiles have considerably different shape; notably, the absence of UV emission in the central core (note the shallow profiles between 15″ and 80″ radius) and the bar cusps have shifted outward by 15″–20″ (∼0.5 Kpc), exhibiting a more pronounced, localized or compact, signal relative to the IR. The UV light then falls off steeper than the IR light between 200″ and 800″, but thereafter it remains constant and extends well beyond the IR disk, to radii exceeding (>1000″), punctuated by dense knots that are unmistakable markers for star formation. The last panel shows the $W4$ 22 μm, MIPS 24 μm, and *GALEX* NUV+FUV. $W4$ exhibits sharper profiles than MIPS-24 (note the dip at 30″) and extends to lower levels because the MIPS-24 mosaic is not large enough to capture all of the light from M 83. The $W4$ depth reaches a limit of 18.5 mag arcsec^{-2} (corresponding to 25.1 mag arcsec^{-2} in AB). Likewise with the $W3$ comparison to the UV, the $W4$ band appears shifted relative to the *GALEX* bands, although it is not as distinct as the 12 μm comparison.

To summarize our IR–UV imaging results thus far: although there is a clear physical connection between the star formation activity and the warm dust emission arising from the ISM, the M 83 IR-to-UV flux ratio diagram and surface brightness profiles emphasize that the distribution of young stars and UV diffuse emission is only partially correlated with mid-IR radiation, emphasizing the importance of tracking the obscured (IR) and unobscured (UV) star formation. We next investigate the IR to gas connection.

5.2. M 83: Radio H I and Infrared Connection

The neutral hydrogen gas reservoir of M 83 extends ∼1° (80 kpc) in length, containing a HIPASS-measured total of 8.3 × 10^9 $M_\odot$ of H I (Koribalski et al. 2004). Another 4 × 10^9 $M_\odot$ of molecular hydrogen resides in the central interior and bar of M 83 (Lundgren et al. 2004, 2008, for a distance of 4.66 Mpc). The total dynamical mass is estimated to be 6 × 10^{10} $M_\odot$ (Lundgren et al. 2008) and 8 × 10^{10} $M_\odot$ (Crosthwaite et al. 2002).

We have obtained new high spatial resolution 21 cm imaging of the M 83 region using the Australia Telescope Compact Array (ATCA) as part of the Local Volume H I Survey (LVHIS; Koribalski 2010), and in combination with single-beam observations using the Parkes 64 m dish,[22] constructed a map of the H I distribution that is comparable in resolution to that of *WISE* and *GALEX* (10″ versus 5″). Figure 12 presents the neutral gas distribution of M 83, viewed to its fullest extent (left panel) and focusing on the inner disk in which the IR is detected (right panel). At the largest scales, the gas is well extended beyond the optical/IR disk, forming a warped structure that indicates

[22] Applying uniform weighting of the uv-data gives more weight to the longest baselines in the compact array ($\lesssim$6 km).

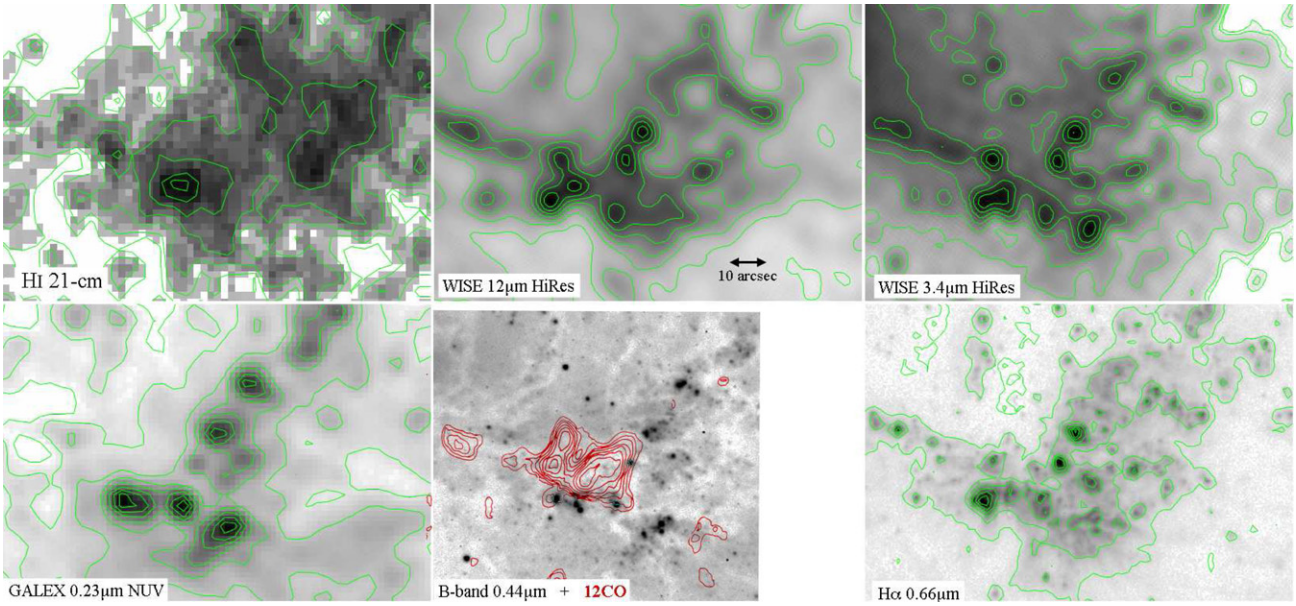

Figure 13. Close-up view of the southwestern bar cusp of M 83, centered on J2000 coordinate $13^h36^m52^s.86$, $-29^d52^m55^s.3$. Clockwise starting from left: high spatial resolution 21 cm image (ranging from 0.01 to 0.60 Jy km s^{-1}, *WISE* HiRes 12 μm, *WISE* HiRes 3.4 μm, Hα, *B* band (with 12CO contours), and *GALEX* NUV. The green contours emphasize the gray-scale contrast. Overlaying the *B*-band image, the red contours are 12CO(1–0) with levels 2, 3, 4, 5, 6, 7, 8, 9 × 2.3 Jy km s^{-1} (Kenney & Lord 1991). At the distance of M 83, the physical scale of 10″ is 213 pc.

(A color version of this figure is available in the online journal.)

tidal disturbance. To the north, a long H I filament corresponds spatially and kinematically to the tidal stream of stars tracing a dwarf galaxy that is shredding and spiraling into the M 83 gravitational well. The highly asymmetric extended gas distribution suggests that other small galaxies may also be accreting onto the disk.

Closer to the central region, more ordered spiral arms are discerned. The right panel of Figure 12 shows the H I overlaid (red contours) on the *W*3 12 μm image. The spatial correspondence between the neutral gas and the integrated (line of sight) PAH–ISM emission is striking: except for the nuclear region, where the H I is absent (having been converted to molecular gas for consumption), the atomic hydrogen traces the current star formation on large angular scales. Since it is the molecular hydrogen gas that serves as the primary fuel for star formation, we would not necessarily expect the neutral hydrogen to be so closely correlated with the PAH emission arising from PDRs and H II regions (e.g., see below). However, the Kennicutt–Schmidt Law (K-S; Kennicutt 1989), which relates the SFR surface density to the gas surface density, tells us that the total gas (neutral plus molecular) controls the star formation—here traced by the 12 μm maps, which highlight the sites of enhanced star formation density.

This gas-to-IR dependence is further emphasized in the extended Schmidt Law detailed in Shi et al. (2011). High-resolution maps of molecular CO emission (tracing the cold H_2 distribution) show concentrated, clumpy associations that trace the embedded star formation, particularly along the inner eastern arm (see Lord & Kenney 1991; Rand et al. 1999). What leads to the strong correlations between neutral H I and the IR emission? Beyond replenishment through accretion and bar-directed feeding from the massive H I reservoir, Tilanus & Allen (1993; see also Lundgren et al. 2008) propose that the atomic hydrogen in the central disk of M 83 is in fact the byproduct of molecular hydrogen that has been dissociated by the strong radiation fields arising from the massive star formation in the spiral arms. The gas is likely to pass though many neutral to molecular to neutral cycles during the lifetime of star formation in the spiral arms. In any event, it is clear that the interplay between molecular gas and neutral gas can produce a complex physical association with the SFR and its efficiency.

To investigate the gas to mid-IR emitting dust relationship at the finest scales that our multi-wavelength data enable, we zoom into the southwest bar transition zone, located roughly at $13^h36^m52^s.86$, $-29^d52^m55^s.3$ (J2000). The region contains several massive star formation complexes, as revealed in Figure 13, generating strong radiation fields that heat the gas and dust that has funneled into this region, recently mapped with far-IR imaging from *Herschel* (cf. Foyle et al. 2012). The neutral gas content is represented by the H I 21 cm map (upper left), and the molecular gas by the ^{12}CO contours (red). The obscured star formation is traced by the PAH emission as seen at 12 μm, and the unobscured star formation by the UV and Hα imaging. Finally, the evolved population emission peaks in the near-IR, here represented by *W*1 3.4 μm. The "cusp" is clearly evident with these probes, the bar ends at center and then promptly turns to the northwest as it transitions to the massive spiral arm that gives M 83 its distinctive morphology. It is clear that the molecular gas (red contours) more closely aligned with the star formation (both *W*3 and the UV) than the neutral gas; nevertheless, the total gas is concentrated in the same area as the bright star formation knots. The density wave and bar kinematics have focused the fuel that is now driving the star formation. The *B*-band image, whose angular resolution discerns features as small as 10 pc, exhibits dark dust lanes that represent the thickest concentrations of gas, roughly outlining the UV (transparent) knots and coincident with the *W*3 IR (obscured) emission. The recombination Hα shows that the star formation complex breaks into several small clumps bathed in diffuse emission that *W*3 clearly detects. Kenney & Lord (1991) make the case that the southwest bar cusp is composed of distinct kinematic gas components that originated from different regions of the disk but have streamed

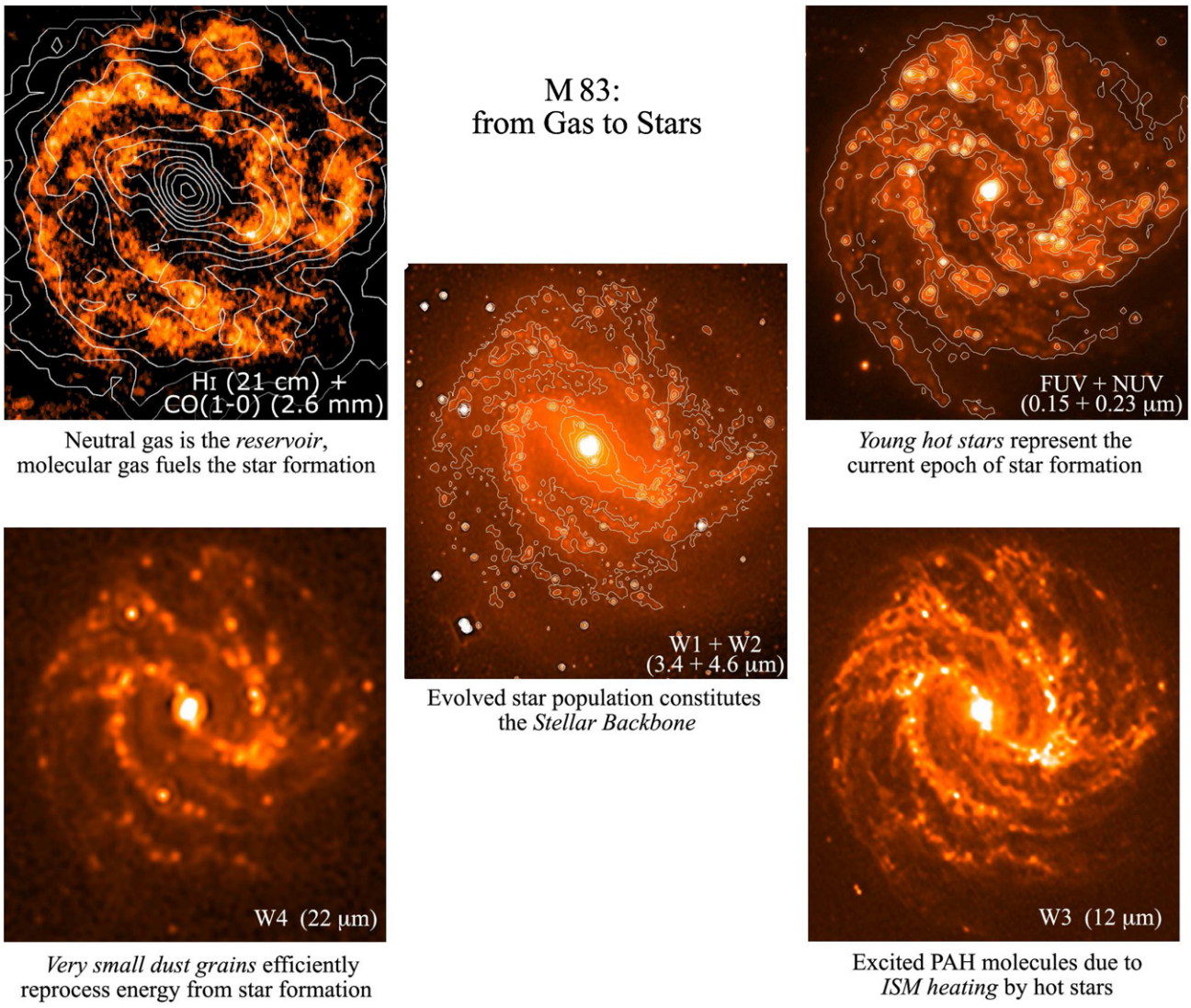

Figure 14. Many faces of M 83, highlighting the evolution from gas to stars. The 10′ panels show: the neutral (H I gray scale) and molecular hydrogen (CO contours) gas content, massive star formation as viewed by *GALEX* NUV (gray scale) and FUV (white contours), *WISE* view of 11.3 μm PAH emission ($W3$ band) and reprocessed starlight ($W4$ band) both associated with star formation, and the center panel shows the stellar distribution of the previous generations of star formation as viewed with the $W1$ (3.4 μm; gray scale) and $W2$ (4.6 μm; white contours) bands. The CO(1–0) is from Crosthwaite et al. (2002).

(A color version of this figure is available in the online journal.)

into the transition zone forming dense molecular clouds. The red contours also show that they are spatially distinction, resolved by both *WISE* and *GALEX*. A wealth of information is provided by the multi-wavelength data sets presented here, highlighting the importance of extracting both spatial and spectral elements to study and decode the physics in star formation.

5.3. M 83: From Gas to Stars

Understanding the process that fuels the star formation, requires both the neutral and molecular hydrogen content be mapped and studied with respect to the young, hot population of stars (*GALEX*) and the ISM that responds to the energy input (*WISE* and *Spitzer*). Figure 14 summarizes the evolution from gas to stars using the maps presented in this work, starting in the upper left and moving clockwise, completing the cycle in the center panel. We start with the fuel: the primordial H I combines to form molecular H_2, which gravitationally collapses (e.g., via spiral density waves) to form new stars. Massive O and B stars radiate copious amounts of UV photons, which are detected by *GALEX* in the FUV and NUV bands. Most of the radiation, however, is scattered and absorbed by dust grains that are distributed throughout the spiral arms and birth clouds. The radiation excites the complex PAH molecules that form on dust grains located outside of H II regions. These photodissociation regions are detected by *WISE* in the $W3$ 12 μm band and by *Spitzer* in the IRAC 8 μm band. The radiation warms small dust grains to temperatures of ∼100–150 K, radiating (modified blackbody) photons in the mid-IR window that is detected by *WISE* with the $W4$ 22 μm band and by *Spitzer* with the MIPS 24 μm band. Over time the stars disperse from their birth clouds, becoming visible to detection at optical wavelengths. Massive stars burn hot and bright, living for only a few to tens of millions of years before exploding and sending their gas back into the ISM for recycling. Less massive stars live much longer: solar-type stars burn for billions of years, evolving into luminous red giants. These stars, far more numerous that the massive O and B stars, form the aggregate massive backbone of the galaxy. These cool giants emit most of their photospheric radiation in the near-IR window, detected and studied by *WISE* with the $W1$ 3.4 μm and $W2$ 4.6 μm bands and by *Spitzer* with the IRAC

Table 5
Broadband Spectral Luminosities

Name	K_s 2.2 μm log ($\nu L_\nu/L_\odot$)	$W1$ 3.4 μm log ($\nu L_\nu/L_\odot$)	$W2$ 4.6 μm log ($\nu L_\nu/L_\odot$)	$W3$ 12 μm log ($\nu L_\nu/L_\odot$)	$W4$ 22 μm log ($\nu L_\nu/L_\odot$)	MIPS 24 μm log ($\nu L_\nu/L_\odot$)	FUV 0.16 μm log ($\nu L_\nu/L_\odot$)	NUV 0.23 μm log ($\nu L_\nu/L_\odot$)
NGC 584	10.101	9.586	9.183	8.178	7.513	7.440	7.910	8.387
NGC 628	9.559	9.225	8.887	9.220	8.911	8.883	9.494	9.463
NGC 777	10.594	10.176	9.794	8.834	8.039	7.988	8.739	8.892
NGC 1398	10.498	10.027	9.650	9.477	8.846	...	9.384	9.401
NGC 1566	9.677	9.273	8.922	9.161	9.048	9.004	9.455	9.388
NGC 2403	9.110	8.791	8.462	8.693	8.505	8.442	9.293	9.226
NGC 3031	10.099	9.652	9.262	8.925	8.457	8.454	9.172	9.145
NGC 4486	10.585	10.236	9.845	8.861	8.412	8.309	9.047	9.200
NGC 5194	10.116	9.685	9.353	9.808	9.566	9.550	9.759	9.796
NGC 5195	9.814	9.359	8.983	8.702	8.574	8.601	8.295	8.464
NGC 5236	9.963	9.587	9.248	9.613	9.578	9.558	9.639	9.688
NGC 5457	9.969	9.567	9.233	9.542	9.251	9.226	10.023	9.944
NGC 5907	10.264	9.815	9.472	9.619	9.281	9.264	9.132	9.145
NGC 6118	...	9.455	9.101	9.294	8.939	...	...	...
NGC 6822	7.188	7.127	6.754	6.408	6.175	6.137	7.727	7.728
NGC 6946	9.934	9.543	9.213	9.674	9.480	9.472	9.821	9.850
IC 342	9.710	9.362	9.018	9.387	9.239	9.184	9.797	9.654

Notes. The νL_ν luminosity (normalized by the total solar luminosity) is derived from the integrated flux density and the distance listed in Table 1, where the luminosity uncertainty is completely dominated by the distance uncertainty; assuming a distance uncertainty of 5%, it follows that the luminosity uncertainty is 10%. The fluxes have been corrected for the Galactic extinction and the expected internal extinction. The K_s flux densities are from the 2MASS Large Galaxy Atlas (Jarrett et al. 2003).

3.6 μm and 4.5 μm bands. While some galaxies undergo dynamical interactions (e.g., within group and cluster environments), the basic ingredients and processes that drive M 83, sketched in Figure 14, are how galaxies form and evolve over vast stretches of time.

6. STAR FORMATION RATE

Both the present SFR and total stellar mass (M_*) are fundamental parameters for the study of galaxy evolution. Direct comparison of the global SFR (from the *WISE* long-wavelength bands) with stellar mass (short-wavelength bands) enumerate the present-to-past star formation history, or effectively, how fast the galaxy is building. This specific SFR (sSFR) is a critical metric of morphological evolution. In this section, we explore the SFR and stellar mass properties of our large galaxy sample, providing a preliminary prescription for estimating these quantities from the spectral luminosities. We focus on the global properties in this work, with an extension to much larger samples and to more detailed work on the internal star formation, gas, and stellar density properties left to future work. Table 5 presents the νL_ν luminosity densities for the near-IR (2MASS K_s band), mid-IR (*WISE* and MIPS-24) and *GALEX* FUV/NUV, corrected for foreground Galactic extinction and the expected internal extinction (see Section 4.2.1). The expected uncertainty in the luminosity is ~10%, assuming 5% uncertainty in the distance estimate. Here the νL_ν values have been normalized by the total solar luminosity ($L_\odot$): 3.839×10^{33} erg s^{-1}.

To convert the luminosities to the "in-band" equivalent,[23] scale the νL_ν by a factor of 7.37, 22.883, 58.204, 38.858, and 282.50 for the K, $W1$, $W2$, $W3$, and $W4$ bands, respectively, where the scaling factor takes into account the difference between the total solar luminosity and the in-band value (as measured by the 2MASS and *WISE* bands; see section below on stellar masses).

For nearby galaxies, the present star formation is traditionally studied using tracers of massive stars, notably Balmer emission arising from H II regions (e.g., Kennicutt 1998), which requires significant extinction corrections to account for absorbed or scatter light. With the advent of space-based UV observations of galaxies in the local universe, notably from *GALEX*, these studies are now carried out on large, diverse, and statistically significant samples. Since the UV photons originating from or associated with hot, young stars are predominately absorbed by dust grains and re-radiated at longer wavelengths, the IR window may be used to effectively trace the underlying star formation, although ideally a combination of the IR and *GALEX* UV provides the most complete estimate. Studies using *IRAS*, *Infrared Space Observatory*, and *Spitzer* observations have correlated the mid- and far-IR emission with the present young stellar population that is embedded within molecular clouds that embody spiral arms and disks of galaxies. Most relevant to *WISE*, global SFRs may be directly estimated using the warm dust grain and integrated PAH emission (alternatively, gas column density-normalized PAH emission) or combinations of UV or Hα and IR tracers to capture both the unobscured and obscured star formation (Calzetti et al. 2007; Leroy et al. 2008; Calzetti 2011; Kennicutt et al. 2009; Rieke et al. 2009; Treyer et al. 2010). Below we present both IR and combined IR+UV SFRs.

We establish the global *WISE* $\mathrm{SFR_{IR}}$ relation by bootstrapping from the well-studied MIPS-24 relation (e.g., Calzetti et al. 2007; Rieke et al. 2009; Rujopakarn et al. 2012). Although using only the 24 μm luminosity to estimate the $\mathrm{SFR_{IR}}$ is not as accurate as using the L_{TIR}, or some combination of IR, UV, and optical, it still provides a tight correlation for galaxies with moderate to high metallicities (but see Relaño et al. 2007 for SFR analysis of individual H II regions). Using the Rieke et al. (2009) relation to derive the $\mathrm{SFR_{IR}}$ from MIPS-24 luminosity,

[23] The "in-band" luminosity, L_λ should not be confused with the "spectral" luminosity (νL_ν). The M/L ratio is calibrated using the in-band luminosity: the computed luminosity (as measured in the band) normalized by the absolute solar luminosity as measured in the band. We derive the absolute in-band magnitude of the Sun: 3.32, 3.24, 3.27, 3.23, and 3.25 mag for K_s, $W1$, $W2$, $W3$, and $W4$, respectively; we will refer to these luminosities as L_K, L_{W1}, etc.

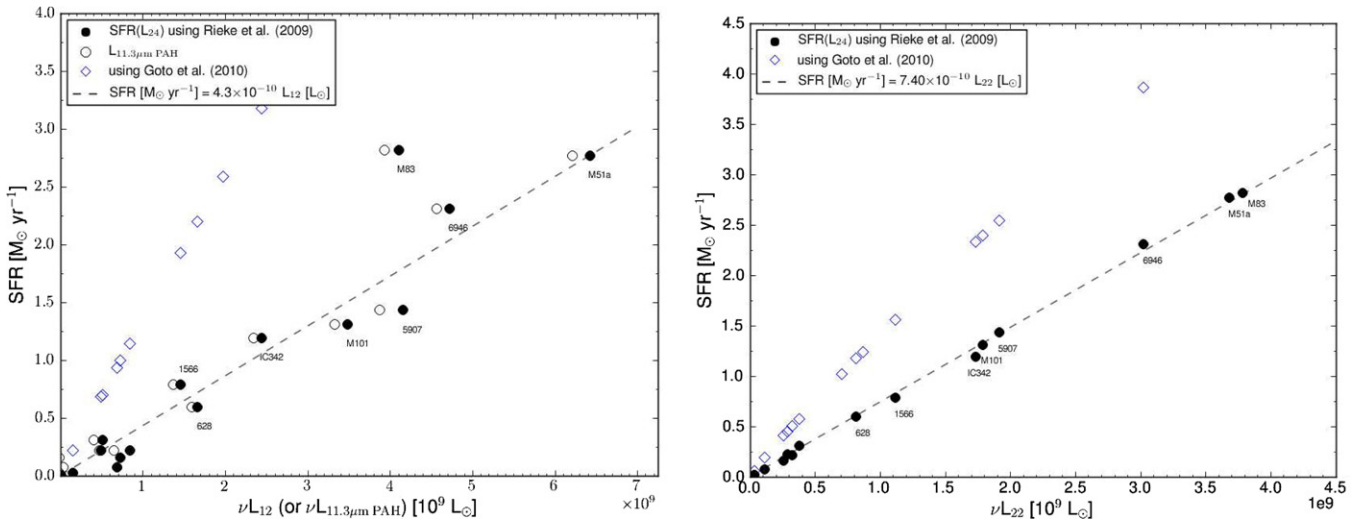

Figure 15. Correlating the SFR with the *WISE* mid-IR luminosity. The global SFR_{IR} is derived from the MIPS 24 μm luminosity and the Rieke et al. (2009) calibration. Left: the global SFR_{IR} as a function of the *WISE* 12 μm luminosity (filled circles) and the integrated 11.3 μm PAH luminosity (open circles). Right: the global SFR_{IR} as a function of the *WISE* 22 μm luminosity. A simple linear fit to the data is shown (dashed line). The galaxy name is indicated below the measurement, where single numbers represent the NGC #.

(A color version of this figure is available in the online journal.)

we plot the *WISE* νL_{12} and νL_{22} against the MIPS-estimated SFR_{IR} (Figure 15). For the SFR range between 0 and 3, we find the best-fit νL_{12} and νL_{22} relations to be

$$WISE\ W3:\ \mathrm{SFR_{IR}}\,(\pm 0.28)\,(M_\odot\ \mathrm{yr}^{-1}) = 4.91(\pm 0.39)\times 10^{-10}\,\nu L_{12}(L_\odot), \quad (1)$$

$$WISE\ W4:\ \mathrm{SFR_{IR}}\,(\pm 0.04)\,(M_\odot\ \mathrm{yr}^{-1}) = 7.50(\pm 0.07)\times 10^{-10}\,\nu L_{22}(L_\odot). \quad (2)$$

The rms scatter between the MIPS-estimated SFR_{IR} and the *WISE* SFRs (Equations (1) and (2)) is 0.28 and 0.04 $M_\odot$ yr^{-1}, for SFR (12 μm) and SFR (22 μm), respectively; the actual uncertainty in any given *WISE*-derived SFR is at least 10% given the uncertainty in the luminosity. As expected, there is a very tight relation between the *WISE* νL_{22} and the Rieke SFR_{IR}, since both *WISE* $W4$ and MIPS-24 have very similar bandpasses, tracing the warm ISM dust continuum. Conversely and similar to the larger scatter observed in the IRAC 8 μm-to-SFR relation (Calzetti et al. 2007), the *WISE* νL_{12}-to-SFR_{IR} relation exhibits a trend that reflects the complex relationship of combined thermal dust + silicate absorption + PAH emission with star formation activity. The strength of the PAH emission bands depends on the metallicity, column density of gas, and ionizing radiation field from the young stellar population (Engelbracht et al. 2008; Draine 2011), but the 11.3 μm PAH can also be excited by spatially diffuse, evolved (~Gyr) stellar population (Calzetti 2011). Nevertheless, the νL_{12} relation is very useful to have because the $W3$ (12 μm) band is so much more sensitive than the $W4$ (22 μm) band, and often, for galaxies beyond the local universe, is the only detection from *WISE*.

We have attempted to isolate the line-of-sight integrated PAH emission in the $W3$ band from the underlying continuum by subtracting from the $W3$ a scaled version of $W1$, representing the R-J stellar light. Note that we are ignoring the warm-dust emission in $W3$ that arises from the dust shells of AGB stars and from AGN; these potentially important components are further discussed below. Using the three elliptical galaxies in the sample, which trace only the photospheric continuum contribution, we determine that the $W3$ to $W1$ scale factor is ~15% (which may be compared with the IRAC-4 to IRAC-1 ratio of 23%; Helou et al. 2004). The resulting νL_{PAH} is shown in Figure 15 as open circles. The scatter in the SFR ($\nu L_{11.3\,\mu m\,PAH}$) relative to the Rieke SFR_{IR} is slightly smaller, 0.26 $M_\odot$ yr^{-1} but still much larger than the SFR (22 μm) distribution. For comparison we also show the SFR estimated using the Goto et al. (2011) relation, which attempts to adapt the SINGS 8 and 24 μm luminosity-to-L_{TIR} relation to the expected *WISE* $W3$ and $W4$ bandpasses. The Goto et al. (2011) SFRs are very likely overestimated, ~2× larger than those predicted by Rieke et al. (2009) for 22 μm and ~3× larger for 12 μm.

We stress that the relations presented here (Equations (1) and (2)) are only preliminary due to the small size of our sample. A more thorough investigation should involve a larger sample, that includes a wide range in metallicity and νL_{IR} (e.g., SINGS sample), calibrating the *WISE* luminosities to the SFR derived through UV, IR, and hydrogen recombination line analysis as with Calzetti et al. (2007) and Kennicutt et al. (2009). A final important caveat: even with a more complete sample to establish the *WISE* SFR relations, the mid-IR is sensitive to only the warm tracers of star formation (PAHs, small dust grains), and thus represents a lower limit to the total IR SFR that also includes the heavily obscured star formation in dense molecular cores, best traced by the far-IR emission (e.g., observations from *IRAS*, *Herschel*, and *AKARI*).

For the galaxy sample, the IR SFRs are estimated using the empirical relations, Equations (1) and (2), and are listed in Table 6. They trace the dust-obscured star formation activity, which is dependent on the dust geometry and total gas/dust column density. For the UV photons—associated with young massive stars—that manage to escape the galaxy, *GALEX* may be used to estimate the unobscured star formation; Table 6 lists the SFR estimated from the FUV and NUV extinction-corrected measurements as follows. Buat et al. (2008, 2011) calibrate the FUV SFR, characterizing it in terms of the *GALEX* luminosity as follows: $\log \mathrm{SFR_{FUV}} = \log(\nu L_{FUV}/L_\odot) - 9.69$. The SFR based on the NUV luminosity density is provided by Equation (6) of

Table 6
Infrared and Ultraviolet Global Star Formation Rates

Name	SFR_{IR} (12 μm) ($M_\odot$ yr^{-1})	SFR_{IR} (22 μm) ($M_\odot$ yr^{-1})	SFR_{IR} (24 μm) ($M_\odot$ yr^{-1})	SFR_{FUV} (0.15 μm) ($M_\odot$ yr^{-1})	SFR_{NUV} (0.23 μm) ($M_\odot$ yr^{-1})	SFR_{tot} (IR+UV) ($M_\odot$ yr^{-1})
NGC 584	0.1	$<10^{-2}$	$<10^{-2}$	$<10^{-2}$	$<10^{-2}$	$<10^{-2}$
NGC 628	0.8	0.6	0.6	0.6	0.6	1.1
NGC 777	0.3	0.1	0.1	0.1	0.2	0.2
NGC 1398	1.5	0.5	...	0.5	0.5	0.9
NGC 1566	0.7	0.8	0.8	0.6	0.5	1.3
NGC 2403	0.2	0.2	0.2	0.4	0.3	0.6
NGC 3031	0.4	0.2	0.2	0.3	0.3	0.5
NGC 4486	0.4	0.2	0.2	0.2	0.3	0.4
NGC 5194	3.1	2.8	2.8	1.2	1.2	3.5
NGC 5195	0.2	0.3	0.3	0.0	0.1	0.3
NGC 5236	2.0	2.8	2.8	0.9	1.0	3.2
NGC 5457	1.7	1.3	1.3	2.2	1.7	3.3
NGC 5907	2.0	1.4	1.4	0.3	0.3	1.5
NGC 6118	1.0	0.7	...	...	...	<1
NGC 6822	$<10^{-2}$	$<10^{-2}$	$<10^{-2}$	$<10^{-2}$	$<10^{-2}$	$<10^{-2}$
NGC 6946	2.3	2.3	2.3	1.4	1.4	3.2
IC 342	1.2	1.3	1.2	1.3	0.9	2.4

Notes. SFR_{IR} (12 μm) = 4.9 × 10^{10} L_{12} ($L_\odot$) and SFR_{IR} (22 μm) = 7.5 × 10^{10} L_{22} ($L_\odot$) (see Figure 15). SFR_{IR} (24 μm) is derived from $L_{24\,\mu m}$ and Equations (10) and (11) of Rieke et al. (2009). The UV rates are estimated from the FUV luminosity (using the relation from Buat et al. 2008, 2011) and the NUV luminosity density (using the relation from Schiminovich et al. 2007). The total UV+IR SFR, characterized as $(1-\eta)SFR_{IR} + \gamma SFR_{FUV}$, where η is the fraction of mid-IR light that originates from the dust shells of AGB stars and γ scales the UV transparency; here, η is assumed to be 0.17 and γ is unity (see Elbaz et al. 2007 and Buat et al. 2011).

Schiminovich et al. (2007): $SFR_{NUV} = 10^{-28.165}\,L_{NUV}$ (erg s^{-1} Hz^{-1}). For the sample, about half of the UV SFRs are larger or comparable to the estimates using the IR tracers, which verifies the importance of accounting for the unobscured star formation. Combining both UV and IR estimates, the "total" SFR may be characterized (Elbaz et al. 2007; Buat et al. 2011) as $(1-\eta)SFR_{IR} + \gamma SFR_{FUV}$, where η is the fraction of mid-IR light that originates from the dust shells of AGB stars and γ scales the UV transparency. In effect, the value of η will depend on the fractional number of AGB and intermediate, post-starburst stars (ages 1–3 Gyr) that contribute to the mid-IR light; Buat et al. (2011) compute an ensemble average value of 0.17 for η using a large sample of field galaxies. Adopting the Buat et al. (2011) values for η (0.17) and γ (unity), the UV+IR SFR is listed in the last column of Table 6, and is generally larger (∼10%–20%) of the IR component. So, for example, consider the SFR of NGC 5236 (M 83): Reported in Section 5, the extinction-corrected integrated FUV flux is 10.11 mag (325 mJy), translating to a luminosity of 4.4 × 10^9 $L_\odot$. Using the relation of Buat et al. (2011), the M 83 SFR_{FUV} is then 0.9 $M_\odot$ yr^{-1}, or roughly 1/3 of the estimate SFR_{IR} (Table 6), assuming γ is unity, and using the average η value, the total SFR would then be ∼3.3, which is 14% greater than the reported SFR_{IR}. We note that the resulting total SFRs have values that are generally 5%–50% larger than the tabulated values in Leroy et al. (2008), but are systematically much smaller than the SFRs predicted using the combined *GALEX* FUV+MIPS(24) relation in the same work (Equation (D10) of Leroy et al. 2008).

The global SFRs are graphically presented in Figure 16, where we compare with the neutral hydrogen gas content to demonstrate the essential star formation efficiency trend of the K-S scaling relation, connecting the star formation density to the total gas density. Although the H I is usually associated with the diffuse IR emission, while the molecular gas (as traced by CO and HCN emission) is more closely associated with star formation, we demonstrated in the last section that the obscured star formation in M 83 is associated with the neutral gas distribution. And indeed, we observed a clear trend (rms scatter ∼ 1 $M_\odot$ yr^{-1}) in both SFR_{IR} and SFR_{tot} and the H I mass. Also shown in the figure is the trend quantified using the SINGS sample and a nearby high-H I mass galaxy (Cluver et al. 2010) that covered a much larger range in neutral gas mass, 10^7–10^{11} $M_\odot$. The slope in the SFR-to-gas trend will increase if the contribution from the molecular gas is included:

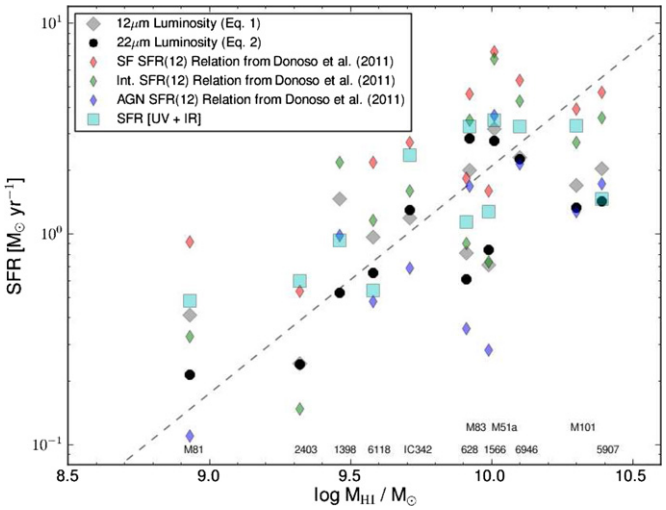

Figure 16. Global SFRs derived from the *WISE* 12, 22 μm and *GALEX* FUV and NUV luminosities, compared to the neutral hydrogen content (see Table 6 for details). For comparison, also shown are the SFRs that follow from the Donoso et al. (2012) 12 μm relations of starburst, intermediate, and AGN galaxy types. The dashed line corresponds to the trend observed in the SINGS sample (Cluver et al. 2010).

(A color version of this figure is available in the online journal.)

gas-rich galaxies have higher fractions of molecular gas (e.g., 25%–50% of the total gas), while gas-poor galaxies have much lower fractions of H II (e.g., Leroy et al. 2008; see also the COLDGASS scaling relations in Saintonge et al. 2012). The highest global SFRs belong to M 51a, M 83, M 101, and NGC 6946, while the lowest rates belong to the elliptical galaxies and the dwarf NGC 6822. The lower the H I content, the smaller the IR luminosity (and hence, SFR as predicted by the global K-S relation), while the most luminous disk galaxies have the highest gas content. The H I reservoir feeds and builds the molecular hydrogen reservoir, which is what ultimately fuels the star formation and slowly builds the stellar mass of the galaxy (see below for discussion of the scaling relation between SFR and M_*).

For comparison purposes, Figure 16 includes the IR SFRs derived using the relations given by Donoso et al. (2012), who cross-matched *WISE* 12 μm fluxes with SDSS photometry and spectroscopy of a large, statistically significant sample of nearby galaxies ($\bar{z} \sim 0.08$). The 12 μm emission is sensitive to both recent SF (~few hundred 10^6 yr) and to star formation averaged over Gyr timescales. Moreover, the emission may arise or be associated with AGN as well as the host itself. Consequently, they separated their matched sample into star-forming, intermediate, and type-2 AGN, calibrating the SFR based on optical emission lines with the *WISE* 12 μm luminosity. Using these three relations applied to the WERGA galaxy sample $W3$ luminosities, the Donoso et al. relation SFRs are consistent with the calibrated SFRs from this work (Equations (1) and (2)). Specifically, the star formers (red diamonds) tend to have the highest SFRs and are 20%–30% larger than those derived in this work (Equation (1)), intermediates (green diamonds) are most consistent with the WERGA sample, and the AGN types (blue diamonds) have the lowest SFRs, but still in line with the overall scatter in $W3$. They point out that most of the 12 μm emission arises from the young stellar populations, <0.6 Gyr in age, consistent with the M 83 analysis comparing in detail the $W3$ distribution relative to the UV and radio emission (see Section 5). For the earlier type galaxies, however, the AGN types have 12 μm emission that is dominated by the older, evolved stars (including the AGB population), with ages between 1 and 3 Gyr. As we show below, these populations are an important component in the simple stellar population (SSP) models that are used to derive the underlying stellar mass that is traced by the near-IR 1–5 μm emission. The larger scatter seen in the $\mathrm{SFR_{IR}}$ based on the *WISE* 12 μm (or the IRAC 8 μm) emission relative to the SFR based on the *WISE* 22 μm (or MIPS 24 μm) emission is a consequence of the different emission mechanisms (AGN, PDR, and stellar) and metallicity that augment the mid-IR PAH emission strength. Nevertheless, in the absence of reliable SF tracers (e.g., extinction-corrected Hα luminosity, 22 or 24 μm luminosity, L_{TIR}, or radio 20 cm continuum), the $\mathrm{SFR_{IR}}$ based on *WISE* 12 μm provides an adequate proxy for the star formation activity.

7. STELLAR MASS ESTIMATION

Most of the baryons that comprise a galaxy are locked up in the evolved stellar population, low-mass (~solar) stars that emit the bulk of their light in the 1–3 μm near-IR window. A photometric census of this population of cool K and M giants, in combination with the mass-to-light ratio (M/L), renders an estimate of the total baryonic stellar mass for a galaxy. This simplistic prescription for deriving the stellar mass is complicated by individual variations in the initial mass function (IMF), star formation history and population ages, metallicity, dust extinction, AGB (notably the luminous thermal pulsating stars) contributions, and nuclear activity. Nevertheless, there are many studies that have successfully employed both optical and near-IR (2 μm) observations (e.g., 2MASS) to conduct statistical studies of the extragalactic stellar mass-to-light relation (see Bell et al. 2003; Zibetti et al. 2009). With the advent of *Spitzer*/IRAC imaging of nearby galaxies, the emphasis is now turning to the mid-IR 3 and 5 μm window of the R-J distribution, with the major advantages being the superior sensitivity to lower surface brightness emission (thus capturing more of the total flux) while less sensitive to the foreground dust extinction. On the other hand, the disadvantage of the mid-IR relative to the near-IR is the added sensitivity to light arising from dust emission associated with star formation and with the evolved population of thermally pulsating AGB stars, both of which will boost the mid-IR luminosity and thereby render an overestimate of the stellar mass (e.g., Meidt et al. 2012). As we shall see below, there is a strong dependence of the M/L ratio on the mid-IR galaxy color, but we caution the results are preliminary and further analysis with a larger sample is paramount.

The *WISE* "in-band" luminosity, L_λ is derived using the equation

$$L(\mathrm{band})/L_\odot = 10^{-0.4(M(\mathrm{band}) - M_\odot(\mathrm{band}))}, \quad (3)$$

where M(band) is the absolute magnitude of the source and $M_\odot$(band) is the absolute magnitude of the Sun as measured in the band. Employing the 2MASS and *WISE* band RSRs (Jarrett et al. 2011), the SEDs of the Sun and Vega (Fukugita et al. 1995), we derive (cf. Oh et al. 2008) the absolute in-band magnitude of the Sun: 3.32, 3.24, 3.27, 3.23, and 3.25 mag for K_s, $W1$, $W2$, $W3$, and $W4$, respectively; these values are used to estimate the stellar mass in conjunction with the M/L ratio.

Recent work that has attempted to derive the M/L calibration for IRAC 3.6 μm and 4.5 μm (usually by bootstrapping from the near-IR) includes Li et al. (2007), Oh et al. (2008), Westmeier et al. (2011), and Zhu et al. (2010). The latter used SWIRE imaging and archival "reference" (stellar) masses that were estimated by combining SDSS photometric data with models from Bruzual & Charlot (2003). The mid-IR M/L that Zhu et al. (2010) present depends on the IRAC luminosities and, to correct for galaxy-to-galaxy variation in the star formation history, on the optical ($g-r$) color (see Equations (6) and (7) in their work). Yet other studies (e.g., Zibetti et al. 2009), employ the latest SSP models of Charlot & Bruzual (see Bruzual 2007) that have an updated treatment of the AGB contribution, although there remains significant disagreement between observations and the new SSP models (e.g., Kriek et al. 2010; see more discussion on this topic below). Another method that was applied to *Spitzer* observations of the Circinus Galaxy (For et al. 2012) combines near-IR derived M/L with conversion to *Spitzer* wavelengths through color conversions and SSP models as follows: using the M/L (K_s) relation derived from the analysis of Bell & de Jong (2001) and stated in Westmeier et al. (2011, see their Equation (8)) and M/L near- to mid-IR transformations from Oh et al. (2008), the IRAC M/L relation in terms of the ($J-K$) color follows

$$\begin{aligned}\text{IRAC } 3.6\,\mu\text{m: } & (M/L)\,(M_\odot/L_\odot) \\ & = (0.92 \times 10^{(1.434\,(J-K_s)-1.380)}) - 0.05\,. \end{aligned} \quad (4)$$

The *WISE* equivalent of this relation follows by applying a small scaling factor (near unity) to convert the *WISE* $W1$

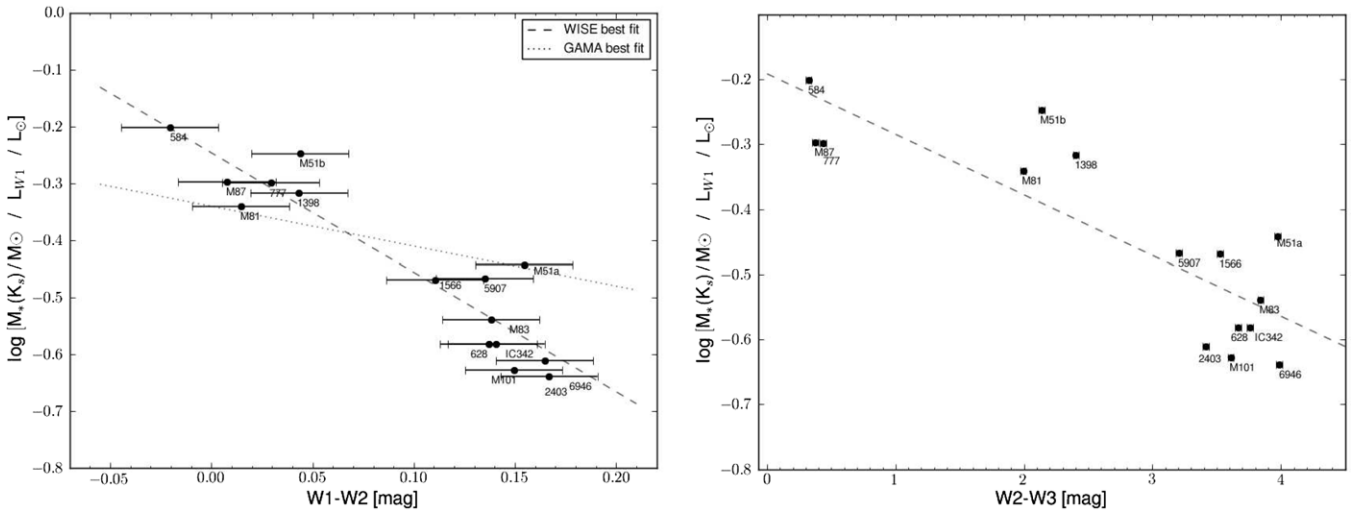

Figure 17. Empirical mass-to-light relation, $(M_\odot/L_\odot)$, derived from *WISE* 3.4 μm in-band luminosity ($W1-W2$ color (left panel), $W2-W3$ color (right panel)) and K_s-derived stellar masses using the Zhu et al. (2010) relation (see also Figure 18). The color error bars represent the formal uncertainties (Table 2) and a 1.5% photometric calibration uncertainty. The linear trend (dashed line) is described by Equations (9) and (10). The dotted line (left panel) represents the $(M_\odot/L_\odot)$ derived for nearby galaxies in the GAMA survey (see the text for details).

flux to equivalent IRAC-1 flux based on the Hubble type (see Figure 21). The *WISE* M/L becomes

$$\textit{WISE}\ 3.4\,\mu\text{m}:\ (M/L)\,(M_\odot/L_\odot) = ((0.92/\zeta_1)\ \times\ 10^{(1.434\,(J-K_s)-1.380)}) - (0.05/\zeta_1)\,. \quad (5)$$

One of the most extensive M/L investigations comes from the S4G study of nearby galaxies (e.g., Meidt et al. 2012; see also Eskew et al. 2012), utilizing sensitive IRAC 3.6 μm and 4.5 μm imaging from the "warm" *Spitzer* Mission. Employing a Chabrier-type IMF (e.g., Chabrier 2003) that is optimal for early-type galaxies, the SSP models of Bruzual & Charlot (2003), and cross-calibrating 2MASS near-IR colors of K/M giants to those measured with *Spitzer*-GLIMPSE, they derive a relation between IRAC-1 3.6 μm M/L and the [3.6]−[4.5] color:

$$\text{IRAC}\,3.6\,\mu\text{m}:\ \log(M/L)(M_\odot/L_\odot) = -0.22 + 3.42([3.6]-[4.5])\,. \quad (6)$$

Although these studies are in preliminary stages, the S4G relation appears to render results that are consistent with other metrics (see below), notably for the early-type galaxies (i.e., dominant R-J emission). The *WISE* equivalent of this relation follows by applying a small scaling factor to convert the *WISE* magnitudes to equivalent IRAC magnitudes. This entails using the zero-point flux to magnitude conversion, and Hubble type and expected *WISE*-to-IRAC flux ratio based on model templates are used to derive the band-to-band scaling factors. The M/L would become

$$\textit{WISE}\ 3.4\,\mu\text{m}:\ \log(M/L)(M_\odot/L_\odot) = -0.75 + 3.42((W1-W2) - 2.5\log(\zeta_2/\zeta_1)), \quad (7)$$

where ζ_1 accounts for the $W1$-to-IRAC-1 band-to-band differences, and ζ_2 accounts for the $W2$-to-IRAC-2 band-to-band differences as per Hubble type. Using elliptical galaxies as an example, the $W1$/IRAC-1 flux ratio is 1.06, and the $W2$/IRAC-2 flux ratio is 0.94, the *WISE* M/L relation is then

$$\textit{WISE}\ 3.4\,\mu\text{m (early types)}:\ \log(M/L)(M_\odot/L_\odot) = -0.31 + 3.42(W1-W2). \quad (8)$$

A more direct, but largely empirical method for using the *WISE* colors to adjust the M/L relation for star formation history effects, is to adopt the stellar "mass" derived using the K_s-band in-band luminosity and compare with the "light" traced by the $W1$ (3.4 μm) luminosity. This hybrid method then correlates the mass with the light in the sense that the K and $W1$ bands are sampling the same stellar population. Accordingly, Figure 17 presents the hybrid $M_*(K_s)$-to-L_{W1} ratio as a function of the $W1-W2$ color and the $W2-W3$ color, where the stellar mass is estimated using the 2MASS K_s in-band luminosity (Jarrett et al. 2003) and the Zhu et al. (2010) relation (their Equation (5)) that includes the $(g-r)$ color correction.[24] It should be stressed that since we have used the Zhu et al. (2010) for the K-band stellar masses, the resultant masses are smaller by ∼0.3–0.4 dex compared to those masses derived using, for example (see Figure 18(a)), Bell et al. (2003), Leroy et al. (2008), and de Blok et al. (2008), due to the Zhu et al. (2010) formulation which uses "reference" stellar masses (see also Kannappan & Gawiser 2007). We see from Figure 17 that the M/L has a clear linear trend with *WISE* color: the M/L is higher for the early types (i.e., bulge-dominated blue galaxies) relative to the late types (star-forming, red galaxies). This trend likely arises from extinction (e.g., dust geometry), metallicity and population age differences. The linear equation that best fits the sample distribution (Figure 17, dashed lines) is

$$\textit{WISE}\ 3.4\,\mu\text{m}:\ \log(M_*(K_s)/L_{W1})(M_\odot/L_\odot) = -0.246(\pm0.027) - 2.100(\pm0.238)(W1-W2); \quad (9)$$

$$\textit{WISE}\ 3.4\,\mu\text{m}:\ \log(M_*(K_s)/L_{W1})(M_\odot/L_\odot) = -0.192(\pm0.049) - 0.093(\pm0.016)(W2-W3). \quad (10)$$

The steepness in the M/L relation with *WISE* color over a relatively short range(-0.02 mag $< W1-W2 < 0.17$ mag) may be influenced by the small sample of "normal" galaxies presented in this work. Comparing to a much larger sample of nearby ($z < 0.1$) galaxies extracted from the Galaxy and

[24] Estimated (∼10%–20%) using SED model templates; see also the Hubble type vs. $(g-r)$ color distribution in James et al. (2008).

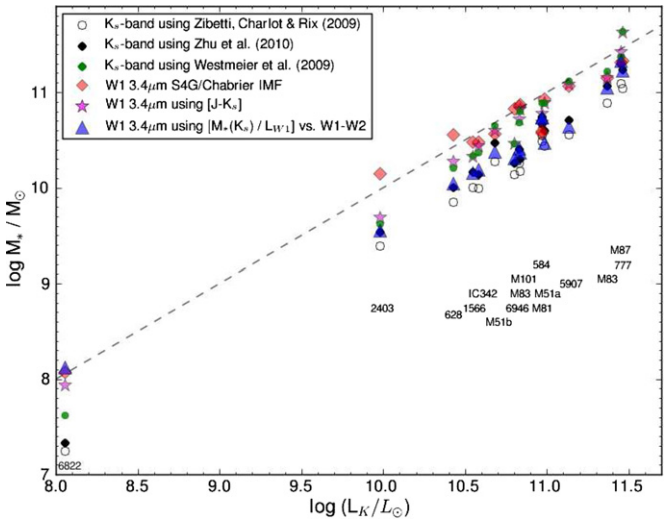

Figure 18. Stellar mass compared to the K_s-band luminosity. The masses are estimated from the K_s, $W1$, and $W2$ luminosities and the M/L relations of Zibetti et al. (2009), Zhu et al. (2010), the S4G/Chabrier IMF relation (Equation (7)), and the M/L relations from this work (Equations (4) and (9); Figure 17). For comparison, the dashed line represents a M/L fraction of unity. (A color version of this figure is available in the online journal.)

Mass Assembly (GAMA; Driver et al. 2011) project from their field G15, the M/L relation as a function of the *WISE* color is much flatter (see dotted line in Figure 17(a); M. E. Cluver et al. 2013, in preparation). The GAMA stellar masses are derived using optical $(g-i)$ colors, stellar population synthesis models and careful Bayesian parameter estimation (Taylor et al. 2011), all of which contribute to the observed *WISE* versus GAMA M/L slope difference; but moreover, the GAMA G15 field has a greater variety of galaxy types, covering a wide range in stellar population (notably giant and AGB relative contributions), metallicity, IMF dust geometry, nuclear activity, and star formation history. We therefore strongly caution that the *WISE* M/L hybrid K-band relation presented in Figure 17 and Equations (9) and (10) should be viewed as preliminary and, at best, incomplete.

Bringing it all together and comparing the different methods introduced here, we estimate the stellar mass for our galaxy sample using the 2MASS K_s-band fluxes (Jarrett et al. 2003) and *WISE* $W1$ and $W2$ fluxes in conjunction with the Bell et al. (2003), Zibetti et al. (2009), Zhu et al. (2010), 2MASS color (Equation (4)), S4G (Equation (7)), and hybrid near-IR to mid-IR (Figure 17) M/L ratios that depend on the *WISE* colors. As noted previously, for the mid-IR relations derived using IRAC photometry, we apply small scaling factors to convert the *WISE* fluxes to equivalent IRAC fluxes. The results are presented in Figure 18, where the derived stellar mass is plotted against the K_s luminosity, currently the most reliable tracer of the evolved stellar population.

The observed scatter between the near-IR methods and those using the hybrid methods is about 0.1–0.2 dex (∼40% rms), with a systematic difference between the two methods of about 0.3–0.5 dex. The masses that are derived from the $J-K$ colors tend to be larger than those derived from the Zibetti et al. (2009) and Zhu et al. (2010, reference mass) treatments. For example, the stellar mass of NGC 6946 is estimated to be $\sim 3.2 \times 10^{10}\ M_\odot$ using the near-IR Bell et al. (2003) formulations (e.g., Leroy et al. 2008; de Blok et al. 2008), and $\sim 1.5 \times 10^{10}\ M_\odot$ using Equation (9). Note that the *WISE* $W1-W2$ adjusted masses (Equation (9)) track closely to the near-IR stellar mass estimates of Zhu et al. (2010), which is to be expected since the *WISE*+2MASS hybrid-relation employs the K_s estimated mass. The S4G/Chabrier values are closest to the Bell et al. (2003) result ($M/L \sim$ unity) for massive galaxies.

Overall differences arise from the assumed IMF and the stellar population synthesis models; the latest generation include more sophisticated treatment of the AGB contribution (e.g., Maraston et al. 2006; Bruzual 2007; Charlot & Bruzual 2007), although, for example, they do not fit very well to the observed SEDs of post-starburst galaxies (cf. Kriek et al. 2010). As of this writing, there remains large uncertainty in modeling the mid-IR light contribution from star-forming and post-starburst galaxies, rendering equally large uncertainties in the IRAC M/L relations. Consequently—although there is close binding between the near- and mid-IR luminosities—the M/L relation that accounts for the galaxy color (Equation (9)) should have the best correspondence with the 2 μm estimates, and we thus adopt them as the stellar mass for our sample.

8. STAR FORMATION HISTORY

In this section, we construct the scaling relation between the star formation and the stellar mass of the galaxy sample. Accordingly, using this mass (Equation (9) and the $W1$ luminosity) in conjunction with the $\mathrm{SFR_{IR}}$ (22 μm; Equation (2)) and the combined IR+UV SFR, we derive the global sSFR, gauging the present-to-past star formation history. Figure 19 presents the sSFR compared to the Hubble type and to the stellar mass content. The sSFR derived using the total SFR compared to the IR SFR is slightly higher (∼0.3 dex), yet both exhibit a similar trend with morphology, gas mass, and stellar content.

Reminiscent of the segregation observed in the *WISE* color-color plot (Figure 4), there are three distinct groupings: early-type ellipticals have very low sSFRs, early-type spirals have moderate sSFR, and late-type spirals have high sSFRs. Elliptical galaxies have exhausted their fuel supply: little if any star formation is happening and thus there is no growth in the total stellar mass. At the other extreme, late-type spirals (e.g., M 83) are actively forming stars from molecular hydrogen (with the neutral hydrogen tracking the gas content), building their stellar backbone and bulge populations (the cycle is graphically depicted in Figure 14). On smaller scales, indeed this is observed in Figure 20, a revisit of the southwest bar transition of M 83 (see Figure 13 for details), but now converting the $W3$ image to SFR and the $W1$ image to stellar mass to derive the sSFR at parsec-physical scales. Overlaid (in yellow/orange) are the 12CO contours, tracking the molecular gas. Both the gas and the highest sSFR regions are coincident, with values that peak at $\log \mathrm{SFR}/M_* = -9.75$, as shown in the red dashed histogram. As would be expected, the molecular gas is fueling the massive star formation, indirectly traced by $W3$ through PAH emission arising from PDRs. For the local universe, the existence of a tight scaling relation between the stellar mass (star formation history) and the SFR (current activity) is a vital clue that the formation of stars (and hence galaxy evolution) is regulated by secular (physical) processes that that are active over long (Gyr) periods of time. Moreover, this behavior where high-mass galaxies form fewer stars per unit stellar mass compared with less massive systems is typically found to exist for $z < 2$, with an overall decline in sSFR with decreasing redshift (e.g., Daddi et al. 2007; Noeske et al. 2007; Pannella et al. 2009; Karim et al. 2011). The shift of star formation efficiency from higher mass systems in the past to lower mass systems observed locally is often referred to as "cosmic downsizing" (Cowie et al. 1996).

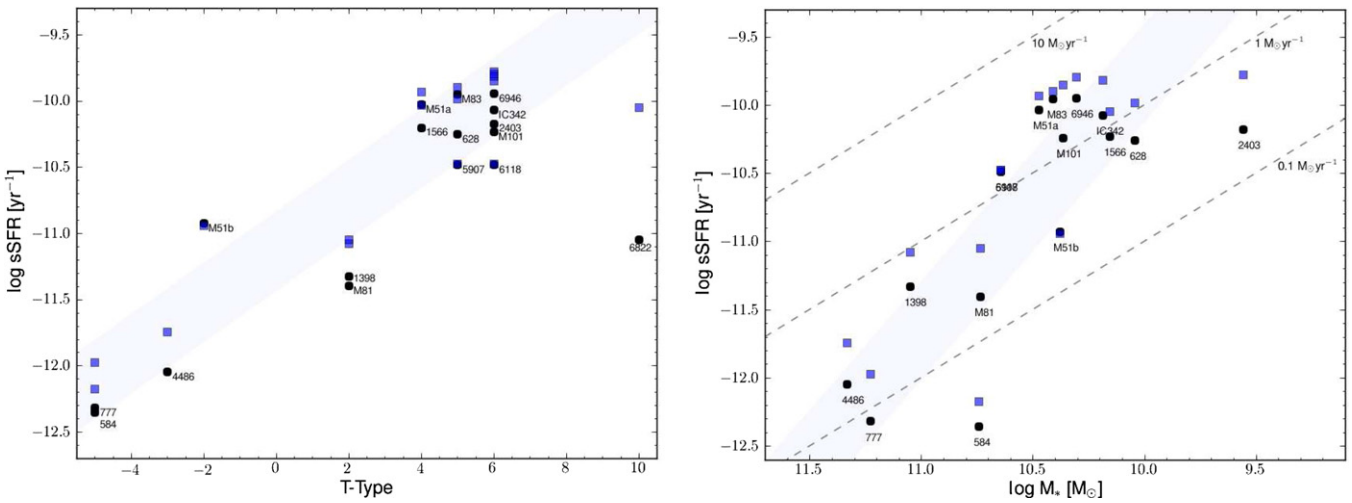

Figure 19. sSFR compared to the Hubble type and stellar mass. The stellar mass is derived using the M/L relation from this work (Equation (9)). Two global SFRs are shown: black points correspond to the SFR (22 μm; Equation (2)) and blue squares correspond to the combined IR+UV SFR. There is a similar linear trend (illustrated by the blue shaded regions) for both Hubble type and the host stellar mass. A range in SFRs (from 0.1 to 10 $M_\odot$ yr^{-1}) are represented by the dashed lines.

(A color version of this figure is available in the online journal.)

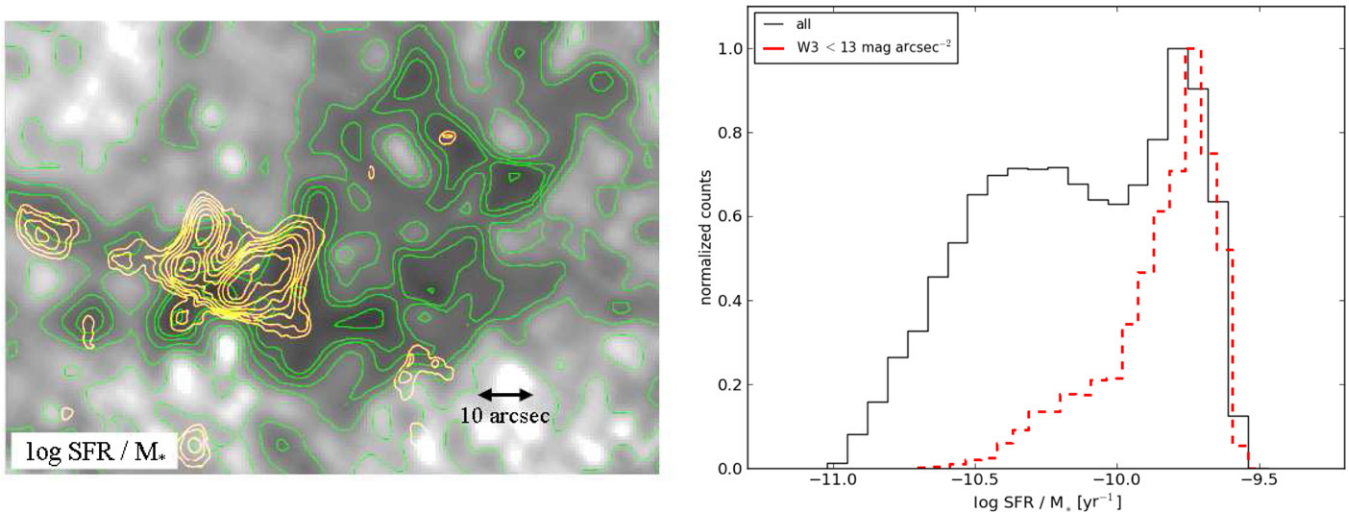

Figure 20. sSFR in the southwestern bar cusp of M 83. Left: the sSFR is derived from the $W1$ (stellar mass) and $W3$ (SFR) imaging. The green contours range from -10.5 to -9.75 for log SFR/M_* (yr^{-1}). The orange contours correspond to the molecular gas (see Figure 13); right: histogram showing the sSFR distribution for the region. The red dashed line denotes the 12 μm high surface brightness knots: <13 mag (0.2 mJy) arcsec^{-2}.

(A color version of this figure is available in the online journal.)

This observed difference in star formation efficiency between Hubble types, gas reservoir, and stellar content is consistent with the large sample results of Donoso et al. (2012), who compared the sSFR of star-forming, intermediate, and bulge-dominated AGN-type galaxies, as well as the GASS/COLDGASS analysis (Saintonge et al. 2011, 2012) that explored the relationship between the atomic and molecular gas components and the star formation histories using SDSS and *GALEX*. Finally, we note that the simple *WISE* color diagram (Figure 4(a)) has a similar behavior as the derived sSFR diagram because the colors, in fact, are tracing the same evolutionary states. That is, the $W1-W2$ versus $W2-W3$ colors in (Figure 4(a)) essentially capture the sSFR.

9. SUMMARY

In this paper we have presented the results of a mid-IR and UV photometric study of 17 large, nearby galaxies, using the *WISE*, *Spitzer*, and *GALEX* space telescopes. The primary science goals were to (1) characterize and assess the quality of source extraction for resolved galaxies observed by *WISE*, (2) to validate the WERGA measurements by comparison with those using *Spitzer* imaging, and (3) to derive the star formation activity and (4) the stellar mass content for the sample. For the galaxy M 83 (NGC 5236), we examined in detail the distribution of young and old stars, star formation activity, and gas content. We highlight here our main results from the M 83 analysis and from the larger sample.

1. Employing an MCM-HiRes deconvolution technique, we have reconstructed *WISE* images that have an improvement in angular resolution that is approximately a factor of three to four relative to the nominal (Atlas) *WISE* imaging, and comparable (to within 30%) in resolution to that of *Spitzer*/IRAC and *Spitzer*/MIPS-24. A more complete description and demonstration of MCM is given in Paper I.
2. The typical 1σ isophotal surface brightnesses for the *WISE* $W1$, $W2$, $W3$, and $W4$ bands, respectively, are 21.8, 18.1,

and 15.8 mag arcsec^2 (Vega). Azimuthal averaging achieves surface brightnesses that reach depths of 24.0, 23.0, 19.4, and 18.5 mag arcsec^2 for bands $W1$, $W2$, $W3$, and $W4$, respectively, equivalent to AB mag of 26.7, 26.3, 24.6, and 25.1 mag arcsec^{-2}, respectively.

3. The photometric performance using the MCM-HiRes reconstructed *WISE* imaging appears to be of high quality as gauged by detailed comparison with 2MASS, *Spitzer*, and *IRAS* photometric properties, augmented with SED analysis using population synthesis models. We caution that there remain cosmetic (negative depression) artifacts enveloping high surface brightness sources (e.g., bright stars; bright nuclei), particularly with $W4$ (22 μ); see Paper I for further discussion of these "ringing" artifacts.
4. For the barred spiral galaxy M 83, the direct comparison between *WISE* and *GALEX* of the two-dimensional distribution of the warmed ISM and the massive star population reveals the obscured (*WISE*) and unobscured (*GALEX*) sites for star formation. Intriguingly, the neutral H I gas correlates strongly with the 11.3 μm PAH emission, traced by the *WISE* 12 μm band, which is usually associated with the molecular gas that fuels star formation; the H I may be the byproduct of molecular hydrogen that has been dissociated by the strong radiation fields arising from the massive star formation in the spiral arms of M 83.
5. Employing the 2MASS and *WISE* band RSRs, and the SEDs of the Sun and Vega, we derive the absolute in-band magnitude of the Sun: 3.32, 3.24, 3.27, 3.23, and 3.25 mag for K_s, $W1$, $W2$, $W3$, and $W4$, respectively.
6. We have calibrated the IR global SFR relation that is appropriate to the *WISE* 12 and 22 μm bands using the *Spitzer* 24 μm relation as a bootstrap. In combination with the *GALEX* luminosities, computed SFRs that encompass both the obscured (traced by *WISE*) and unobscured (*GALEX*) present-day star formation activity. We find that the SFR relative to the neutral gas content follows a simple linear trend in which the larger the gas reservoir the higher the SFR, consistent with the K-S scaling relation.
7. The aggregate stellar mass is estimated using the 3.4 and 4.6 μm bands of *WISE*. We have derived several variations of the IRAC and *WISE* M/L relations, bootstrapped from the well-studied K_s-band relations and from population synthesis models that relate the mid-IR light that arises from the evolved stellar population to the total stellar content.
8. Combining the global SFR and the stellar content, we investigate the sSFR, gauging the present-to-past star formation history for the sample of galaxies. We find a clear scaling relation between the sSFR and the with Hubble type and the gas content: Early-type galaxies have exhausted their fuel supply, so there is either slow or no growth in the total stellar mass. Late-type spirals and galaxies with large gas reservoirs, are actively forming stars from molecular hydrogen and building their stellar disk and bulge populations.
9. We discuss the construction of WERGA that comprises a complete, volume-limited sample of the local universe. The strengths of *WISE* to trace the stellar mass and the star formation activity mean the WERGA will play a crucial and complementary role in the multi-wavelength effort to understand galaxy assembly and evolution.

We thank G. Meurer, S. Lord, J. Mazzarella, and B. Madore for tapping their vast knowledge base of nearby galaxies. Discussions with S. Meidt and N. Taylor were very helpful in understanding the (ongoing) difficulties with M/L modeling. This work is based (in part) on observations made with the *Spitzer* and research using the NASA/IPAC Extragalactic Database (NED) and IPAC Infrared Science Archive, all of which are operated by JPL, Caltech under a contract with the National Aeronautics and Space Administration. Support for this work was provided by NASA through an award issued by JPL/Caltech. R.J.A. was supported by an appointment to the NASA Postdoctoral Program at the Jet Propulsion Laboratory, administered by Oak Ridge Associated Universities through a contract with NASA. M.E.C. acknowledges support from the Australian Research Council (FS110200023). This publication makes use of data products from the Wide-field Infrared Survey Explorer, which is a joint project of the University of California, Los Angeles, and the Jet Propulsion Laboratory/California Institute of Technology, funded by the National Aeronautics and Space Administration.

APPENDIX A

SPITZER AND *IRAS* PHOTOMETRY

This appendix presents both the ancillary photometry measurements and the direct comparisons with those of *WISE*. Extending the analysis presented in Paper I, the objective is to validate the spatially de-convolved *WISE* imaging global and surface brightness measurements using ancillary infrared observations.

A.1. Spitzer Source Characterization

In order to directly compare the *WISE* isophotal aperture photometry with that of *Spitzer*, the same aperture size and shape used for the *WISE* measurements (Table 2) are applied to the IRAC and MIPS-24 measurements. The resulting photometry is presented in Table 7. These tabular results do not include any Galactic or internal extinction corrections.

Measurements are carried out for those galaxies with post-BCD mosaics available from either the SINGS archive or the *Spitzer* Heritage Archive. In a few cases the resulting mosaic images are too small to extract the integrated flux (using the *WISE* fiducial aperture) or to measure a reliable local background. NGC 1398 and NGC 6118 were only observed during the *Spitzer* Warm Mission, and thus only the IRAC-1 and IRAC-2 data were available. In the case of NGC 4486 (M 87), only the MIPS-24 mosaics were adequate in size to extract a complete flux. For the case of IC 342, the IRAC imaging does adequately cover the field, however the nucleus of IC 342 is so bright that it saturated the 12 s exposures. Consequently, we used the short-exposure (HDR) images to measure the IRAC-1 and IRAC-2 mosaics. For IRAC-3 and IRAC-4, since they were too faint to measure with the short HDR imaging, we used saturation recovery methods (developed by the Spitzer Science Center) to rectify the saturated nucleus of IC 342, which is so bright at these wavelengths that the light is dominated by the unresolved nucleus.

Most of the galaxies in the sample have integrated fluxes that have been previously published, notably from Dale et al. (2007) for the SINGS sample and Gordon et al. (2008) for M 101. Even though there has been no attempt to match apertures with the Dale et al. (2007) measurements, there is relatively good agreement between their flux densities and those of the isophotal photometry. We find that for most sources, the agreement is better than 10%, with a few notable exceptions: NGC 584, NGC 6822, and M 51b. The early-type galaxy NGC 584 is much brighter in the IRAC-4 and MIPS-24 measurements of

Table 7
Spitzer Fixed-aperture[a] Photometry

Name	IRAC-1 (Jy)	IRAC-2 (Jy)	IRAC-3 (Jy)	IRAC-4 (Jy)	MIPS-24 (Jy)
NGC 584	0.347 ± 0.007	0.216 ± 0.004	0.142 ± 0.004	0.070 ± 0.002	0.019 ± 0.001
NGC 628	0.822 ± 0.017	0.589 ± 0.012	1.025 ± 0.028	3.344 ± 0.083	2.882 ± 0.051
NGC 777	0.167 ± 0.004	0.112 ± 0.003	0.095 ± 0.008	0.037 ± 0.005	0.008 ± 0.004
NGC 1398	0.794 ± 0.016	0.514 ± 0.010	...	...	...
NGC 1566	0.705 ± 0.014	0.485 ± 0.010	0.861 ± 0.022	2.047 ± 0.051	2.851 ± 0.050
NGC 2403	1.610 ± 0.033	1.083 ± 0.021	1.854 ± 0.049	3.996 ± 0.099	5.536 ± 0.098
NGC 3031	10.535 ± 0.213	6.644 ± 0.130	6.111 ± 0.164	6.216 ± 0.162	5.296 ± 0.094
NGC 4486	...	...	...	...	0.185 ± 0.004
NGC 5194[b]	2.611 ± 0.053	1.748 ± 0.034	4.082 ± 0.105	10.912 ± 0.271	12.757 ± 0.226
NGC 5195[b]	1.120 ± 0.023	0.712 ± 0.014	0.667 ± 0.017	0.970 ± 0.024	1.434 ± 0.025
NGC 5236	6.083 ± 0.123	4.048 ± 0.079	6.350 ± 0.168	22.986 ± 0.572	42.155 ± 0.745
NGC 5457[c]	2.455 ± 0.050	1.639 ± 0.032	2.891 ± 0.081	7.508 ± 0.187	8.340 ± 0.147
NGC 5907	0.760 ± 0.015	0.519 ± 0.010	0.834 ± 0.021	1.882 ± 0.046	1.713 ± 0.030
NGC 6118	0.165 ± 0.003	0.114 ± 0.002	...	...	...
NGC 6822	1.832 ± 0.037	1.255 ± 0.025	0.985 ± 0.027	1.179 ± 0.032	1.448 ± 0.026
NGC 6946	3.157 ± 0.064	2.187 ± 0.043	5.096 ± 0.134	13.221 ± 0.329	20.177 ± 0.357
IC 342[d]	7.680 ± 0.155	5.168 ± 0.101	7.806 ± 0.218	22.219 ± 0.553	39.486 ± 0.698

Notes.
[a] Aperture size, axis ratio, and orientation are matched to *WISE*; see Table 2 for coordinate position and aperture details.
[b] Photometry of NGC 5194/5 is uncertain due to blending.
[c] For comparison, Gordon et al. (2008) measured the following *uncorrected* IRAC fluxes for M 101: 2.84, 1.76, 3.69 and 7.26 Jy, IRAC-1, 2, 3, and 4, respectively. The MIPS-24 flux is 10.5 Jy. Both the IRAC and MIPS-24 measurements are within 5% of the *uncorrected* measurements of this work.
[d] IRAC imaging of IC342 saturated in the core, recovered using short-exposure HDR images. Measurements are not corrected for Galactic or internal extinction.

the SINGS extraction, likely due to using an aperture that is too large for relatively weak R-J emission in these bands (see Section 4.2 for discussion). Similarly, a smaller aperture (compared with SINGS) was used to extract the *W*4 and MIPS-24 photometry for NGC 6822, resulting in a much smaller flux by comparison. NGC 6822 is the most difficult galaxy to characterize due to its low surface brightness, flat-profile morphology, and proximity to the Galactic Plane with its associated foreground star and dust emission contamination. Another outlier in the comparison, NGC 5195 (M 51b) is much fainter in the SINGS extraction, likely due to the complexity and uncertainty with deblending M 51b from the larger M 51a. As a final comparison, we note that for the giant spiral galaxy, M 101, there is excellent agreement with photometry (where the aperture measurements are uncorrected) reported by Gordon et al. (2008); see Table 7 notes for details.

A.2. Comparing WISE with Spitzer and IRAS

Averaging over large scales, a comparison between the *WISE* and *Spitzer* imaging is provided by the mean radial profiles for each galaxy in each band, plots are included in Appendix C. The IRAC/MIPS-24 profile (magenta line) typically matches closely with the *WISE* profile (black line), with offset differences due to the bandpass differences. For a more quantitative global analysis, we turn to the integrated fluxes.

Directly comparing the *WISE* isophotal photometry with the aperture-matched photometry of IRAC and MIPS-24 requires taking into account the bandpass differences between the two infrared missions. Computing synthetic photometry of model galaxy SED templates (GRASIL: Polletta et al. 2006, 2007; Silva et al. 1998) from the *WISE* and *Spitzer* bandpass RSRs (Jarrett et al. 2011), we are able to predict the integrated flux ratio between *WISE* and *Spitzer* photometry for a range of Hubble types. Figure 21 presents *WISE* versus *Spitzer* photometry flux ratios, which are compared to predicted ratios from early-type, late-type, and starburst galaxies. As noted in Section 3, color corrections for both *WISE* and *Spitzer* sources have been applied.

Comparing *W*1 3.4 μm with that of IRAC-1 3.6 μm, *W*1 will tend to be brighter than IRAC-1 since the *WISE* band is relatively bluer; i.e., it is more sensitive to R-J light from the evolved population that is peaking in the near-IR window. And indeed, that is what is observed, particularly for the early-type galaxies (NGC 584, NGC 777, M 87, NGC 1398, and M 51b), which tend to be 5%–10% brighter in *W*1 (the expected value is ∼6%). The late-type galaxies range between 0% and 5% brighter in *W*1, which is in line with the expectation. The notable outliers are the S4G galaxies NGC 6118 and NGC 1398, which are 10%–15% too bright in *W*1 compared with the expectation; and M 51a, which is too faint by 5%–10%, likely due to it complex blending with M 51b. IC342, interestingly, has a ratio that is consistent with a starburst SED in which warm dust has inverted the ratio; indeed, the nucleus of IC342 is undergoing a strong starburst (cf. Laine et al. 2006; Brandl et al. 2006; J. Turner 2011, private communication).

Comparing *W*2 4.6 μm with that of IRAC-2 4.5 μm, the *WISE* fluxes are expected to be slightly fainter, ∼5%, than the IRAC fluxes because of the slope in the R-J tail. The observed scatter in the flux ratio is on that order, with early and late types mixing without any obvious segregation. The outliers are M 51a/b, a blended pair system, and NGC 6822, which is a Magellanic dwarf located behind the Milky Way.

The *W*3 12 μm bandpass is significantly different from the IRAC-4 8.0 μm both in terms of the central wavelength and the sensitivity to the ISM. The IRAC-4 band is centered on the 7.7 μm PAH band (and includes the 6.2 μm PAH band),

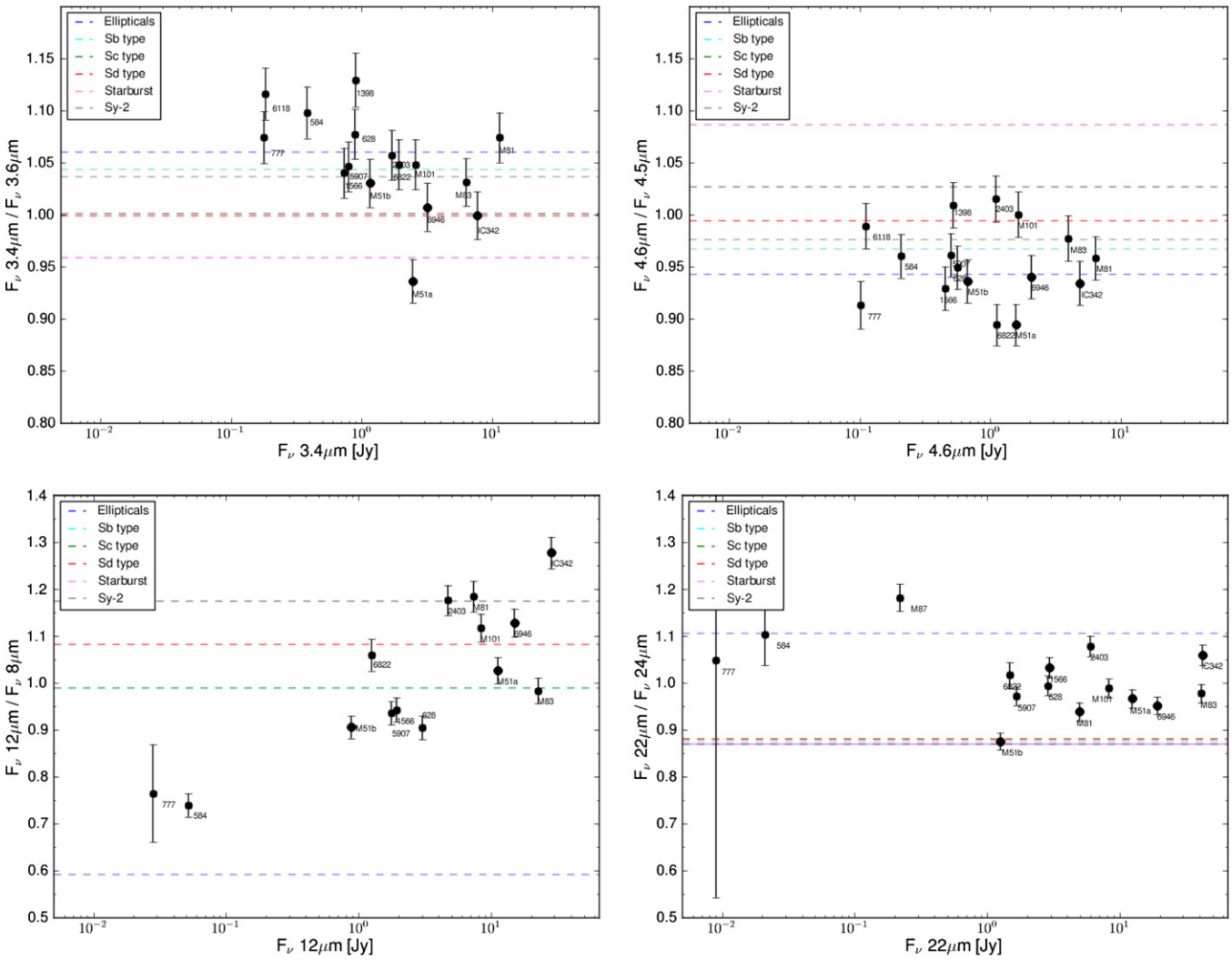

Figure 21. *WISE* photometry compared to *Spitzer* IRAC and MIPS-24. The isophotal apertures have been matched between *WISE* and *Spitzer* in most cases (filled circles); the open-circle symbols denotes those *Spitzer* measurements in which the mosaic was too small to capture the total flux, or when the source photometry may be compromised (blending or source confusion). The galaxy name is indicated next to the measurement, where single numbers represent the NGC #. The horizontal lines represent the expect flux ratios for specified Hubble types (see legend), derived from model templates integrated over the *WISE* and *Spitzer* RSRs.

(A color version of this figure is available in the online journal.)

which is small and tends toward charged molecules, while the *W*3 band is centered on the 11.3 PAH band, which is larger and tends toward neutral-charge molecules (cf. Tielens 2008; Draine 2011). The broad *W*3 band also includes the silicate absorption band at 10 μm, a typically significant feature in IR-luminous galaxies. The expected flux ratios are, consequently, expected to be large depending on the galaxy type, ranging from 0.6 for early types (R-J emission) and 1.2 for star-forming disk galaxies with AGN. Although the range is large, the observed ratios appear to be within 5%–10% of the expected values. The highest ratio belongs to IC342, which is likely the strongest nuclear starburst in the sample. The other strongly star-forming galaxies, including NGC 2403, NGC 6946, and M 83, all have high ratios, indicating strong 11.3 μm PAH emission.

For the longest wavelength extractions, we compare *W*4 22 μm with the MIPS-24 measurements. The expected flux ratios range from 0.9 (late types) to 1.1 (early types). The observed ratios tend to cluster around unity, suggesting an uncertainty of ∼5%–10% between *WISE* and *Spitzer* measurements in these two bands. The only outlier is M 87, revealing a difference in nuclear AGN emission observed by *WISE* and *Spitzer*. Finally, a note about the MIPS-24 observations of M 81, NGC 1566, and M 51b: they all have *Spitzer* imaging that does not fully cover the field as wide as *WISE*; hence, there is a slight (∼5%) underestimate of their *Spitzer* fluxes.

We now compare the *WISE* isophotal photometry with published *IRAS* 12 and 25 μm fluxes. As with the *Spitzer* comparison, we derive the expected ratios using model SED templates and the *WISE*/*IRAS* bandpass RSRs. No color corrections have been applied to the *IRAS* fluxes, only the published values are used for this comparison. The results are presented in Figure 22. Due to the limited sensitivity of *IRAS*, all of the galaxies in this comparison are gas-rich star-forming systems, roughly Sc/d types (M 81 is the exception, it is an early-type spiral).

For 12 μm, we expect ratios between 1.0 (early-type spirals) and 1.35 (starbursts). The observed ratios are 1.1 to 1.4 for most of the systems, which is ∼10% brighter than the expected range for Sc/Sd type galaxies. M 83 appears to have a flux ratio that is 10% too faint, but well within the uncertainties (*IRAS*

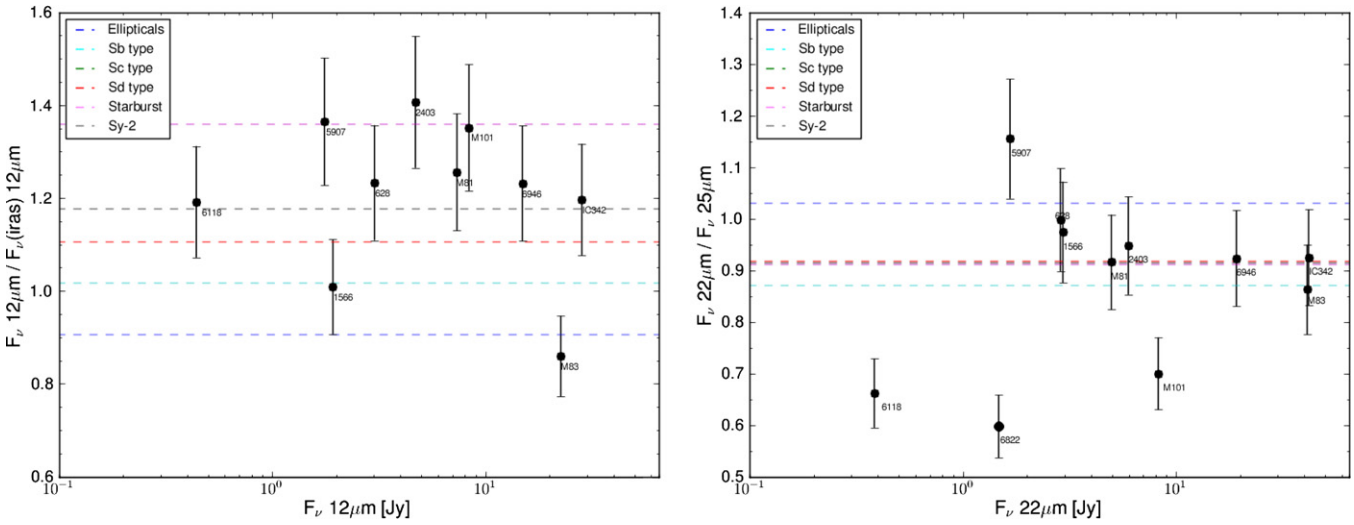

Figure 22. *WISE* photometry compared to the *IRAS* 12 and 25 μm bands. The *IRAS* photometry comes from Rice et al. (1988), Sanders et al. (2003), and Lisenfeld et al. (2007). Sources NGC 6822 and NGC 1398 are not shown due to confusion or poor-quality *IRAS* measurements.

(A color version of this figure is available in the online journal.)

fluxes). We would then conclude that *WISE* $W3$ photometry is systematically ∼10% brighter than *IRAS* estimates.

For 25 μm, we expect a more narrow range in flux ratio, from 0.9 (late types) to 1.1 (early types). What is observed is that most sources do have ratios in that range, but exceptions include NGC 5907 (ratio is too high), NGC 6118 (too low), and M 101 (too low). It is not clear whether this is a *WISE* or *IRAS* discrepancy, but the latter is the more likely given that *WISE* $W4$ and MIPS-24 have very good agreement. The uncertainty between *WISE* $W4$ and *IRAS* 25 μm extractions is ∼20%, consistent with the quoted *IRAS* flux density uncertainties.

APPENDIX B

GALEX PHOTOMETRY

Aperture photometry extracted from the *GALEX* images of the sample galaxies (except NGC 6118, which was not observed by *GALEX*) is presented in Table 8. Since there is little (or weak) spatial correspondence between the UV and the IR properties (discussed in Section 5, M 83 results), there is no attempt to match the UV apertures with those of *WISE*; instead, we use the optical RC3 elliptical shape values, with slight adjustments where needed. The reported flux densities have not been corrected for the foreground Galactic extinction, however the table also includes the expected foreground extinction (AB mag units) in the *GALEX* bands (see Treyer et al. 2007). In Section 6, we estimated the UV SFR using these flux densities corrected for Galactic extinction.

Table 8
GALEX Aperture Photometry

Name	Axis Ratio	P.A. (°)	R_{25} (′)	F_{FUV} (mJy)	A_{FUV} (mag)	F_{NUV} (mJy)	A_{NUV} (mag)
NGC 584	0.66	69.5	2.9	0.4	0.35	1.6	0.35
NGC 628	0.93	80.0	10.3	75.2	0.59	104.7	0.58
NGC 777	0.74	145.0	2.1	0.3	0.38	0.6	0.38
NGC 1398	0.71	100.0	5.2	9.4	0.11	14.6	0.11
NGC 1566	0.91	59.0	6.5	51.5	0.08	66.1	0.08
NGC 2403	0.61	126.0	14.9	251.2	0.33	322.1	0.33
NGC 3031	0.70	157.0	21.1	177.0	0.66	248.9	0.66
NGC 4486	0.94	0.0	7.9	6.5	0.19	13.8	0.19
NGC 5194	0.65	184.0	8.2	131.8	0.29	214.8	0.29
NGC 5195	0.79	79.0	9.3	4.5	0.29	10.0	0.29
NGC 5236	1.00	0.0	14.0	325.1	0.55	544.5	0.55
NGC 5457	0.95	80.0	17.2	334.2	0.07	416.9	0.07
NGC 5907	0.16	156.0	7.2	8.1	0.09	12.5	0.09
NGC 6822	1.00	0.0	15.1	359.8	1.94	539.5	1.90
NGC 6946	0.96	80.0	9.4	288.4	2.82	461.3	2.74
IC 342	0.96	81.0	15.0	1037.6	4.60	1116.9	4.39

Notes. The reported flux densities have not been corrected for the foreground Galactic extinction; however, A_{FUV} and A_{NUV} are the estimated extinctions (in AB mag units) for the *GALEX* bands and may be used to correct the flux densities accordingly. The formal errors are less than 1%; but including the flat-field and calibration errors, the actual photometric uncertainty is ∼5%. The semi-major axis, R_{25}, is approximately equal to one-half of the optical (RC3) D25 diameter. Photometry of NGC 5194/5 is uncertain due to blending.

APPENDIX C

RADIAL SURFACE BRIGHTNESS PROFILES

Figure 23 shows the azimuthally averaged, radial surface brightness profiles for sample of galaxies, including both *WISE* HiRes (black solid line) and *Spitzer* (magenta solid line) measurements. The results paired in the standard way: $W1$/IRAC-1, $W2$/IRAC-2, $W3$/IRAC-4, and $W4$/MIPS-24, from left to right panels, respectively. The *WISE* profile shapes are simply characterized using a double Sérsic function fit: the inner galaxy or bulge light (cyan dashed line) and the disk (blue dashed line); the gray dashed line is the total contribution from the bulge and disk.

For the elliptical and early-type galaxies (NGC 584, NGC 777, and M 87), the *WISE* and *Spitzer* results are solidly consistent for all radii down to the background level, but for the longer wavelengths the signal is much fainter and the surface brightness drops rapidly with radius. The star-forming galaxies also show good correspondence between *WISE* and *Spitzer* profiles. Note that for the $W3$ to IRAC-4 comparison, the bandpasses are sufficiently different such that there is an offset in surface brightness. The expected offset, based on the spectral shape, ranges from a scale factor of 0.6 (early types) to 1.1 (star-forming) to 1.2 (AGN); see Figure 7 for details. One clear

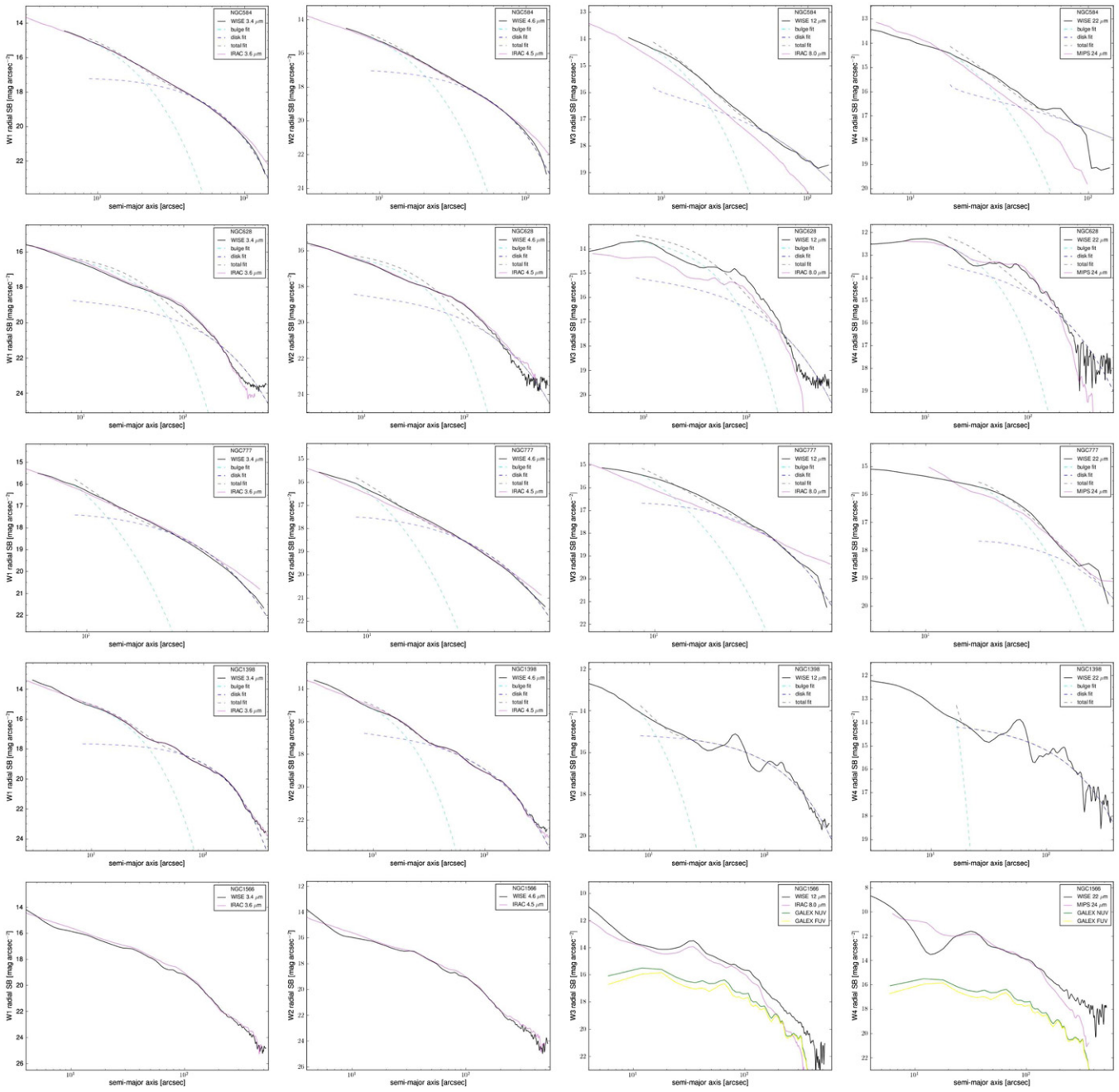

Figure 23. Azimuthally averaged elliptical–radial profiles comparing *WISE* (black line) with IRAC and MIPS-24 (magenta line). The dashed lines show the Sérsic fits to the bulge (cyan) and disk (blue) regions.

(A color version of this figure is available in the online journal.)

trend that is seen is that the *Spitzer* images (notably IRAC) are sometimes too small to capture the total flux of the galaxy, and as a consequence the local background subtraction tends to chop off the outer most extended light. For example, the *W*3 profile of M 83 (see also Figure 13) drops to zero at a radius of 250″, whereas the *WISE W*3 (as well as *GALEX*) extends beyond 500″.

Finally, the low surface brightness galaxy in the sample, NGC 6822, shows the largest departure differences between *WISE* HiRes and the *Spitzer* imaging profiles. In all four bands, the *WISE* profiles show a saw-tooth ringing pattern, which is not seen in *Spitzer* profiles. This galaxy is characterized by a flat diffuse component punctuated with stars and (a few) star formation regions (see Figure 1). The averaged *WISE* profiles of NGC 6822 are in fact dominated by noise fluctuations and the "ringing" artifacts that are induced by the MCM process (see Paper I for more details on the amplified noise and ringing behavior). However, without the radial averaging, the differences are not so apparent when comparing images side-by-side; see Figure 24, which shows the *W*3 12 μm (drizzle and HiRes versions) and IRAC 8 μm images of NGC 6822. This case serves as a cautionary note: For dwarf and low surface brightness galaxies, the drizzle co-addition method is the preferred enhanced resolution process for *WISE* imaging.

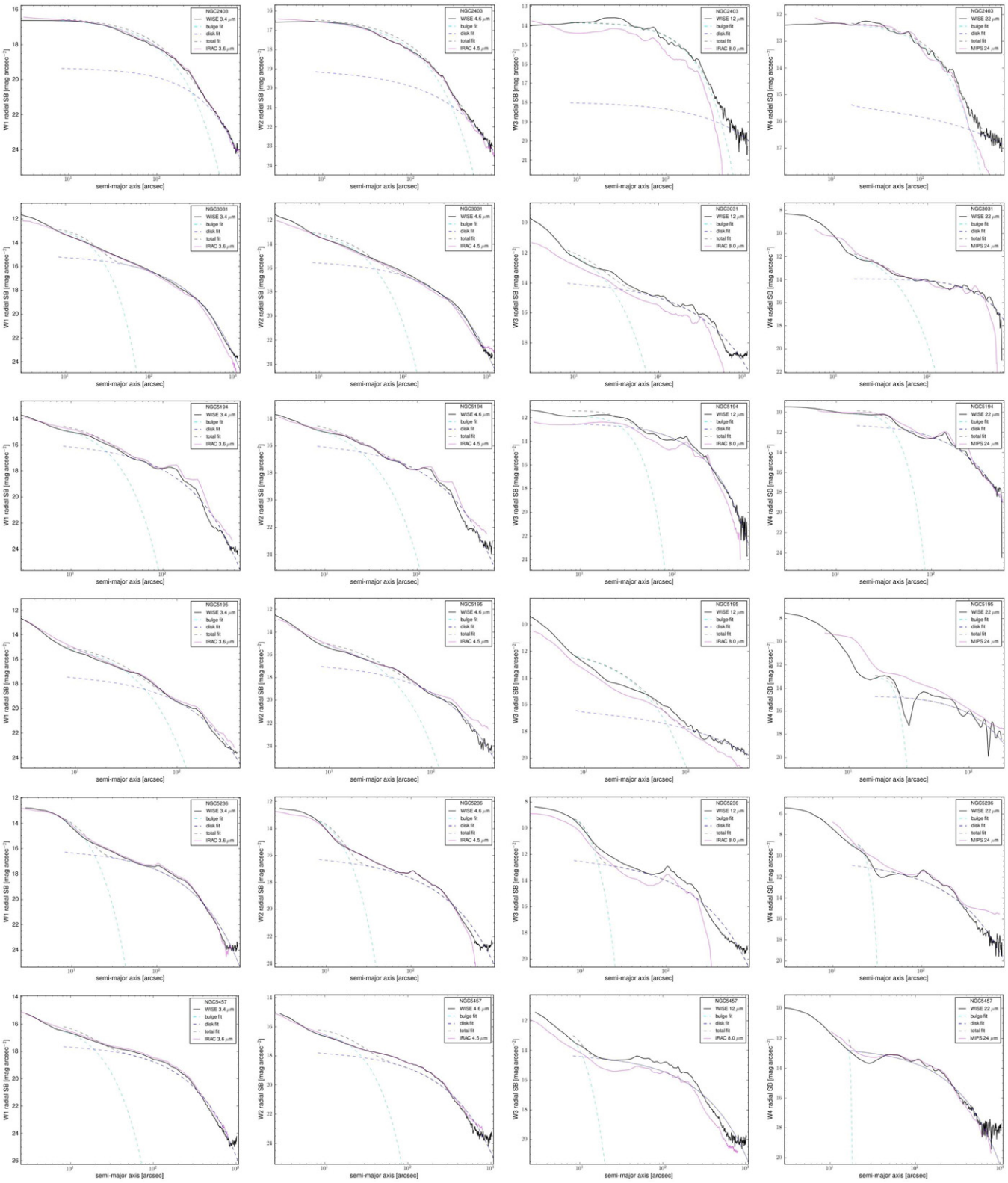

Figure 23. (Continued)

APPENDIX D

WISE ENHANCED RESOLUTION GALAXY ATLAS

The results presented in this work represent the pilot study of a large program in which we will use the *WISE* image and source catalog archive to build the WERGA, consisting of the largest galaxies in the sky, that will complete the S4G IRAC-1 and IRAC-2, $D = 40$ Mpc volume-limited, survey, as well as complement other large surveys (e.g., SDSS, 2MASS, *AKARI*, LVIS).

A key feature of the WERGA is the construction of images with a factor of ∼3–4 improvement in spatial resolution

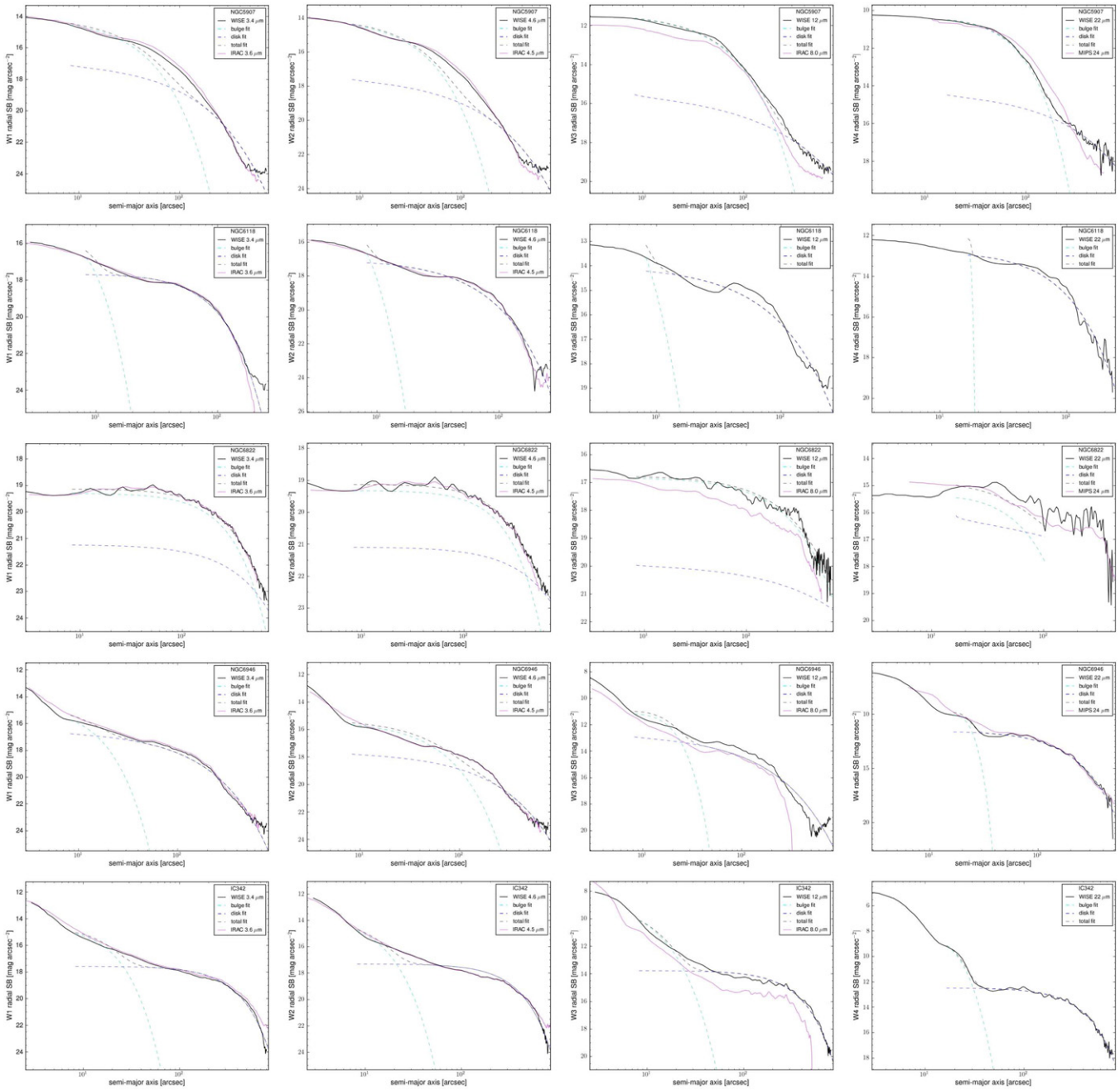

Figure 23. (Continued)

compared to the public-release mosaic imaging. The achieved resolutions are comparable, ∼25%–30%, to those of *Spitzer* IRAC and MIPS-24. We estimate that MCM/HiRes resolution enhancement (Paper I) is most effective for all galaxies with a near-IR diameter greater than ∼2′. Using the 2MASS XSC (Jarrett et al. 2000, 2003) to select sources by their near-IR angular size, we find over ∼10,000 galaxies with diameters greater than this limit. For galaxies smaller than this size threshold, the most effective and practical resolution-enhancement method is to employ Variable-Pixel Linear Reconstruction ("drizzling"), which improves spatial resolution performance compared with nominal *WISE* imaging by ∼30%–40%, but is also much less CPU-intensive than the MCM/HiRes reconstruction.

Both sets of images, four bands each, will comprise the WERGA imaging that will be released to the public via NED as part of this project. This all-sky image Atlas will have broad and enduring impact to the community, representing the only *WISE* imaging that is dedicated to resolved sources, and with the HiRes reconstructions a unique and fundamental component that transforms the all-sky survey into a powerful "observatory" not unlike that of the *Spitzer Space Telescope*. The legacy value of these high-resolution images will span decades given that *AKARI* and *WISE* are likely to be the only mid-IR all-sky survey for many years to come; indeed, most galaxies in the local universe have only been imaged and measured by *WISE* (e.g., compared to the *Spitzer* coverage of the local universe).

The advantage of *WISE* of simultaneously tracing the stellar mass and the star formation activity means the WERGA will play a crucial and complementary role in the multi-wavelength

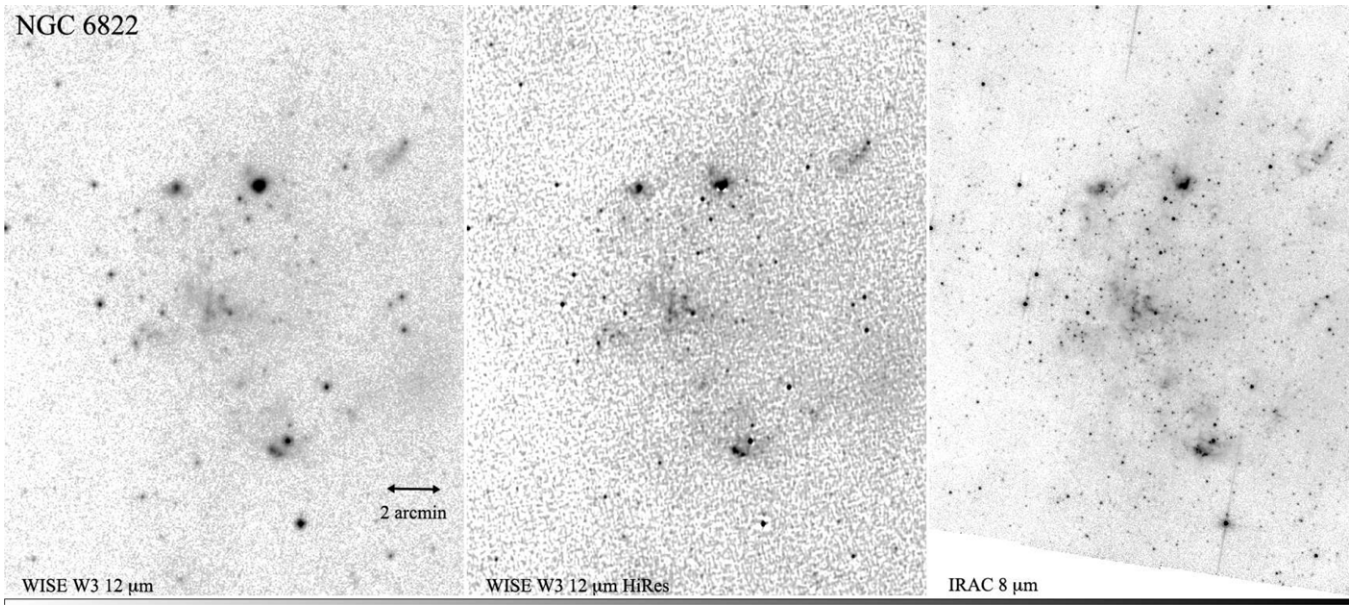

Figure 24. Dwarf galaxy NGC 6822. *WISE W*3 12 μm drizzle and HiRes, and *Spitzer* IRAC 8 μm imaging.

endeavor to understand galaxy assembly and evolution. This dual capability means that the WERGA could provide a resolved anchor for the (typically, spatially coarse) atomic and molecular gas studies of the SFR to stellar mass scaling relations that are now underway (e.g., GASS/COLDGASS). Moreover, in the coming decade we will see the entire sky mapped with unprecedented spectral sensitivity and spatial detail by radio-wave surveys (ASKAP, MeerKAT, and Apertif SKA pathfinders). Notably, the ASKAP-WALLABY (Koribalski & Staveley-Smith 2013, in preparation) and EMU (Norris et al. 2011) projects will extract neutral hydrogen content and radio continuum (e.g., synchrotron) emission from galaxies in the local universe, both of which in combination with *WISE* provide insight to the present and past star formation histories.

REFERENCES

Bell, E. F., & de Jong, R. S. 2001, ApJ, 550, 212
Bell, E. F., McIntosh, D. H., Katz, N., & Weinberg, M. D. 2003, ApJS, 149, 289
Berta, S., Fritz, J., Franceschini, A., Bressan, A., & Pernechele, C. 2003, A&A, 403, 119
Boomsma, R., Oosterloo, T. A., Fraternali, F., et al. 2008, A&A, 490, 555
Brandl, B. R., Bernard-Salas, J., Spoon, H. W. W., et al. 2006, ApJ, 653, 1129
Briggs, F. H. 1982, AJ, 259, 544
Bruzual, G. 2007, in ASP Conf. Ser. 374, From Stars to Galaxies: Building the Pieces to Build Up the Universe, ed. A. Vallenari et al. (San Francisco, CA: ASP), 303
Bruzual, G., & Charlot, S. 2003, MNRAS, 344, 1000
Buat, V., Boissier, S., Burgarella, D., et al. 2008, A&A, 483, 107
Buat, V., Giovannoli, E., Takeuchi, T. T., et al. 2011, A&A, 529, A22
Calzetti, D. 2011, EAS Publ. Ser., 46, 133
Calzetti, D., Kennicutt, R. C., Engelbracht, C. W., et al. 2007, ApJ, 666, 870
Cannon, J. M., Walter, F., Armus, L., et al. 2006, ApJ, 652, 1170
Cardelli, J. A., Clayton, G. C., & Mathis, J. S. 1989, ApJ, 345, 245
Chabrier, G. 2003, PASP, 115, 763
Chynoweth, K., Langston, G., Holley-Bockelmann, K., & Lockman, F. 2009, AJ, 138, 287
Clementini, G., Held, E. V., Baldacci, L., & Rizzi, L. 2003, ApJ, 588, 85
Cluver, M. E., Jarrett, T. H., Kraan-Korteweg, R. C., et al. 2010, ApJ, 725, 1550
Cowie, L. L., Songaila, A., Hu, E. M., & Cohen, J. G. 1996, AJ, 112, 839
Crosthwaite, L. P., Turner, J. L., & Ho, P. T. P. 2000, AJ, 119, 1720
Crosthwaite, L. P., Turner, J. L., & Ho, P. T. P. 2002, AJ, 123, 1892
Cutri, R., Wright, E. L., Conrow, T., et al. 2011, *WISE* Explanatory Supplement, http://wise2.ipac.caltech.edu/docs/release/prelim/expsup/
Daddi, E., Dickinson, M., Morrison, G., et al. 2007, ApJ, 670, 156
Dale, D. A., Gil de Paz, A., Gordon, K. D., et al. 2007, ApJ, 655, 863
de Blok, W. J. G., Walter, F., Brinks, E., et al. 2008, AJ, 136, 2648
de Vaucouleurs, G. 1994, in Quantifying Galaxy Morphology at High Redshift, STSCI workshop (Baltimore, MD: STScI), http://www.stsci.edu/institute/conference/galaxy-morphology/program2.html
de Vaucouleurs, G., de Vaucouleurs, A., Corwin, H. G., Jr., et al. 1991, Third Reference Catalogue of Bright Galaxies (RC3; New York: Springer)
Dong, H., Calzetti, D., Regan, M., et al. 2008, AJ, 136, 479
Donoso, E., et al. 2012, ApJ, 748, 80
Draine, B. T. 2011, EAS Publ. Ser., 46, 29
Driver, S. P., Hill, D. T., Kelvin, L. S., et al. 2011, MNRAS, 413, 971
Elbaz, D., Daddi, E., Le Borgne, D., et al. 2007, A&A, 468, 33
Engelbracht, C. W., Rieke, G. H., Gordon, K. D., et al. 2008, ApJ, 678, 804
Eskew, M., Zaritsky, D., & Meidt, S. 2012, AJ, 143, 139
Flaherty, K. M., Pipher, J. L., Megeath, S. T., et al. 2007, ApJ, 663, 1069
For, B. Q., Koribalski, B. S., & Jarrett, T. H. 2012, MNRAS, 425, 1934
Foyle, K., Wilson, C. D., Mentuch, E., et al. 2012, MNRAS, 421, 2917
Fukugita, M., Shimasaku, K., & Ichikawa, T. 1995, PASP, 107, 945
Gil de Paz, A., Boissier, S., Madore, B. F., et al. 2007, ApJS, 173, 185
Goddard, Q. E., Kennicutt, R. C., Ryan-Weber, E. V., et al. 2010, MNRAS, 405, 2791
Gordon, K. D., Engelbracht, C. W., Rieke, G. H., et al. 2008, ApJ, 682, 336
Goto, T., Arnouts, S., Inami, H., et al. 2011, MNRAS, 410, 573
Jarrett, T. H., Chester, T., Cutri, R., et al. 2000, AJ, 119, 2498
Helou, G., Roussel, H., Appleton, P., et al. 2004, ApJS, 154, 253
Herrmann, K. A., Ciardullo, R., Feldmeier, J. J., & Vinciguerra, M. 2008, ApJ, 683, 630
Huchtmeier, W. K., & Bohnensiengel, H. D. 1981, A&A, 100, 72
Hunter, D. A., Baum, W., O'Neil, E., & Lynds, R. 1996, ApJ, 468, 633
Indebetouw, R., Mathis, J. S., Babler, B. L., et al. 2005, ApJ, 619, 931
James, P. A., Knapen, J. H., Shane, N. S., Baldry, I., & de Jong, R. 2008, A&A, 482, 507
Jarrett, T. H., Chester, T., Cutri, R., Schneider, S., & Huchra, J. 2003, AJ, 125, 525
Jarrett, T. H., Cohen, M., Masci, F., et al. 2011, ApJ, 735, 112
Jarrett, T. J., et al. 2012, AJ, 144, 68 (Paper I)
Kanbur, S. M., Ngeow, C., Nikolaev, S., Tanvir, N. R., & Hendry, M. A. 2003, A&A, 411, 361
Kannappan, S. J., & Gawiser, E. 2007, ApJ, 657, L5
Karim, A., Schinnerer, E., Martínez-Sansigre, A., et al. 2011, ApJ, 730, 61
Kenney, J. D. P., & Lord, S. D. 1991, ApJ, 381, 118
Kennicutt, R. C., Jr. 1989, ApJ, 344, 68
Kennicutt, R. C., Jr. 1998, ARA&A, 36, 189
Kennicutt, R. C., Jr., Armus, L., Bendo, G., et al. 2003, PASP, 115, 928
Kennicutt, R. C., Jr., Hao, C.-N., Calzetti, D., et al. 2009, ApJ, 703, 1672
Kilborn, V., Koribalski, B., Forbes, D., Barnes, D., & Musgrave, R. 2005, MNRAS, 356, 77
Kohno, T. B. D., Tosaki, T., Matsushita, et al. 2002, PASJ, 54, 541
Koribalski, B. S. 2010, ASPC, 421, 137

Koribalski, B. S., Staveley-Smith, L., Kilborn, V. A., et al. 2004, AJ, 128, 16
Kriek, M., Labbé, I., Conroy, C., et al. 2010, ApJ, 722, 64
Laine, S., Kotilainen, J. K., Reunanen, J., Ryder, S. D., & Beck, R. 2006, AJ, 131, 701
Larsen, S. S., Brodie, J. P., Elmegreen, B. G., et al. 2001, ApJ, 556, 801
Leroy, A. K., Walter, F., Brinks, E., et al. 2008, AJ, 136, 2782
Li, H.-N., Wu, H., Cao, C., & Zhu, Y.-N. 2007, AJ, 134, 1315
Lisenfeld, U., Verdes-Montenegro, L., Sulentic, J., et al. 2007, A&A, 462, 507
Lord, S. D., & Kenney, J. D. P. 1991, ApJ, 381, 130
Lundgren, A. A., Olofsson, H., Wiklind, T., & Beck, R. 2008, in Proc. ASP Conf. Ser. 390, Pathways through an Eclectic Universe, ed. J. H. Knapen, T. J. Mahoney, & A. Vazdekis (San Francisco, CA: ASP), 144
Lundgren, A. A., Wiklind, T., Olofsson, H., & Rydbeck, G. 2004, A&A, 413, 505
Malin, D., & Hadley, B. 1997, PASA, 14, 52
Maraston, C., Daddi, E., Renzini, A., et al. 2006, ApJ, 652, 85
Martin, D. C., Fanson, J., Schiminovich, D., et al. 2005, ApJ, 619, L1
Masci, F. J., & Fowler, J. W. 2009, in ASP Conf. Ser. 411, Astronomical Data Analysis Software and Systems XVIII, ed. D. Bohlender, P. Dowler, & D. Durand (San Francisco, CA: ASP), 67
Masters, K., Giovanelli, R., & Haynes, M. 2003, ApJ, 126, 158
Meidt, S. E., Schinnerer, E., Munoz-Mateos, J.-C., et al. 2012, ApJ, 748, L30
Meurer, G. R., Hanish, D. J., Ferguson, H. C., et al. 2006, ApJS, 165, 307
Morrissey, P., Conrow, T., Barlow, T. A., et al. 2007, ApJS, 173, 682
Morrissey, P., Schiminovich, D., Barlow, T. A., et al. 2005, ApJ, 619, L7
Murakami, H., Baba, H., Barthel, P., et al. 2007, PASJ, 59, S369
Noeske, K. G., Weiner, B. J., Faber, S. M., et al. 2007, ApJ, 660, L43
Norris, R., et al. 2011, PASA, 28, 215
Oh, S.-H., de Blok, W. J. G., Walter, F., Brinks, E., & Kennicutt, R. C., Jr. 2008, AJ, 136, 2761
Pahre, M. A., Ashby, M. L. N., Fazio, G. G., & Willner, S. P. 2004, ApJS, 154, 229
Pannella, M., Gabasch, A., Goranova, Y., et al. 2009, ApJ, 701, 787
Paturel, G., Theureau, G., Fouqué, P., et al. 2002, A&A, 383, 398
Petty, S., Assef, R., Jarrett, T. H., et al. 2012, AJ, submitted
Pohlen, M., Martinez-Delgado, D., Majewski, S., et al. 2004, in ASP Conf. Ser. 327, Satellites and Tidal Streams, ed. F. Prada, D. Martinez Delgado, & T. J. Mahoney (San Francisco, CA: ASP), 288
Polletta, M., Tajer, M., Maraschi, L., et al. 2007, ApJ, 663, 81
Polletta, M., Wilkes, B. J., Siana, B., et al. 2006, ApJ, 642, 673
Poznanski, D., Butler, N., Fillipenko, A. V., et al. 2009, ApJ, 694, 1067
Rand, R. J., Lord, S. D., & Higdon, J. L. 1999, ApJ, 513, 720
Reach, W. T., Megeath, S. T., Cohen, M., et al. 2005, PASP, 117, 978
Relaño, M., Lisenfeld, U., Pérez-González, P., Vílchez, J., & Battaner, E. 2007, ApJ, 667, L141
Rice, W., Lonsdale, C. J., Soifer, B. T., et al. 1988, ApJS, 68, 91
Rieke, G. H., Alonso-Herrero, A., Weiner, B. J., et al. 2009, ApJ, 692, 556
Rogstad, D., & Shostak, G. 1971, A&A, 13, 99
Rujopakarn, W., Rieke, G., Weiner, B., et al. 2012, ApJ, 755, 168
Saha, A., Claver, J., & Hoessel, J. 2002, AJ, 124, 839
Saintonge, A., Kauffmann, G., Wang, J., et al. 2011, MNRAS, 415, 61
Saintonge, A., Tacconi, L., Fabello, S., et al. 2012, ApJ, 758, 73
Sancisi, R., & van Albada, T. S. 1987, in Dark Matter in the Universe, ed. J. Kormendy & G. R. Knapp (Kluwer: Dordrecht), 67
Sanders, D. B., Mazzarella, J. M., Kim, D. C., et al. 2003, AJ, 126, 1607
Schiminovich, D., Wyder, T. K., Martin, D. C., et al. 2007, ApJS, 173, 315
Schlegel, D. J., Finkbeiner, D. P., & Davis, M. 1998, ApJ, 500, 525
Shang, Z., Zheng, Z., & Brinks, E. 1998, ApJ, 504, L23
Sheth, K., Regan, M., Hinz, J. L., et al. 2010, PASP, 122, 1397
Shetty, R., & Ostriker, E. 2006, ApJ, 647, 997
Shi, Y., Helou, G., Yan, L., et al. 2011, ApJ, 733, 87
Shi, Y., Rieke, G., Hines, D., Gordon, K., & Egami, E. 2007, ApJ, 655, 781
Silva, L., Granato, G. L., Bressan, A., & Danese, L. 1998, ApJ, 509, 103
Stern, D., Assef, R. J., Benford, D. J., et al. 2012, ApJ, 753, 30
Taylor, E. N., Hopkins, A. M., Baldry, I. K., et al. 2011, MNRAS, 418, 1587
Thilker, D. A., Boissier, S., Bianchi, L., et al. 2007, ApJS, 173, 572
Thilker, D. A., Hoopes, C. G., Bianchi, L., et al. 2005, ApJ, 619, 67
Tielens, A. 2008, ARA&A, 46, 289
Tielens, A., & Hollenbach, D. 1985, ApJ, 291, 722
Tilanus, R. P. J., & Allen, R. J. 1993, A&A, 274, 707
Tonry, J. L., Dressler, A., Blakeslee, J. P., et al. 2001, ApJ, 546, 681
Treyer, M., Johnson, B., Schiminovich, D., & O'Dowd, M. 2010, ApJ, 719, 119
Treyer, M., Schiminovich, D., Johnson, B., et al. 2007, ApJS, 173, 256
Tully, R. B. 1988, Nearby Galaxy Catalog (New York: Cambridge Univ. Press)
Tully, R. B., Rizzi, L., Shaya, E. J., et al. 2009, AJ, 138, 323
Westmeier, T., Braun, R., & Koribalski, B. 2011, MNRAS, 410, 2217
Willick, J. A., Courteau, S., Faber, S. M., et al. 1997, ApJS, 109, 333
Wolfire, M. G., McKee, C. F., Hollenbach, D., & Tielens, A. G. G. M. 2003, ApJ, 587, 278
Wright, E. L., Eisenhardt, P. R. M., Mainzer, A. K., et al. 2010, AJ, 140, 1868
Zhu, Y.-N., Wu, H., Li, H., & Cao, C. 2010, RAA, 10, 329
Zibetti, S., Charlot, S., & Rix, H. 2009, MNRAS, 400, 1181